High-resolution spatio-temporal quantification of fish predator-prey interactions over ecosystem scales with multispectral underwater sensing and optimality of human visual perception with natural daylight

by

Shourav Pednekar

Submitted to the Department of Mechanical Engineering
in partial fulfillment of the requirements for the degree of

Doctor of Philosophy

at the

MASSACHUSETTS INSTITUTE OF TECHNOLOGY

June 2023

Author .....
Department of Mechanical Engineering
May 11, 2023

Certified by .....
Nicholas C. Makris
Professor of Mechanical and Ocean Engineering
Thesis Supervisor

Accepted by .....
Nicolas Hadjiconstantinou
Chairman, Department Committee on Graduate Theses

High-resolution spatio-temporal quantification of fish predator-prey interactions over ecosystem scales with multispectral underwater sensing and optimality of human visual perception with natural daylight

by

Shourav Pednekar

Submitted to the Department of Mechanical Engineering
on May 11, 2023, in partial fulfillment of the
requirements for the degree of
Doctor of Philosophy

Abstract

Marine ecosystems face simultaneous pressures from human activities, ocean industrialization, potential global warming and changing habitats. Continuous monitoring of marine biodiversity and ecosystem processes is needed to assess the individual fish species survivability in such conditions. The increasing use of computer modeling and simulations based on significantly under-sampled data of the marine environment, however, leads to unconstrained and potentially unstable predictions of key processes. To address this issue, we demonstrate a technology enabling synoptic quantification and distinction of multispecies fish population densities over ecosystem scales with continuous spatial and temporal resolution. This enables high-resolution quantification of predator-prey interactions in space and time over ecosystem scales. We present an example of an event in the Barents Sea where a massive cod predatory swarm of approximately 1.9 million individuals attacks a defending coherently moving linear capelin prey structure extending over 14 km containing approximately 23 million individuals. Capelin are a keystone species of the Arctic ecosystem. Cod are their primary predator, but cod populations have collapsed everywhere except in the Nordic Seas due to overfishing causing significant changes in ecosystem balance in those regions. We provide high-resolution spatial density images finely sampled over time of cod convergence on capelin prey, estimated capelin consumed, capelin survived and satiated cod predators quantifying the detailed spatio-temporal dynamics of predation. From these we estimate 58% of the entire capelin group was consumed by the swarming cod within 4 hours where the detailed imagery of behavioral shoal structure show capelin in the highest density regions have the highest probabilities of survival. Other interactions we quantified between predatory juvenile cod and prespawning capelin groups indicate a variety of behavioral mechanisms with varying levels of efficiency are at work for both the predators and prey over the large scales

observed here. These observations are made with multispectral ocean acoustic remote sensing which enables instantaneous imaging of fish populations over thousands of square kilometers with average spatial resolution on the order of 100 m and temporal resolution of about 1 minute. Wide-area species classification and simultaneous population density estimation of individual species employs sensing frequencies at or near fish swimbladder resonance where the large differences across fish species are discernible. Such synoptic imaging at areal rates roughly 10^4 to 10^6 times greater than conventional methods may lead to more stable prediction of key ecosystem processes and has broad applications in remotely classifying fish populations, studying ecosystem functions and assessing species sustainability.

Patterns in light intensity contain vital information for organisms that utilize visual sensory perception for survival in their environments. Psychophysical experiments on visual intensity discrimination with artificial light sources over a century have shown that the smallest detectable change in light intensity, termed just-noticeable difference, grows roughly in direct proportion to the stimulating intensity, approximately following Weber's law of perception. The potential advantages of Weber's law in the context of sensing and pattern recognition, however, have not been quantified given the natural intensity scintillation of environmental light. Here we find Weber's Law to be a consequence of attaining the theoretical minimum mean-square error possible, the Cramer-Rao lower bound, in resolving the intensity of naturally scintillating light. We first obtain the statistics of environmental light signals which we find naturally scintillate with a standard deviation proportional to mean intensity. Given our natural scintillating light intensity data, we find log-transformed intensity and Fechnerian transformed intensity are equivalent to variance-stabilizing-transformed intensity. We then find intensity resolution that follows Weber's Law is statistically optimal in pattern recognition by simple matched-filter correlation and maximizes information reception by homeomorphically transforming signal-dependent intensity scintillation to signal-independent Gaussian noise which can be canceled without loss of signal information. We show just-noticeable-differences in light intensity obtained from psychophysical experiments with artificial light approximately attain the Cramer-Rao lower bound on intensity resolution expected from our observed natural light intensity scintillation. Human intensity resolution is in this manner approximately optimally adapted to the statistical properties of natural light scintillation with Weber's Law as a consequence. Along these lines, the same kind of variance-stabilizing transformation is used in the first part of the thesis in acoustic sensing of fish due to intensity scintillation of measured acoustic intensity data converged upon by the central limit theorem.

Thesis Supervisor: Nicholas C. Makris
Title: Professor of Mechanical and Ocean Engineering

Acknowledgments

I would like to thank my advisor Prof. Nicholas Makris for his guidance and support over the years. Thank you also to Prof. Themistoklis Sapsis and Dr. Yuming Liu for being part of my thesis committee.

I am thankful for the time and help provided by my friends and colleagues from the lab - Arun Krishnadas, Daniel Duane, Byunggu Cho, Dong Hoon Yi, Delin Wang and Chenyang Zhu. Thanks also to Geoffrey Fox for all the administrative help.

Thank you to Dr. Olav Rune Godø for his comments and suggestions on chapter one of the thesis.

I thank my friends Anoop Rajappan, Alok Dadlani and Karan Gandhi for always being supportive.

Above all, I would like to thank my parents Dr. Suhas Pednekar and Dr. Sonali Pednekar for their constant support, love and encouragement; my brother Sushant Pednekar and my sister-in-law Fatine Guedira for their motivation and warmth; and my wife Ekta Joshi Pednekar for her patience and love.

I dedicate this thesis to my family.

Contents

List of Figures

List of Tables

Chapter 1

Millions of predatory cod attack extensive coherent capelin group defensive structures in the Barents Sea quantified with synoptic ecosystem scale sensing

1.1 Introduction

Marine ecosystems face simultaneous pressures from human activities, increasing industrialization, potential global warming and changing habitats which impact the survivability of individual fish species [8, 33, 53, 25, 71, 64]. Better experimental observations of marine biodiversity and associated ecosystem processes are needed to study the sustainability of marine life and aid conservation efforts [72]. As noted previously [59, 58, 57, 30], however, traditional approaches for surveying fish species and mapping their distributions rely on sampling only a small fraction of the survey region and are acutely limited in wide area scanning by their instantaneous coverage scales of hundred meters up to at most a few kilometers [45]. Assessment methods

using such techniques assume statistical stationarity and extrapolations which are not necessarily justifiable [20, 60], and are unable to assess key ecological processes at the temporal and spatial scales at they occur [30]. Here we demonstrate a technology that enables quantification of multispecies fish population densities over ecosystem scales with continuous, high-resolution sampling in space and time. This enables observation and quantification of dynamic ecological processes involving multiple fish species, such as predator-prey interactions, over wide areas.

We do so using multispectral Ocean Acoustic Waveguide Remote Sensing (OAWRS) [59, 58, 40, 41, 90, 57, 94, 17, 18] that enables instantaneous imaging of fish populations over thousands of square kilometers with average spatial resolution on the order of 100 m and temporal resolution of about 1 minute. The OAWRS system makes use of the fact that a waveguide is formed between the sea-surface and the seafloor for sound transmitted on continental shelves [59, 40]. This enables horizontal distances ranging over tens of kilometers and across a 360^o horizontal azimuth to be imaged in time scales of seconds. Several previous investigations have demonstrated the ability of OAWRS to detect, monitor and quantify large fish groups containing tens to hundreds of millions of individuals and stretching over tens of kilometers in varied continental shelf environments [59, 58, 40, 31, 41, 90, 57, 94, 17, 18]. However, classification and enumeration of individual fish species within multispecies aggregations at each resolution cell of the instantaneously imaged area by inferring the scattering contribution of each individual fish species has not been previously demonstrated.

Here we show the ability to remotely classify multiple fish species and simultaneously estimate population densities of multispecies fish groups over ecosystem scales. We quantify cod-capelin predator-prey interactions during an event in the Barents Sea where capelin form vast linear coherent migrating structure extending over 14 km that leads to cod predators forming large counter structures of similar spatial scales and distributions. These cod-capelin interactions are quantified in the northern coastal region of Norway following surveys with OAWRS in February-March 2014. Mature capelin (Mallotus villosus) spawn in this region from late winter to early spring after undertaking large-scale migration from the Barents Sea [68]. Immature Northeast

Arctic cod (Gadus morhua) follow the swarms of mature cod on their way to the cod spawning ground of Lofoten. When the cod migration route crosses the route of migrating mature capelin on the way to the Finnmark coast, the immature cod stop their migration and aggregate in this region to feed on capelin [93, 6, 21]. Monitoring capelin and cod populations in the Arctic and boreal waters has been emphasized over the years [78, 79, 19] because of the key role they play in the pelagic ecosystem of the region.

We find the cod-capelin predator-prey battle went on for approximately four hours and spanned nearly a hundred square kilometers. Capelin form the large densely packed structure when loose dispersed schools congregated after reaching a transition population density close to the sea-surface at the time of transition from night to day. Capelin then undergo synchronous downward migration towards the seafloor, following which we find cod swarming seemingly in response to the capelin group. Our estimates of consumed capelin spatial population densities over time suggest approximately 58% of the entire capelin group could likely have been consumed by the swarming cod within those four hours. Similar estimates of cod consumption on capelin from high resolution spatio-temporal interactions between predatory immature cod and pre-spawning capelin groups are quantified on other instances indicating several behavioral mechanisms are in effect for both the prey and predators.

These observations are made with multispectral ocean acoustic remote sensing with minute-to-minute updates of large multispecies fish populations over wide areas. For swimbladder bearing fish, the gas-filled swimbladders are the primary cause of acoustic scattering at frequencies of hundreds of Hertz to a few kilohertz. Distinct acoustic scattering responses of fish species at frequencies near swimbladder resonance enable robust species classification and population density estimation of individual species in space and time on a per-pixel basis. Such synoptic imaging enables continuous monitoring of ecological processes at areal rates roughly 10^4 times greater than conventional methods. Observations of such spatially and temporally explicit trophic interactions involving large fish groups would not have been possible using conventional techniques.

1.2 Methods

1.2.1 Scattering strength from measured OAWRS images

We obtained simultaneous capelin and cod population density images over areas spanning hundreds of square kilometers near Finnmark, Norway during February-March 2014 using OAWRS which enabled instantaneous wide-area sensing (figure 1-1). The OAWRS system consisted of a vertical source array and a horizontal receiver array in monostatic arrangement towed by the research vessel Knorr. Active source transmissions from the vertical array, deployed at depths 60-70 m below sea-surface, involved linear frequency modulated waveforms of 50 Hz bandwidth and 1 s duration centered at 850, 955, 1125, 1335, 1465 and 1600 Hz. Transmissions from the source are scattered by inhomogenities in the medium and are received by the horizontal receiver array, towed at depths between 60 and 70 m. The receiver array is made up of three sub-arrays: low frequency aperture, mid frequency aperture and high frequency aperture, each consisting of 64 equally spaced hydrophones with respective hydrophone spacing of 1.5 m, 0.75 m and 0.375 m. Wide-area instantaneous OAWRS images are then generated by beamforming, matched filtering and charting scattered returns. The OAWRS images have range resolution of approximately 15 m and angular resolution away from endfire that varies as $\lambda/(Lcos\theta)$ in radians, where λ is the acoustic wavelength, L is the receiver array aperture length and θ is the scan angle from array broadside. Angular resolution enhancement is achieved by combining sub-arrays for beamforming which increases the angular resolution by a factor of approximately 2-3 [91].

The expected square magnitude of the received scattered field [40], $\langle|\phi(\rho_c, f_j)|^2\rangle$, at horizontal location ρ_c and frequency f_j can be expressed as

$$10\log_{10}\frac{\langle|\phi(\rho_c, f_j)|^2\rangle}{|\phi_{\text{ref}}|^2} = SL(\rho_c, f_j) + TLA(\rho_c, f_j) + SS(\rho_c, f_j) \tag{1.1}$$

where $\phi_{\text{ref}} = 1\mu$Pa is the reference acoustic pressure in water, $SL(\rho_c, f_j)$ is the source

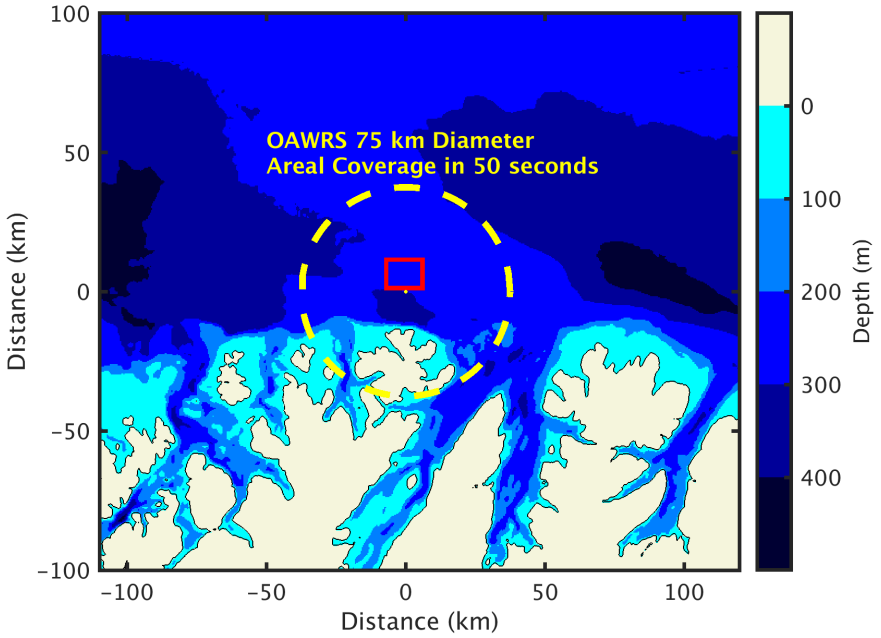

Figure 1-1: Variation in bathymetry near Finnmark, Norway at the location of the Ocean Acoustic Waveguide Remote Sensing (OAWRS) experiment in February-March 2014. The coordinate origin is at 71.2944 deg N, 25.7193 deg. The yellow dashed circle shows 75 km diameter OAWRS areal coverage in 50 s. The red rectangular box marks the zoomed area investigated here.

level at ρ_c and f_j, $TLA(\rho_c, f_j)$ is the depth-averaged transmission loss (Appendix A) to and from the scattering layer integrated over the OAWRS resolution footprint $A(\rho_c, f_j)$ and $SS(\rho_c, f_j)$ is the scattering strength within $A(\rho_c, f_j)$. Equation 1.1 assumes the sonar equation is valid, which is true because the typical wavelengths of OAWRS transmitted signals are much larger than fish swimbladder length scales, that is most fish are acoustically compact scatterers. The scattered field from an individual fish is then omnidirectional which allows factorization of propagation and scattering terms [75].

Scattering Strength SS_{data} images can then be obtained from the measured OAWRS scattered field by accounting for source level, two-way range-dependent transmission loss and areal resolution footprint of the imaging system as

$$SS_{\text{data}}(\rho_c, f_j) = 10\log_{10}\frac{\langle|\phi(\rho_c, f_j)|^2\rangle}{|\phi_{\text{ref}}|^2} - SL(\rho_c, f_j) - TLA(\rho_c, f_j) \tag{1.2}$$

The expected scattering strength within the resolution footprint $A(\rho_c, f_j)$ containing $N(\rho_c)$ scatterers [31] is

$$SS_{\text{model}}(\rho_c, f_j) = 10\log_{10}\left(\sum_{i=1}^{N(\rho_c)}\left\langle\left|\frac{S_i(f_j)}{k}\right|^2\right\rangle\right) - 10\log_{10} A(\rho_c, f_j) \tag{1.3}$$

where S_i is the scatter function of the i^{th} scatterer and k is the acoustic wavenumber. For two types of scatterers within the resolution footprint $A(\rho_c, f_j)$ with scatter functions S_I and S_{II} corresponding to two different fish species each with N_I and N_{II} independent, identically distributed fish respectively with random position and orientation,

$$\sum_{i=1}^{N(\rho_c)}\left\langle\left|\frac{S_i(f_j)}{k}\right|^2\right\rangle = \sum_{i_I=1}^{N_I(\rho_c)}\left\langle\left|\frac{S_I(f_j)}{k}\right|^2\right\rangle + \sum_{i_{II}=1}^{N_{II}(\rho_c)}\left\langle\left|\frac{S_{II}(f_j)}{k}\right|^2\right\rangle \tag{1.4}$$

$$= \left[n_{A_I}(\rho_c)\left\langle\left|\frac{S_I(f_j)}{k}\right|^2\right\rangle + n_{A_{II}}(\rho_c)\left\langle\left|\frac{S_{II}(f_j)}{k}\right|^2\right\rangle\right]A(\rho_c, f_j) \tag{1.5}$$

where $n_{A_I}(\rho_c) = \frac{N_I(\rho_c)}{A(\rho_c, f_j)}$, $n_{A_{II}}(\rho_c) = \frac{N_{II}(\rho_c)}{A(\rho_c, f_j)}$ are the areal densities of scatterer types I and II respectively and $N_I(\rho_c) + N_{II}(\rho_c) = N(\rho_c)$. Then from equations 1.3-1.5

$$SS_{\text{model}}(\rho_c, f_j) = 10\log_{10}\left[n_{A_I}(\rho_c)\left\langle\left|\frac{S_I(f_j)}{k}\right|^2\right\rangle + n_{A_{II}}(\rho_c)\left\langle\left|\frac{S_{II}(f_j)}{k}\right|^2\right\rangle\right] \tag{1.6}$$

The above formulation assumes that the total scattering strength at any pixel is the sum of contribution from fish scatterers only and seafloor scattering effects or other inhomogeneities are small compared to the scattering from fish.

Areal population densities of capelin and cod can then be estimated from scattering strength images after obtaining scatter functions of capelin and cod.

1.2.2 Scatter function model for capelin and cod

Scatter functions of capelin and cod are modeled by utilizing local in-situ measurements of shoal occupancy depths from RV Knorr echosounder and fish length distribution from trawl catch samples. Let scatter function $S_I = S_{cp}$, where S_{cp} is the scatter function of an indiviual capelin in a uniformly distributed vertical layer over depth z with mean shoal depth $z_{0,cp}$, shoal thickness H_{cp}, neutral buoyancy depth $z_{nb,cp}$ and length distribution $g_{cp}(l_{cp})$. Then,

$$\left\langle \left| \frac{S_I(f_j)}{k} \right|^2 \right\rangle = \left\langle \left| \frac{S_{cp}(z, z_{nb,cp}, l_{cp}, f_j)}{k} \right|^2 \right\rangle \tag{1.7}$$

$$= \frac{1}{H_{cp}} \int_{z_{0,cp}-H_{cp}/2}^{z_{0,cp}+H_{cp}/2} \int_{l_{cp}} \left| \frac{S_{cp}(z, z_{nb,cp}, l_{cp}, f_j)}{k} \right|^2 g_{cp}(l_{cp})\, dl_{cp}\, dz \tag{1.8}$$

Similarly, when scatter function $S_{II} = S_{cd}$, where S_{cd} is the scatter function of an indiviual cod in a uniformly distributed vertical layer over depth z with mean shoal depth $z_{0,cd}$, shoal thickness H_{cd}, neutral buoyancy depth $z_{nb,cd}$ and length distribution $g_{cd}(l_{cd})$,

$$\left\langle \left| \frac{S_{II}(f_j)}{k} \right|^2 \right\rangle = \left\langle \left| \frac{S_{cd}(z, z_{nb,cd}, l_{cd}, f_j)}{k} \right|^2 \right\rangle \tag{1.9}$$

$$= \frac{1}{H_{cd}} \int_{z_{0,cd}-H_{cd}/2}^{z_{0,cd}+H_{cd}/2} \int_{l_{cd}} \left| \frac{S_{cd}(z, z_{nb,cd}, l_{cd}, f_j)}{k} \right|^2 g_{cd}(l_{cd})\, dl_{cd}\, dz \tag{1.10}$$

Scatter functions of individual capelin S_{cp} and individual cod S_{cd} are obtained from Love's model [54] following equations provided in Ref. [40] (Appendix B) with physical parameters of capelin and cod obtained from local in-situ echosounder and trawl measurements (Table 1.1). Neutral buoyancy depths $z_{nb,cp}$ and $z_{nb,cd}$ are deter-

mined by establishing the best fit between respective modeled and measured scattering strength of capelin and cod (Appendix C).

Species	Capelin	Cod
Mean length (cm)	17	61
	5-30 (04:15 to 05:15 CET)	50-250
Occupancy depths (m)	20-40 (05:25 CET)	50-250
	30-60 (05:35 CET)	50-250
Neutral buoyancy depth estimate (m)	7 (05:25 CET)	280

Table 1.1: Physical parameters of modeled fish species. Mean lengths of capelin and cod are obtained from trawl capture measurements during January-March 2014 for spawning capelin and immature cod respectively [61]. Capelin and cod group occupancy depths are obtained from local in-situ vertical echosounder measurements from RV Knorr, operating at 12 kHz, at the time of the OAWRS experiment. Neutral buoyancy depths are determined by establishing the best fit between respective modeled and measured scattering strength of capelin and cod following maximum likelihood estimation (Appendix C).

1.2.3 Capelin and cod areal population density estimation

Areal population densities of capelin and cod at each pixel are inferred from the measured scattering strength at that pixel using the maximum likelihood estimation method. That is, for any pixel at horizontal location ρ_c, two parameters are to be estimated: areal population density of capelin $n_{A_{capelin}}$ and areal population density of cod $n_{A_{cod}}$. Here, scattering strength measurements at any pixel in logarithmic domain are assumed to be realizations of Gaussian random variables converged upon by the central limit theorem that are variance-stabilized, that is, standard deviation is independent of the mean. Then, the multivariate Gaussian log-likelihood function [74] for an N_f-dimensional vector of scattering strength measurements $\mathbf{SS} = [SS_{\text{data}}(f_1), SS_{\text{data}}(f_2), ..., SS_{\text{data}}(f_{N_f})]$ for frequencies $f_1, f_2, ..., f_{N_f}$ at any pixel can be expressed as

$$l(n_{A_{capelin}}, n_{A_{cod}}) = \sum_{j=1}^{N_f} \Big\{ -\frac{1}{2}\frac{(SS_{\text{data}}(f_j) - SS_{\text{model}}(f_j|n_{A_{capelin}}, n_{A_{cod}}))^2}{\sigma_{f_j}^2} - \frac{1}{2}\log(2\pi\sigma_{f_j}^2) \Big\} \tag{1.11}$$

where $\sigma_{f_j}^2$ is the variance of measured scattering strength at frequency f_j, $j = 1, 2, ..., N_f = 6$, $SS_{\text{data}}(f_j)$ is the measured scattering strength from equation 1.2 with ρ_c dropped for convenient notation and $SS_{\text{model}}(f_j|n_{A_{capelin}}, n_{A_{cod}})$ is the expected scattering strength from equation 1.6 with $n_{A_I} = n_{A_{capelin}}$, $n_{A_{II}} = n_{A_{cod}}$, $S_I = S_{cp}$ and $S_{II} = S_{cd}$.

Optimal estimates $\hat{n}_{A_{cp}}$ and $\hat{n}_{A_{cd}}$ of the areal population densities $n_{A_{capelin}}$ and $n_{A_{cod}}$ are determined by an exhaustive search over the ranges of capelin and cod population densities such that the log-likelihood function in equation 1.11 is maximized. This is equivalent to minimizing the magnitude of the weighted sum of square difference between the measured scattering strength and expected scattering strength:

$$\min_{n_{A_{capelin}}, n_{A_{cod}}} \left| \sum_{j=1}^{N_f} \Big\{ -\frac{1}{2}\frac{(SS_{\text{data}}(f_j) - SS_{\text{model}}(f_j|n_{A_{capelin}}, n_{A_{cod}}))^2}{\sigma_{f_j}^2} \Big\} \right| \tag{1.12}$$

Areal population densities of capelin and cod thus obtained are mapped over all pixels and presented in figure 1-2.

1.3 Results and Discussion

1.3.1 Species classification shows dense, coordinated capelin shoals in the presence of cod

On February 27 2014 at 05:25 Central European Time (CET) local time, approximately 1.5 hours prior to local sunrise, strong line-like features were observed in the scattering strength maps, as shown in figure 1-2a for transmitted source frequency of

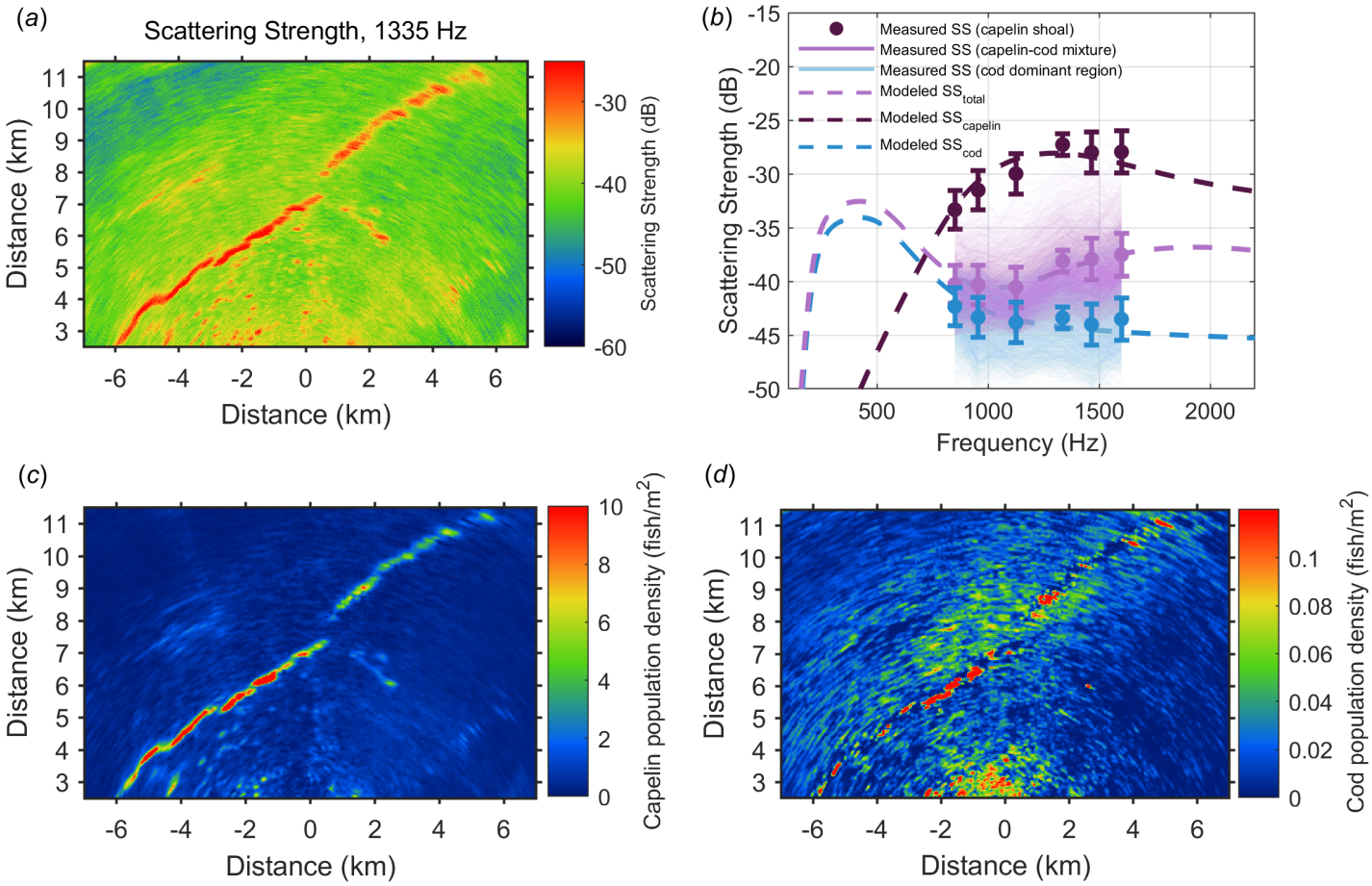

Figure 1-2: Spatial populations containing a mixture of capelin and cod were found in the northern coastal waters of Finnmark, Norway on 27 February 2014. (a) Instantaneous OAWRS scattering strength image at 05:25:49 CET for sensing frequency 1335 Hz showing a bounded, near-contiguous, dense scatterer surrounded by a region of relatively high scattering strength. Location of OAWRS source, towed by Research Vessel Knorr, at 05:25:49 CET is taken to be the coordinate origin, at 71.2944 deg N, 25.7193 deg E. Seafloor depths in the imaged region ranged from 270 m to 290 m. (b) Distinct frequency responses of capelin and cod enables simultaneous species classification and population estimation at each pixel. Using measurements at frequencies centered at 850, 955, 1125, 1335, 1465 and 1600 Hz, the resonance peak for capelin was found to be around 1335 Hz. Within this frequency band, a dynamic range of roughly 7 dB was obtained for scattering strength of capelin with a significant fall-off away from resonance. Cod dominant regions were identified by the slightly decreasing trend in the frequency response with scattering strength model for young cod showing estimated resonance frequency below 500 Hz, outside the sensing frequency band. Composite areas containing capelin-cod mixture typically showed maximum scattering strength at frequencies above 1335 Hz. Brown, violet and blue dashed lines correspond to the modeled scattering strengths of capelin, capelin-cod mixture and cod respectively. (c) Densely packed, roughly 14 km long capelin group containing approximately 23 million individuals imaged on Feb 27, 2014 at 05:25:49 CET about 20 km north of the Finnmark coast. (d) Cod distribution surrounding the dense capelin shoals.

1335 Hz. The x and y coordinates in figure 1-2a are plotted in terms of distance in kilometers relative to the source location at the instantaneous time 05:25 CET. Scattering strength at each resolution cell of the image for any source frequency is the total sum of contributions from all types of scatterers in that resolution cell, which could be an individual fish, multiple individuals of a single species, multiple individuals of different fish species, seafloor, other inhomogeneities, or a combination of all of these. A vector of scattering strength measurements $\mathbf{SS}_{\text{data}}(\rho_c)$ was then formed at each pixel with horizontal location ρ_c over the OAWRS sensing frequencies f_j where $j = 1, 2, ..., 6$ such that $\mathbf{SS}_{\text{data}}(\rho_c) = [SS_{\text{data}}(\rho_c, f_1), SS_{\text{data}}(\rho_c, f_2), SS_{\text{data}}(\rho_c, f_3), SS_{\text{data}}(\rho_c, f_4), SS_{\text{data}}(\rho_c, f_5), SS_{\text{data}}(\rho_c, f_6)]$. Plots of measured scattering strength $SS_{\text{data}}(\rho_c, f_j)$ as a function of frequency f_j for all the pixels over the OAWRS image in figure 1-2a showed several regions over the imaged area where measured scattering strength frequency response matched modeled scattering strength responses of either capelin or cod (figure 1-2b). Regions were also found where measured scattering strength showed trends of scattering from both capelin and cod indicating a mixture of capelin and cod in such regions. The species were then identified at each pixel by systematic multi-frequency analysis of independent OAWRS scattering strength measurements with distinct spectral characteristics of acoustic scattering from capelin and cod, which matched modeled responses (figure 1-2b), allowing reliable classification and population enumeration at each pixel in space following the methodology outlined in Section 1.2.

The strong line-like features in figure 1-2a were found to be dense, cohesive capelin shoals with surrounding regions containing a mixture of capelin and cod (figure 1-2c,d). This spatial overlap between the two species spanning hundreds of square kilometers was observed roughly 20 km from the coast of Finnmark, Norway, which is a typical spawning ground for Barents Sea capelin [2, 68]. Immature cod also occupy this region during spring, foraging for pre-spawning and spawning capelin [21, 6]. A resonance peak was observed for capelin at around 1.3 kHz with significant fall-off away from resonance, consistent with modeled response (figure 1-2b). The modeled capelin scattering strength response assumes mean capelin length of 17 cm with 10%

standard deviation and uniform distribution over vertical occupancy depths from 20 to 40 m (Table 1.1). Mean value of capelin neutral buoyancy depth of 7 m across the capelin shoals is estimated by establishing the best fit between modeled scattering strength and measured scattering strength over pixels within the capelin shoal (Appendix C). Likewise, measured scattering strength response following a relatively flat trend is consistent with cod scattering and corresponds to the plateau region after the swimbladder resonance peak in the modeled scattering strength response of cod (blue solid lines in figure 1-2b). The modeled cod scattering strength response assumes mean fish length of 61 cm with 10% standard deviation and uniform distribution over vertical depths from 50 to 250 m (Table 1.1). Similar to the case of modeled capelin response, mean cod neutral buoyancy depth of 280 m is estimated by establishing the best fit between modeled and measured scattering strength over pixels in a region showing cod type frequency response (Appendix C). Composite regions containing a mixture of capelin and cod were identified by their measured scattering strength responses (violet solid lines in figure 1-2b) which typically adhere to modeled cod type response for the lower two sensing frequencies and to modeled capelin type response for the higher frequencies.

OAWRS sensing frequency range from 850 Hz to 1600 Hz is at or near expected capelin swimbladder resonance and within a few hundred hertz of expected cod swimbladder resonance. Attenuation in backscattered returns has been observed previously when sensing frequencies were near the fish swimbladder resonance frequencies [17]. In all the data presented here from measurements in the Barents Sea, no significant attenuation effect was observed in OAWRS images of capelin or cod shoals. The shoal widths of the imaged capelin populations were not large enough to produce significant attenuation by theory [17] even as the operating frequencies were close to expected capelin swimbladder resonance. Expected cod swimbladder resonance frequencies were estimated to be around 300-400 Hz, much lower than OAWRS sensing frequencies, and so no significant attenuation was found for scattering from cod.

The instantaneously imaged dense capelin shoals were organized in a nearly contiguous line-like structure extending across a length of approximately 14 km and were

estimated to contain about 23 million individuals with an estimated weight of 667 tons (figure 1-2c). The boundaries of these capelin shoals had a mean density of 1.4 $fish/m^2$ which was roughly three times higher than the mean capelin density in the diffuse regions outside the shoal boundaries. The highest capelin concentrations ranged from 20 to 50 $fish/m^2$ in the interior of the shoals at multiple population centers. These capelin population densities are consistent with typical capelin packing densities at night [40]. Capelin were also found in relatively less dense shoals in the imaged area (figure 1-2c). These diffuse capelin populations were estimated to contain about 52 million individuals. Total capelin population estimates were obtained by integrating fish densities throughout the imaged area. In regions overlapping and surrounding the dense capelin shoals, an estimated 3.3 million immature cod individuals were found diffusely distributed (figure 1-2d) in contrast to capelin's ordered behavior. Regions with a mix of capelin and cod individuals were also identified and their respective areal densities quantified (figure 1-2c,d). The fish scattering levels were almost everywhere higher than seafloor scattering levels found in the Finnmark region where the seafloor depths vary within a small range from 270 m to 290 m. Measured seafloor scattering strength show a frequency dependence that approximately follows $f^{2.3}$ (Appendix D). Minimum cod density detectable approximately 3 dB above seafloor scattering levels at 955 Hz is 0.01 $fish/m^2$. Similarly, minimum capelin density detectable approximately 3 dB above seafloor scattering levels at 955 Hz is 0.24 $fish/m^2$.

The wide-area imaging with OAWRS was carried out in conjunction with simultaneous trawl catches and conventional fish-finding sonar for ground-truth evidence and calibration. Trawl catch samples confirmed the presence of capelin and cod in the survey region, and fish length distributions were obtained, constraining physical parameters required for scattering strength model estimation by reality (Table 1.1). Concurrent vertical echosounder measurements suggested capelin occupied depths within 50 m of the sea-surface with cod concentration below the capelin shoals, typically at depths greater than 50 m from the sea-surface up to 250 m. The formation of such large capelin shoals as seen in figure 1-2c, which for other species has been

previously noted as coordination within spawning assemblages [58, 94], could be an anti-predator maneuver of capelin prior to downward migration in the presence of cod groups at lower depths [73]. Spawning preferences or natural diel cycle such as change in daylight levels may drive capelin's descent towards the seafloor despite predation risk from cod. In the context of fish predator-prey interactions, it is suggested that larger prey group size reduces encounter rate with predators [38], improves responsiveness to risk during predator attacks [77], and decreases predation risk per capita [34].

We investigated OAWRS population density images prior to the formation of the dense capelin shoals shown in figure 1-2. We found a rapid transition from sparse capelin schools in the night to polarized, coherent groups near local sunrise after reaching a transition population density of 1.4 $fish/m^2$ (figure 1-3). First, we observed diffuse capelin schools sporadically spread in the night (figure 1-3a) with small fluctuations in mean population density with time. The loose capelin schools were then found to congregate and form densely packed groups near sunrise (figure 1-3b), presumably triggered by daylight levels. Mean population densities of capelin were computed as a function of time by averaging capelin densities within each non-overlapping rectangular box of size 200 m x 200 m along the length of the capelin shoal as shown in figure 1-3c. As a transition density of 1.4 $fish/m^2$ was attained, the mean capelin population density averaged over all the rectangular boxes shown in figure 1-3c increased rapidly at a rate of 4.9 $fish/m^2$ per hour (figure 1-3d). At the densest part of the capelin shoal, within the rectangular box marked in red in figure 1-3c, the population density rate was steeper at 24.5 $fish/m^2$ per hour. The transition density for this densest capelin region was similarly 1.4 $fish/m^2$. This transition density scales roughly in inverse proportion to fish-length-squared and is consistent with findings from other species [58, 57]. Such a transition from unordered to coordinated behavior after reaching a transition population density is an aspect of collective motion where an individual organism aligns and travels in a direction influenced by neighboring individuals within its field of perception [88, 89]. Mean capelin population densities in the diffuse region, that is, average of capelin densities over the imaged area exclud-

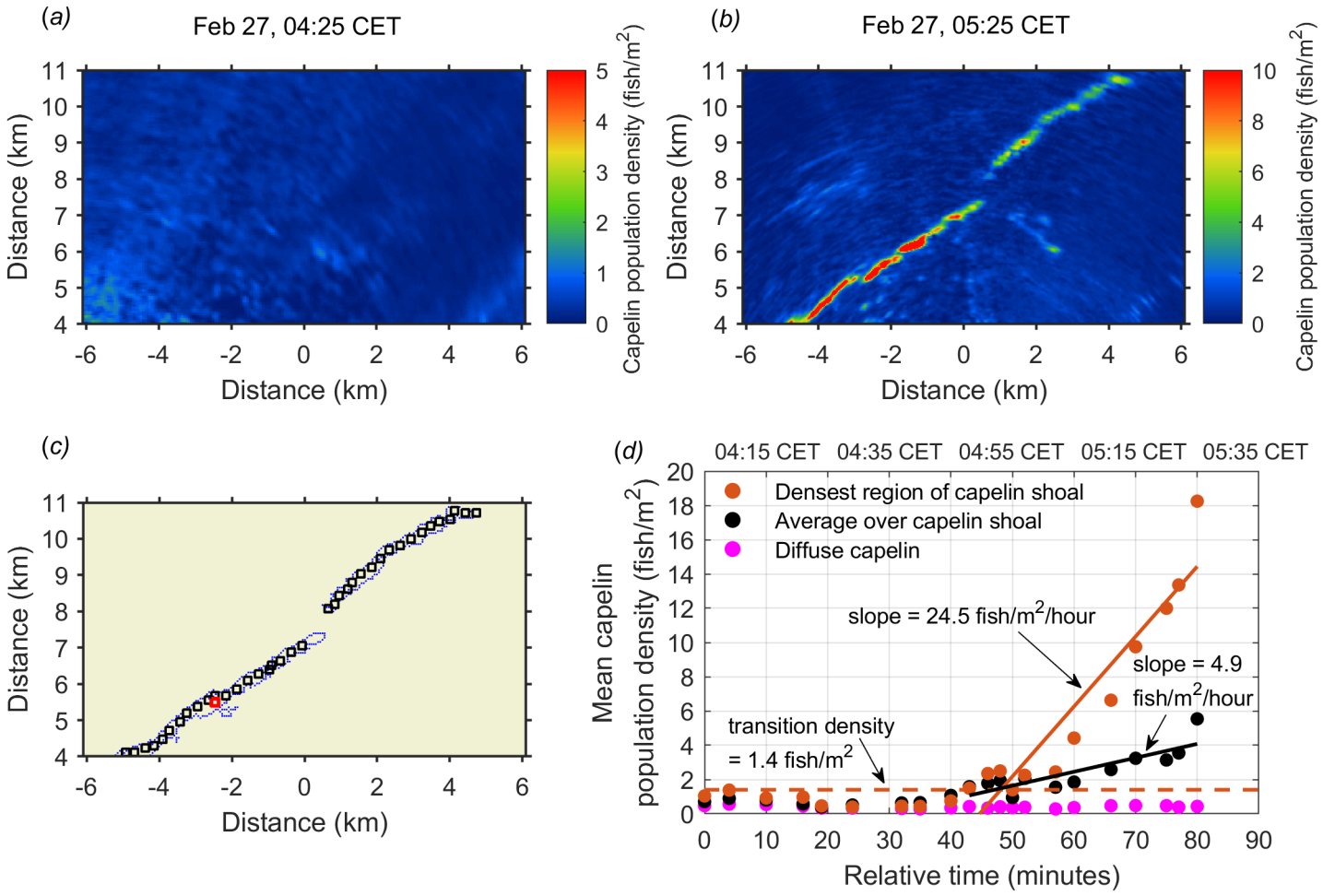

Figure 1-3: Loose capelin schools congregate to form densely packed, organized groups as light levels increase. Relative time starts at 04:05 CET (a,b) Sequence of instantaneous OAWRS areal density images showing short-term spatial and temporal characteristics of the shoal formation process from sparse capelin distribution in (a) to dense cohesive capelin shoals in (b). The coordinate origin is the same as in figure 1-2. (c) Non-overlapping rectangular boxes of size 200 m x 200 m along the length of the capelin shoal from (b) whose outline is shown in blue. Mean capelin population density is estimated over each rectangular box and its average is plotted in (d). Red rectangular box also of size 200 m x 200 m marks the densest region of the capelin shoal. (d) Mean areal population density versus time. Small fluctuations in mean population density is observed before transition density of 1.4 $fish/m^2$ is attained at approximately 04:45 CET. Mean density increases rapidly immediately afterwards. Black solid line is the linear best fit for the data points indicating growth rate for the mean population density averaged from all rectangular boxes. Red solid line is the linear best fit for mean capelin density at the densest part of the shoal marked in (c) with the red rectangular box. Data points in magenta show mean population density over the all the imaged area outside the capelin shoal boundary.

ing the capelin shoals, was consistently below the transition density at around 0.45 $fish/m^2$ and did not show an increase with time. The entire shoaling process, from diffuse background levels consistent with dispersed capelin individuals to formation of denser groups after a transition density was reached, transpired within an hour and is possibly triggered by increasing daylight levels. Autocorrelation time scale of variations in capelin population density was approximately 15 minutes. The growth and ordering of the shoal propagated horizontally as a directional wave with speed around 2 m/s which is an order of magnitude faster than the typical swim speed of capelin. It is suggested that prey in coordinated groups with high polarization, that is high aspect ratio, are at less predation risk than unpolarized swarms [38]. However, this grouping behavior could be due to improved sensing of environmental cues [4] and may not necessarily be due to predation pressures.

1.3.2 Synchronous capelin descent towards seafloor with increase in daylight

After reaching a high population density, the capelin shoals were observed to fade in the OAWRS imagery as light levels increased (figure 1-4 a-f). Vertical profiles from simultaneous echo-sounding line transects from a region roughly 5 km away from the capelin shoals observed in the OAWRS images show that dense capelin layers move down from close to sea-surface to within 20 to 50 m of the seafloor, traversing a vertical distance of roughly 200 m in less than two hours (figure 1-4g). The diminished returns in the OAWRS capelin population density images correspond to a synchronized migration of the densely packed capelin layers towards the seabed at the onset of daylight, with the shoal formation near the sea-surface being a prelude to vertical migration. Capelin schools are known to perform diurnal vertical migrations, staying close to the bottom during the day and rising up to shallow depths of 30 m during the night where they disperse and form loose schools [68]. With estimated average horizontal swimming speed of capelin shoal as 0.15 m/s and direction of travel approximately 135 degrees from positive x-axis, the capelin shoals stay within

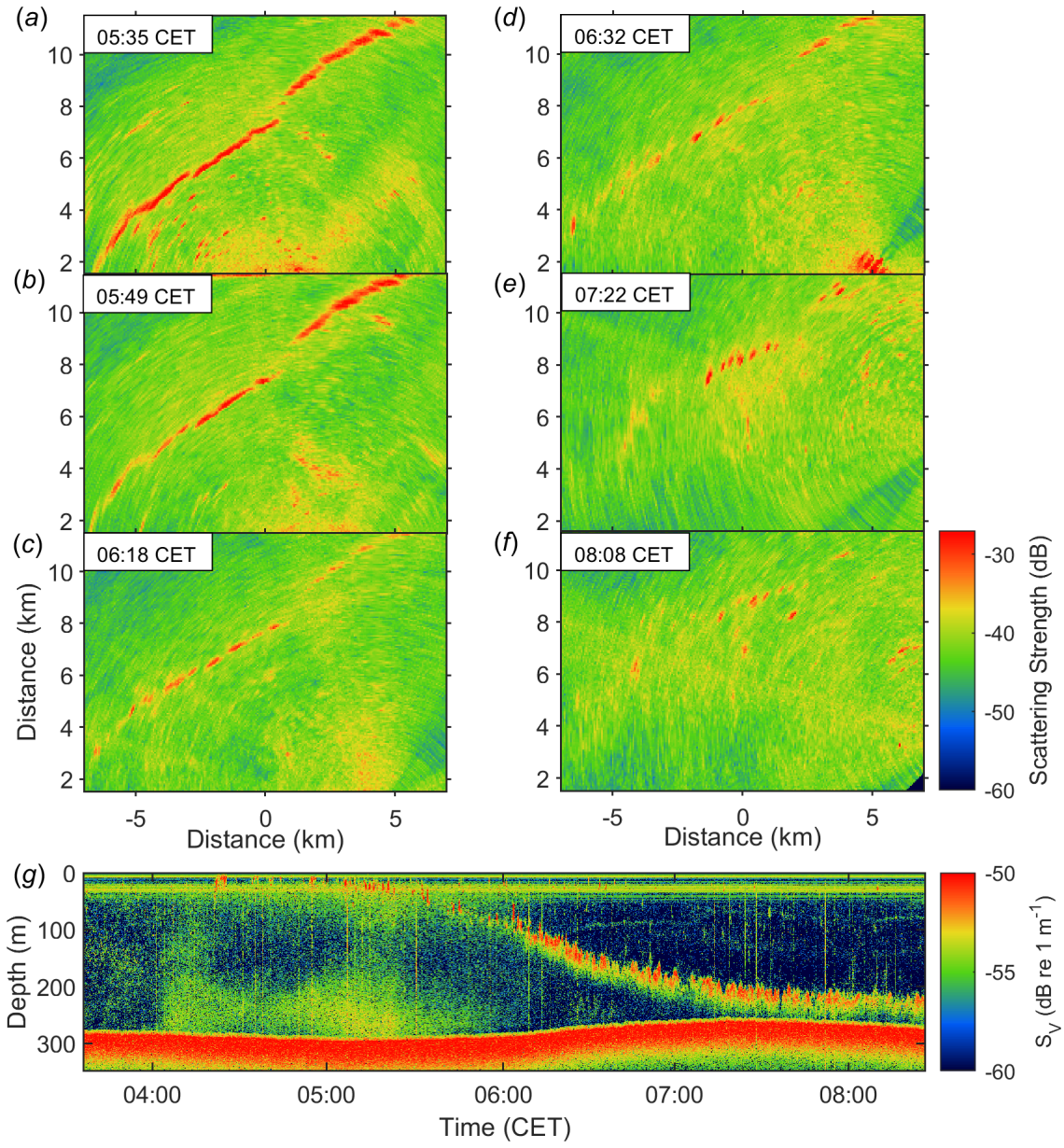

Figure 1-4: Capelin shoals migrate towards the seabed with the descent starting at 05:35 CET, roughly 90 minutes before local sunrise. (a-f) Sequence of instantaneous OAWRS scattering strength images indicating diminished returns from the shoals with time. Gradual horizontal migration with estimated average horizontal swimming speed of capelin shoal as 0.15 m/s and direction of travel approximately 135 degrees from positive x-axis. (g) Time depth profile from simultaneous echosounder measurement of fish volumetric scattering (dB re 1 m^{-1}) measured by conventional fish-finding sonar (CFFS) confirm vertical migration of capelin layers. The coordinate origin in OAWRS images is at 71.2944 deg N, 25.7193 deg E, same as in figures 1-1 and 1-2.

the imaged area, with the extent of horizontal migration not more than 2 km in the direction perpendicular to the shoal length.

The disappearance of capelin shoals from OAWRS imagery could be attributed to a shift in capelin swimbladder resonance frequency, with the peak moving out of operating frequency range as capelin occupied greater depths (figure 1-5). OAWRS uses low frequency transmissions around 1 kHz which is at or near swimbladder resonance of many pelagic fish species [54]. Resonance frequencies depend on fish size, swimbladder volume, occupancy depth in water, and flesh viscosity. Significant variations in the frequency dependence of scattered returns are expected across species due to differences in resonance [40, 31]. Changes or shifts in the resonance peak may also occur for a single species with variations in the depth that the fish occupies. As capelin layers dive deeper within the water column, an increase in the ambient pressure leads to swimbladder volume contraction and, consequently, resonance frequency moves from around 1335 Hz to beyond 1600 Hz, the upper limit of operating frequencies used during the experiment. During this process, we found scattering strength frequency trend to change from a predominantly capelin response with a peak at 1335 Hz (figure 1-5a), through a frequency response of total scattering strength showing adherence to modeled cod response at lower frequencies and modeled capelin response at higher frequencies (figure 1-5b), to a near constant response which is typically observed for cod (figure 1-5c), in the frequency range 850-1600 Hz. This confirmed the horizontal spatial overlap of capelin shoals and cod groups diffusely distributed in the region. Following the species classification and fish population density inference method outlined in §2, capelin and cod areal population densities were estimated and plotted in figure 1-6 during the time period of capelin's vertical migration towards the seafloor. During this descent, as imaged capelin population is shown to reduce following the resonance frequency shift (figure 1-6a), cod population is found to increase in the same region (figure 1-6b) as capelin groups enter cod layers distributed in the water column.

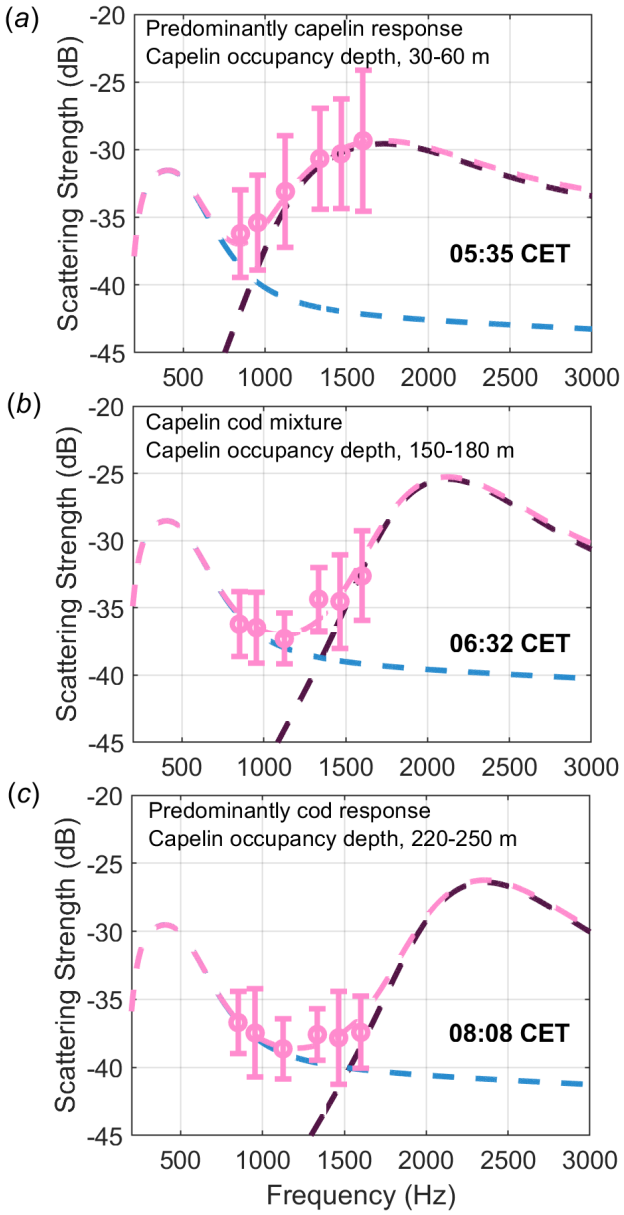

Figure 1-5: Measured Scattering Strength frequency trend of pixels within the capelin shoal boundary at (a) 05:35 CET, (b) 06:32 CET, (c) 08:08 CET, with increase in capelin occupancy depths over time. Swimbladder resonance shift is observed in modeled scattering strength of capelin (brown dashed line) with the resonance peak moving out of the operation frequency range used during the OAWRS experiment. Modeled cod scattering strength is shown in blue dashed line. Measured scattering strength matches well with the total modeled scattering strength (pink dashed line) which sums the contribution of both capelin and cod. Neutral buoyancy depths of capelin. Neutral buoyancy depth of cod is assumed to be the same as in figure 1-2 at 280 m.

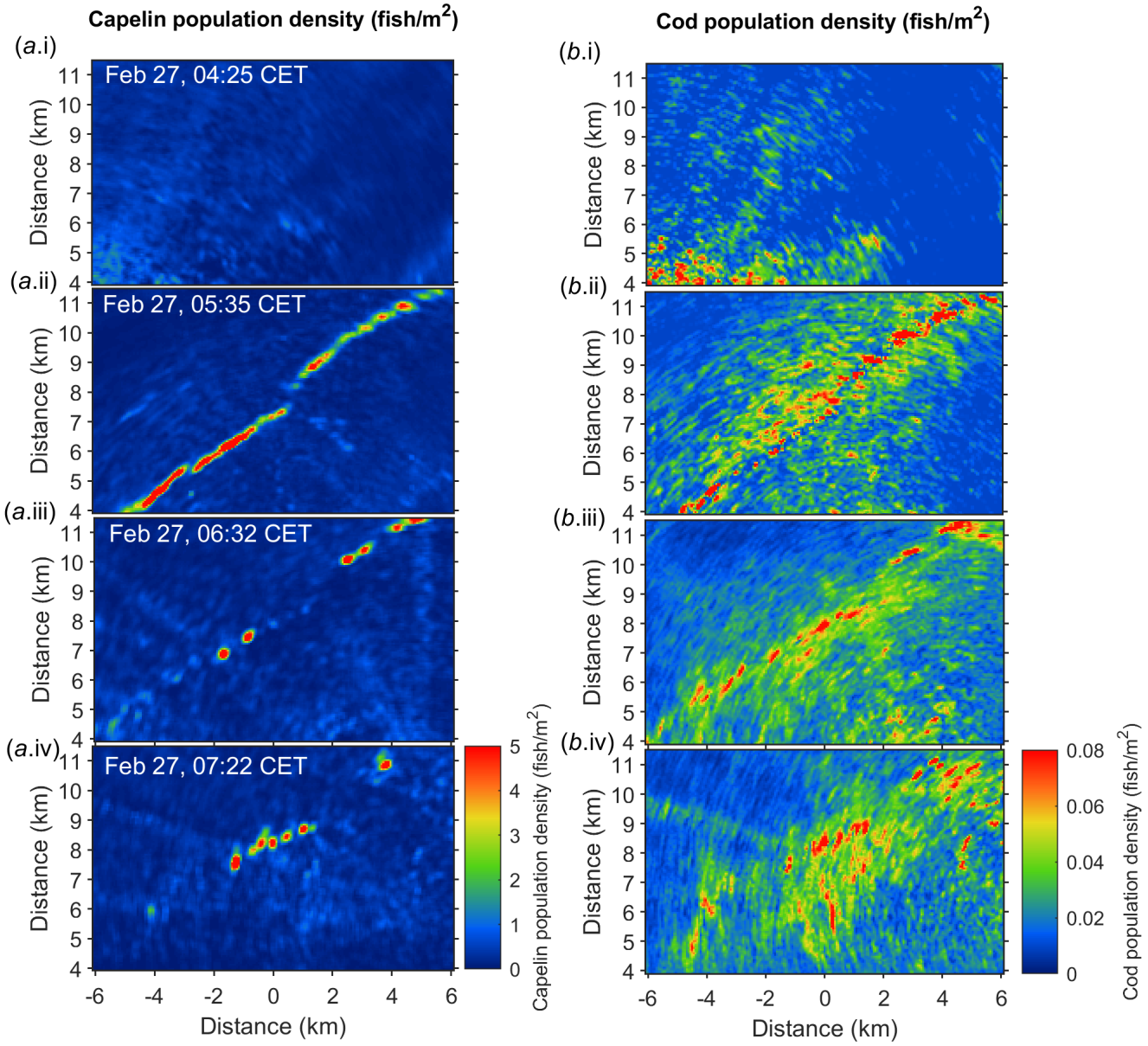

Figure 1-6: (a) Capelin and (b) cod population density maps at (i) 04:25 CET, (ii) 05:35 CET, (iii) 06:32 CET, and (iv) 07:22 CET. The coordinate origin in OAWRS images is at 71.2944 deg N, 25.7193 deg E, same as in figure 1-2.

1.3.3 Cod convergence on descending capelin

Once the capelin shoals descended to the sea floor, we found cod swarming seemingly in response to the capelin shoals and forming their own discrete shoals with spatial scales and distributions similar to the descending capelin (figure 1-7a,b). Amidst the diffusely distributed cod groups, regional pockets were found where cod assembled in large numbers with measured scattering strength frequency response matching modeled cod response (figure 1-7c). The cod were immature and were feeding on capelin, as confirmed from capture trawl and echosounding. The immature cod densities were determined over wide areas with OAWRS, and the shoaling process in time was documented. We found mean cod population density increased at a rate of 0.051 $fish/m^2$ per hour (figure 1-7d), much lower than the capelin shoal formation rate of 4.9 $fish/m^2$ per hour. In the densest cod aggregation, mean cod population density increased at a rate of 0.103 $fish/m^2$ per hour. This increase in the mean cod population density occurred after a transition density of 0.07 $fish/m^2$ was reached. In the diffuse regions, cod density showed a slow rise but was consistently below 0.06 $fish/m^2$. We assume that this is swarming behavior with individual cod predators flocking towards locations of dense capelin groups. It is possible that the convergence of cod may be mediated by communication, with cod known to produce low frequency sound [35]. Predatory swarming in large groups is suggested to increase predation risk per capita [34, 48]. Trawl catch samples from the survey region confirmed that the immature cod were feeding on capelin with undigested capelin found in the stomach content of cod.

1.3.4 Estimated cod predation on capelin

We now obtain quantitative estimates of cod predation on capelin using OAWRS population density maps of both capelin and cod assuming a simple predation model. This assumes that cod that have converged on locations of dense capelin, as seen from the OAWRS cod population density images in figure 1-8a and mean cod population density increase in figure 1-7, arrive there to prey on the capelin shoals. Within

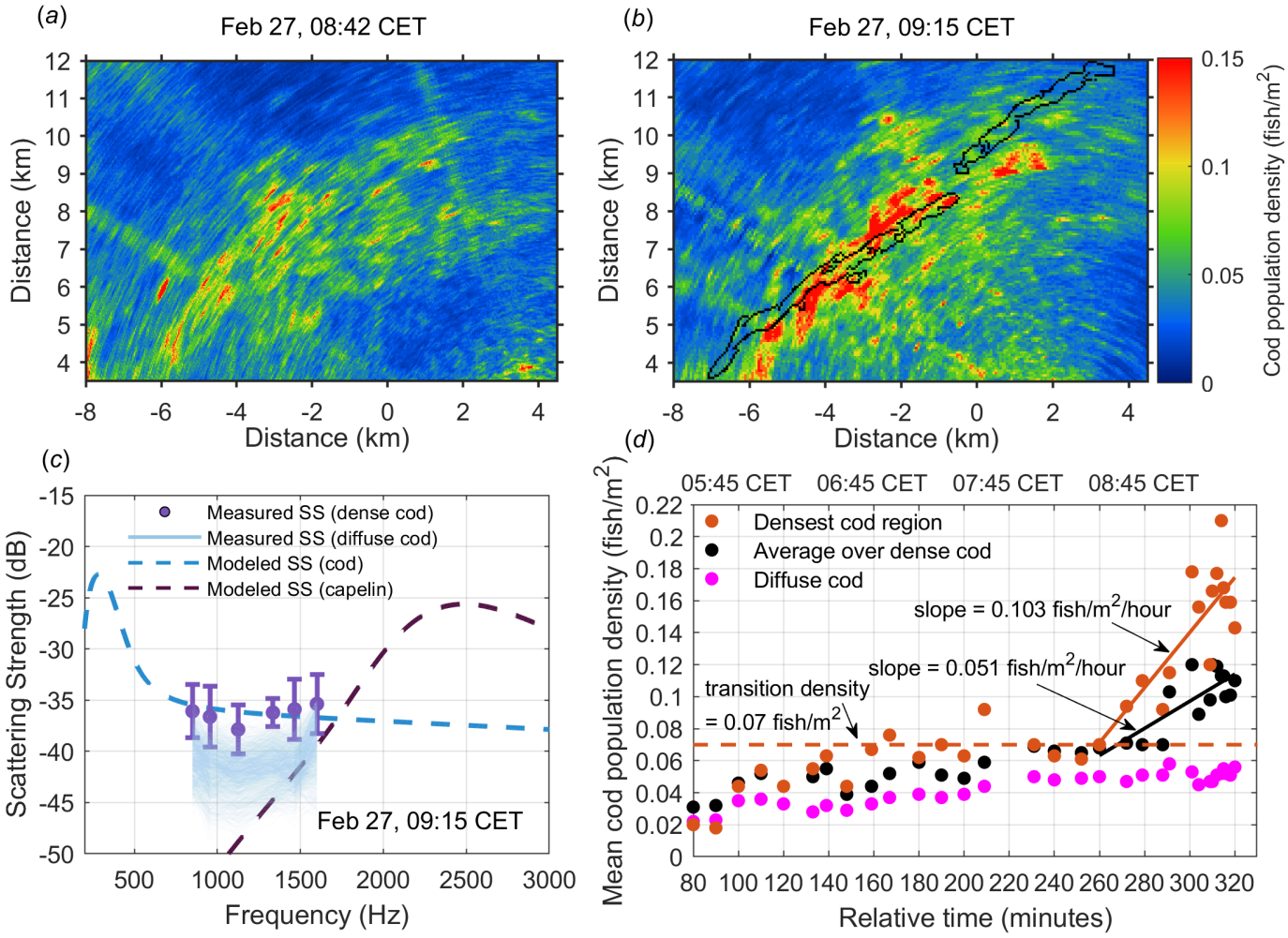

Figure 1-7: Dense cod shoals were observed with scales and spatial distributions similar to capelin. Scales and distributions of cod shoals suggest cod act as individual predators swarming on the existing capelin shoals. (a-b) Sequence of instantaneous OAWRS areal density images showing an increase in density at locations where capelin shoals are expected after descent. Black contour in (b) marks the expected location of capelin shoals with capelin shoal boundary from figure 1-3c shifted by a distance estimated by horizontal speed of 0.15 m/s in the direction of travel roughly 135 degrees from the positive x-axis. (c) Measured scattering strength frequency response show predominantly cod response in both the diffuse and the dense scattering regions. (d) Time series plot of mean cod population density showing a slow growth rate of 0.051 $fish/m^2/hour$ over the regions with dense cod aggregations (black solid line) and a growth rate of 0.103 $fish/m^2/hour$ in the densest cod region (red solid line). Red dashed line shows the transition density at 0.07 $fish/m^2$. Cod densities in the diffuse regions shown with magenta points lie below this transition density.

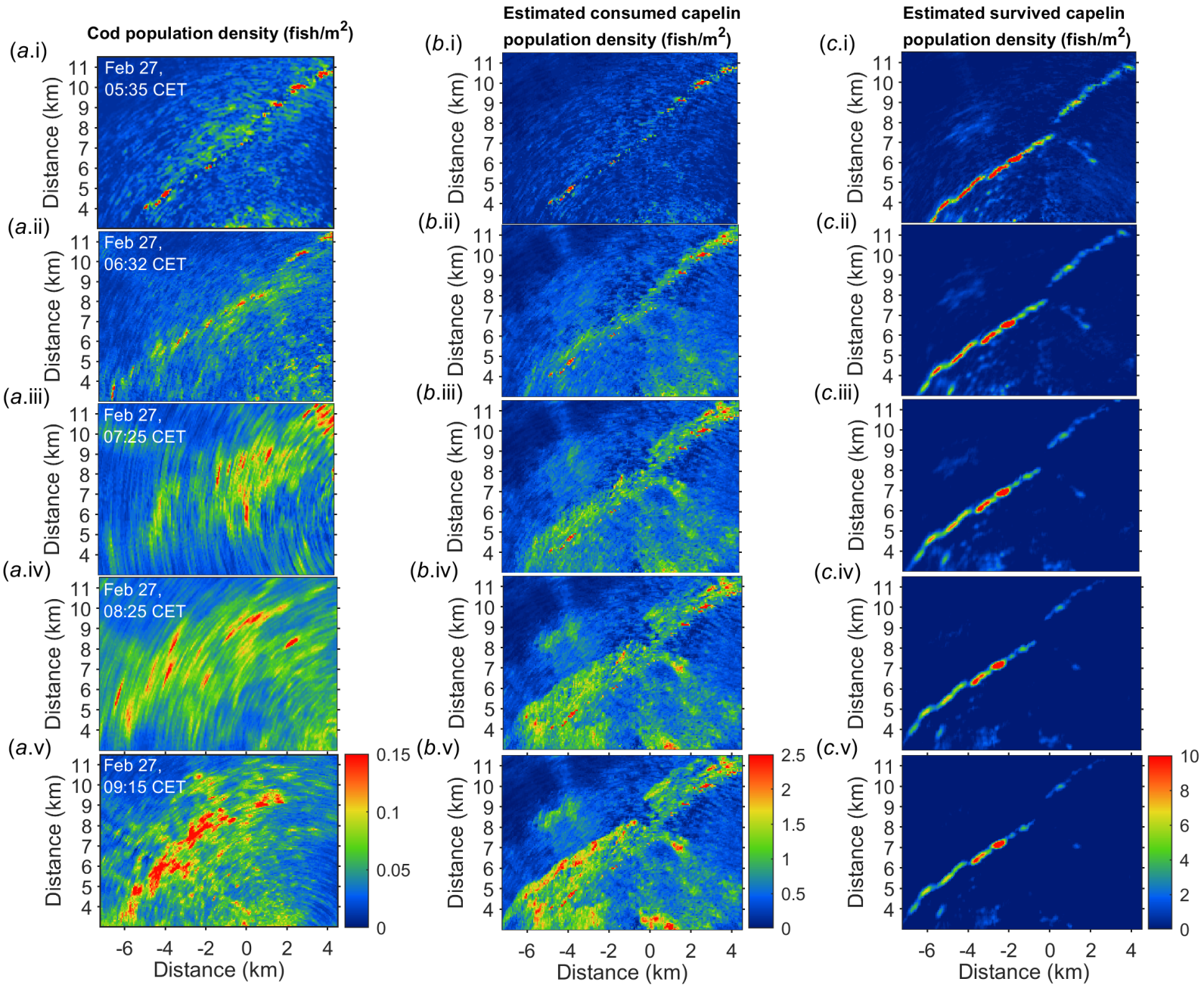

Figure 1-8: Spatial maps of (a) cod population density, (b) estimated consumed capelin population density, and (c) estimated survived capelin population density at (i) 05:35 CET, (ii) 06:32 CET, (iii) 07:25 CET, (iv) 08:25 CET, and (v) 09:15 CET. The population density maps are generated following equations 1.13-1.15 at each resolution cell of the imaged area shown. The coordinate origin is at 71.2944 deg N, 25.7193 deg E, same as in figure 1-2.

a resolution cell of area $A\ m^2$ with capelin population density $n_{A_{capelin}}\ fish/m^2$ cod population density $n_{A_{cod}}\ fish/m^2$, the estimated consumed capelin population density at any time instant t_{n+1} is

$$\begin{aligned} n^{consumed}_{A_{capelin}}(t_{n+1}) &= \gamma[n_{A_{cod}}(t_{n+1}) - n_{A_{cod}}(t_n)], \\ &\text{when } 0 < \gamma[n_{A_{cod}}(t_{n+1}) - n_{A_{cod}}(t_n)] \leq n^{survived}_{A_{capelin}}(t_n) \text{ and } z >= 50m \\ &= n^{survived}_{A_{capelin}}(t_n), \\ &\text{when } \gamma[n_{A_{cod}}(t_{n+1}) - n_{A_{cod}}(t_n)] > n^{survived}_{A_{capelin}}(t_n) \text{ and } z >= 50m \\ &= 0, \text{ otherwise} \end{aligned} \tag{1.13}$$

where $n >= 0$, z is mean capelin occupancy depth from sea-surface and γ, which is the number of capelin consumed by an individual cod, is a constant. It is assumed that cod consumption of capelin between times t_n and t_{n+1} at any resolution cell is due to the increased cod population density at that resolution cell between t_n and t_{n+1}.

The estimated survived capelin population density at time t_{n+1},

$$n^{survived}_{A_{capelin}}(t_{n+1}) = n^{survived}_{A_{capelin}}(t_n) - n^{consumed}_{A_{capelin}}(t_{n+1}) \tag{1.14}$$

and the cumulative consumed capelin population density at time t_{n+1},

$$n^{consumed,total}_{A_{capelin}}(t_{n+1}) = \sum_{k=1}^{n+1} n^{consumed}_{A_{capelin}}(t_k) \tag{1.15}$$

are computed at every pixel and plotted over the whole image as shown in figure 1-8b,c.

Capelin and cod population densities at 05:25 CET are taken to be inputs $n_{A_{capelin}}(t_0)$ and $n_{A_{cod}}(t_0)$ respectively at time t_0 in equation (1.13) such that $n^{survived}_{A_{capelin}}(t_0) = n_{A_{capelin}}(t_0)$. At time t_0, that is at 05:25 CET, $n^{consumed}_{A_{capelin}}(t_0) = 0$ as mean capelin occupancy depth $z < 50$ m from sea-surface.

The estimated percentage of capelin shoal consumed, $\frac{N_{consumed,total}}{N_{capelinshoal}} * 100$, over

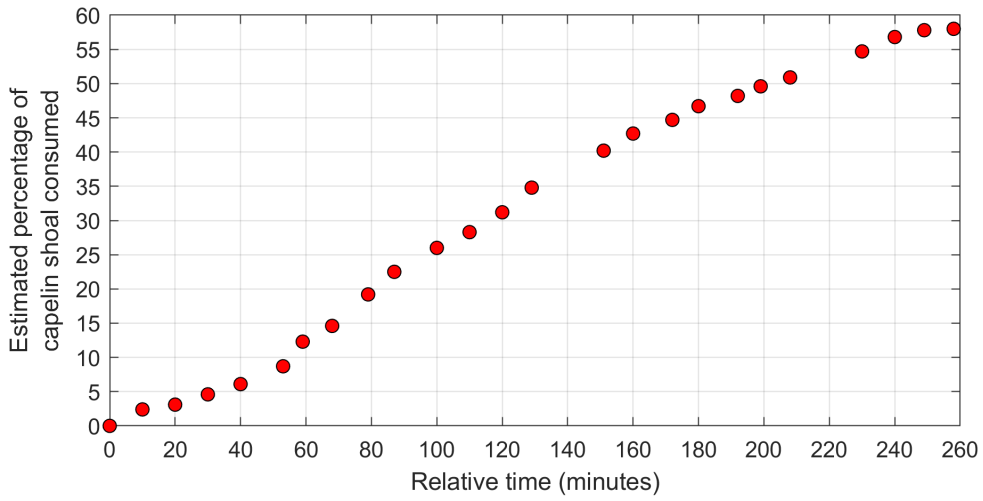

Figure 1-9: Quantitative estimates of cod predation on capelin showing estimated percentage of capelin shoal consumed as a function of time. Relative time starts at 05:25 CET. Total consumption of capelin at any time is the spatial sum of estimated cumulative consumed capelin population density over all pixels or resolution cells within the capelin shoal boundaries.

time is shown in Figure 1-9 for the approximately 14 km long capelin shoal with $N_{capelinshoal} = 23$ million individuals (figure 1-2). $N_{consumed,total}$ is computed by spatially integrating the cumulative consumed capelin population density, $n_{A_{capelin}}^{consumed,total}$, over all pixels within the boundaries of the capelin shoal defined by the threshold of $1.4 fish/m^2$. Any data point in Figure 1-9 shows the estimated percentage of capelin shoal consumed by cod at a particular time t_{n+1} where $n = 0, 1, 2, 3...$ using survived capelin and cod population density maps following equations 1.13-1.15. Echogram measurements show cod occupy vertical depths from 50 m of sea-surface up to the seafloor. Capelin enter cod depth layers within ten minutes of undertaking downward migration from the sea-surface at 05:35 CET. As more cod individuals swarm towards the descending capelin as shown in figure 1-8a, cod population in these regions increases and subsequently the estimated total number of capelin consumed increases. In approximately 4 hours from the initiation of the capelin descent from the sea-surface, the swarming cod are estimated to consume close to 58% of the entire capelin shoal containing $N_{capelinshoal} = 23$ million individuals (figures 1-8b,c and 1-9).

A value of $\gamma = 10$ is used which corresponds to a consumption of 10 capelin, or

approximately 290 grams of capelin, by a cod individual and is based on historical cod stomach sample records [22]. Multiple occurrences of more than 250 grams of capelin in half-digested state have been historically recorded in cod stomach samples from the Barents Sea for cod aged between 5 and 7 years and ranging in length from 58 to 70 cm [22], approximately within one standard deviation of mean cod lengths measured during the 2014 OAWRS experiment in capelin spawning grounds near Finnmark. Cod catches during the time of the experiment from the same research vessel RV Knorr that towed the source and receiver arrays showed at least 7 undigested capelin in the stomach of each individual cod caught.

Over time, the capelin shoal is observed to migrate horizontally in a direction approximately 135 degrees from positive x-axis. Capelin group horizontal speed, $v_{capelin}$, is estimated from spatial cross-correlation between two capelin density maps ten minutes apart from each other with peak correlation coefficient $\rho = 0.804$, and is given as $v_{capelin} = 0.15\ m/s$ when $z <= 230$ m and $v_{capelin} = 0$ when $z > 230$ m, where z is mean capelin occupancy depth from sea-surface.

1.3.5 Other instances of cod-capelin interactions

In addition to the specific event of cod predation on capelin outlined in figures 1-1 to 1-9, there are instances of cod-capelin interactions observed at other times during the OAWRS experiment in Finnmark. In the OAWRS images, cod were present almost everywhere over the wide areas as diffuse background throughout the day-night cycle and in most cases determined the lowest scattering strength levels measured in any OAWRS image above the seafloor scattering levels. Amid the diffuse cod distributions, we found multiple instances of discrete capelin shoals and discrete cod shoals at times as a predator-prey unit showing repetitive dynamics, and at other times with independent behavior with elements of randomness. One of the broad behavioral patterns observed was capelin shoals in the night time. Discrete capelin shoals were observed almost exclusively in the night, i.e. the hours between sunset and sunrise. These discrete capelin shoals were detected as capelin aggregated near the sea-surface during the night and their scattering levels increased above the dif-

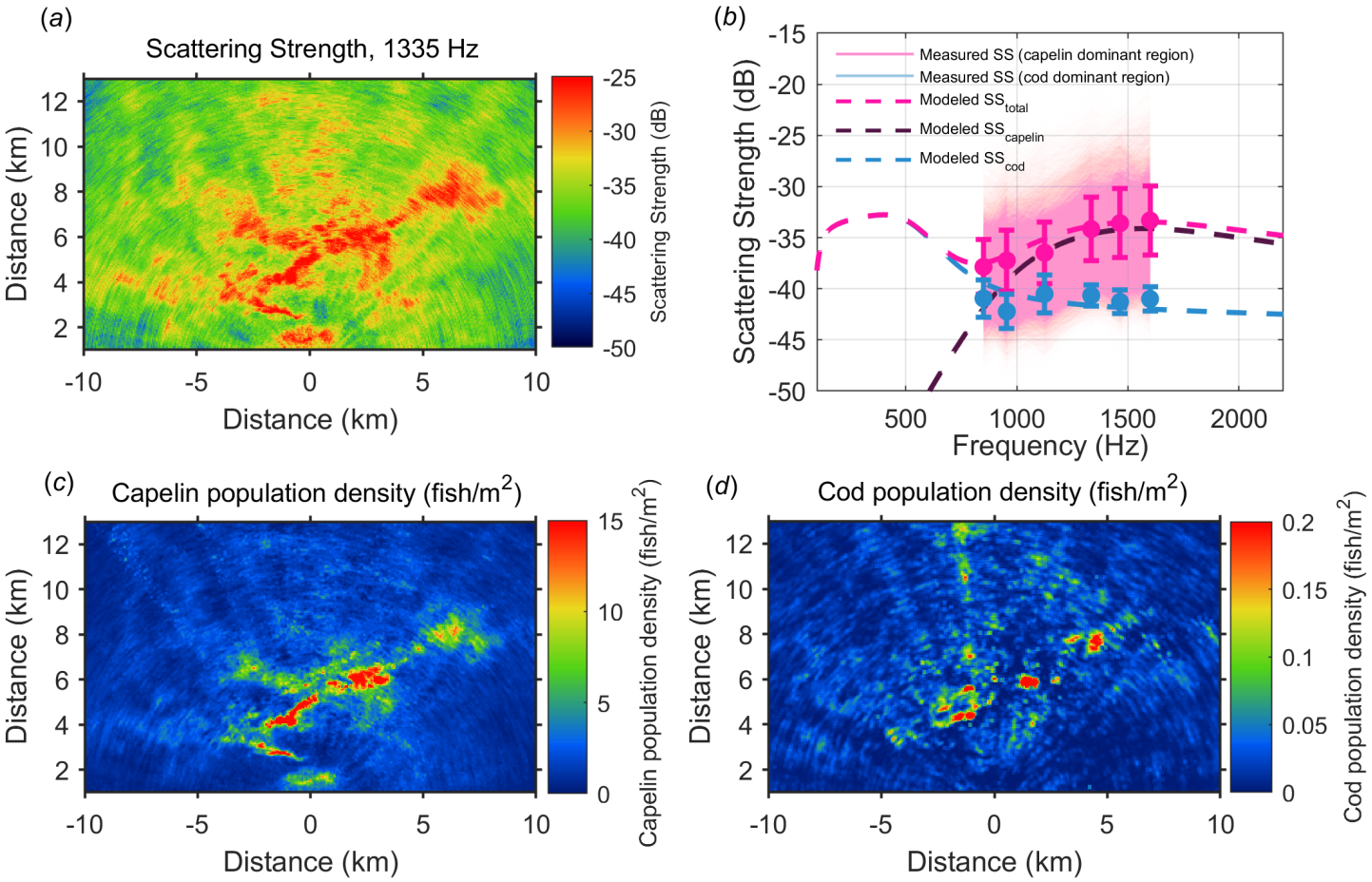

Figure 1-10: Dense capelin shoals with interconnected branches were found on the night of 27 February 2014. (a) Instantaneous OAWRS scattering strength image at 23:15:09 CET for sensing frequency 1335 Hz show dense scattering regions with interconnected branches. Location of OAWRS source, towed by Research Vessel Knorr, at 22:15:09 UTC is taken to be the coordinate origin, at 71.3987 deg N, 25.7098 deg E. (b) Measured scattering strength frequency response at OAWRS sensing frequencies from 850 Hz to 1600 Hz. Each solid line is the measured scattering strength frequency response over the six sensing frequencies at a pixel of the OAWRS image as shown in (a). Colors are assigned to each line based on the frequency at maximum measured scattering strength. A line with scattering strength maximum at frequency equal to or above 1335 Hz is marked pink. A line with scattering strength maximum at frequency below 1335 Hz is marked blue. Scattering strength frequency trend for around 93% of pixels in the image were found to have a the resonance peak around 1335 Hz following modeled capelin scattering strength (brown dashed line) with a dynamic range of approximately 4.5 dB within the sensing frequency range and with a significant fall-off away from resonance. Blue dashed line corresponds to modeled scattering strengths of cod. (c) Densely packed capelin group containing about 78 million individuals. (d) Cod distribution surrounding the dense capelin shoals.

fuse cod populations. Otherwise the capelin go undetected under the dominant cod scattering. The minimum detected capelin populations in terms of $fish/m^2$ depends on the cod population numbers in that area. There are instances in the night time when we found capelin forming shoals possibly without any predator influence (figure 1-10). These night-time capelin shoals had interconnected branches and possibly formed a collective sensing organism in search of a direction to move. Formation of large mobile fish groups has been suggested to improve collective response to environmental information over long spatial scales [4]. The capelin shoals imaged at 23:15 CET (figure 1-10) occupied depths within 40 m of the sea-surface, as evidenced from concurrent RV Knorr echogram measurements. Typical occupancy depths of cod as seen from echosounder measurements in the Finnmark region range from 50-250 m. There is likely a vertical separation between the capelin shoals imaged close to the sea-surface at this time and the cod groups at lower depths.

There is another instance of formation of discrete capelin shoals near the sea-surface approximately 2.5 hours before local sunrise on February 28 (figure 1-11a). In this case, the capelin were relatively less dense with mean density of 1.1 $fish/m^2$, and grouped in multiple shoals of 1-2 km length constituting an estimated 57.8 million capelin individuals. Capelin imaged at 04:15 CET as shown in figure 1-11a were within 50 m of the sea-surface as seen in concurrent echosounder measurements. Relatively high number of cod with an estimated 13.2 million individuals were found in the area (figure 1-11b). Cod convergence on capelin was seen at 05:15 CET as capelin descended to the seafloor (figure 1-11c,d). Capelin descent is likely triggered by increase in daylight levels, as also seen in figures 1-1 to 1-9. From concurrent RV Knorr echogram measurements, capelin depths at 05:15 CET are estimated to be 150 to 200 m. The total capelin population imaged at 05:15 CET (figure 1-11c) is lower than the total capelin population imaged at 04:15 CET (figure 11a). This is likely because of shift in capelin swimbladder resonance beyond the sensing frequency range or due to cod consumption of capelin. However, these behavioral patterns are not seen in all cases at all times. There is at least one instance when capelin form discrete shoals around local sunrise and descend, but we found no discrete cod shoals

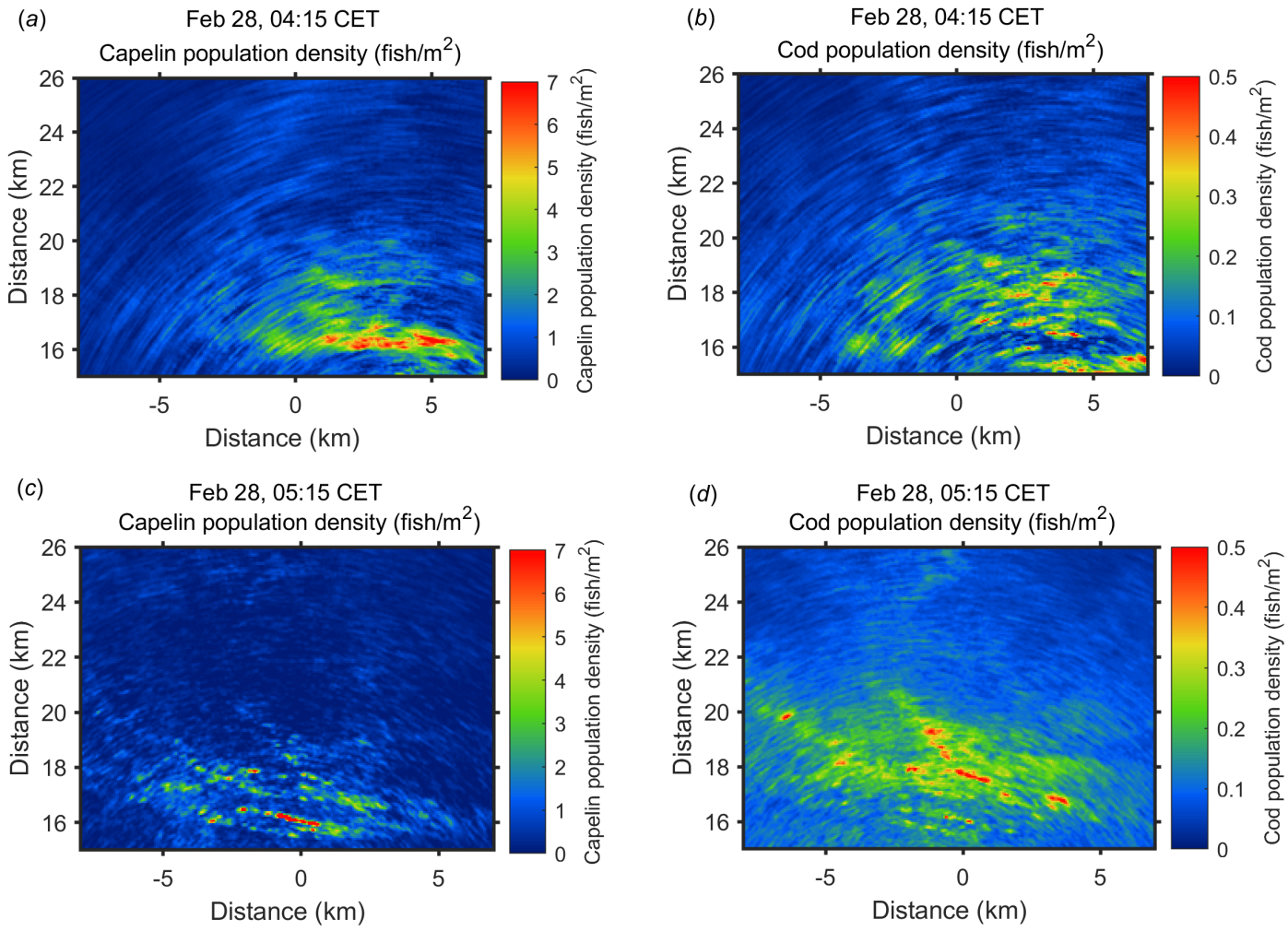

Figure 1-11: Cod convergence on discrete capelin shoals around local sunrise on February 28, 2014. (a) Capelin population density map at 04:15:09 CET with an estimated 57.8 million capelin individuals. Coordinate origin is taken to be 71.3987 deg N, 25.7098 deg E. (b) Cod population density map at 04:15:09 CET with an estimated 13.2 million cod individuals in the imaged area. Areal population densities of capelin and cod are estimated at each pixel from measured scattering strength data following the method outlined in Section 1.2. (c) Capelin population density image at 05:15 CET. Lower capelin population in (c) compared to (a) is likely because of swimbladder resonance shift as capelin occupancy depths increase or because the capelin get eaten by cod. (d) Cod population density image at 05:15 CET showing an increase in cod population numbers in regions where the capelin shoals in (a) are expected. Local sunrise time on February 28, 2014 in Finnmark is 06:53 CET.

that may have driven or responded to the capelin shoals. Furthermore, it is not always the case that capelin form large dense shoals near sunrise time. Capelin also undertake downward migration in small schools again at the onset of daylight (figure 1-12). All these instances are compiled together in figure 1-13 with corresponding quantitative estimates of cod predation on capelin for these instances. The common pattern that emerges is that capelin get eaten when they migrate downwards from the sea-surface at the onset of daylight and enter depths occupied by their predator cod. The predation on capelin occurs irrespective of the fact whether capelin form shoals before migrating or not. The downward migration, in dense shoals or in diffuse schools, seems to be a hardwired behavior correlated to the increase in light levels. On the instance when capelin form large, dense shoals near sea-surface in the nighttime (figure 1-10), roughly 7 hours after local sunrise and 7.5 hours to sunrise, but do not migrate downwards as light levels are expected to be low, less than 10% cod predation is predicted because majority capelin do not enter cod layers and so do not overlap with cod in depth. Overall there is evidence of predator-prey interaction following varied biological mechanisms of shoal formation and group or swarm behavior [4, 34, 39], with elements of randomness and natural variations.

1.4 Conclusion

Human activities such as ocean industrialization and potential global warming put ecosystem functions and survivability of individual fish species at risk. Real-time monitoring and better quantified measurements of key ecosystem processes are needed beyond the use of computer modeling strategies which are based on highly undersampled data. Here, a technology using low frequency, multispectral Ocean Acoustic Waveguide Remote Sensing (OAWRS) is demonstrated which enabled synoptic quantification of multispecies fish population densities over ecosystem scales with continuous spatial and temporal resolution. With remote species classification capability, predator-prey interactions over wide areas are quantified in space and time using multispectral imaging. Distinct scattering responses of fish species at frequencies near

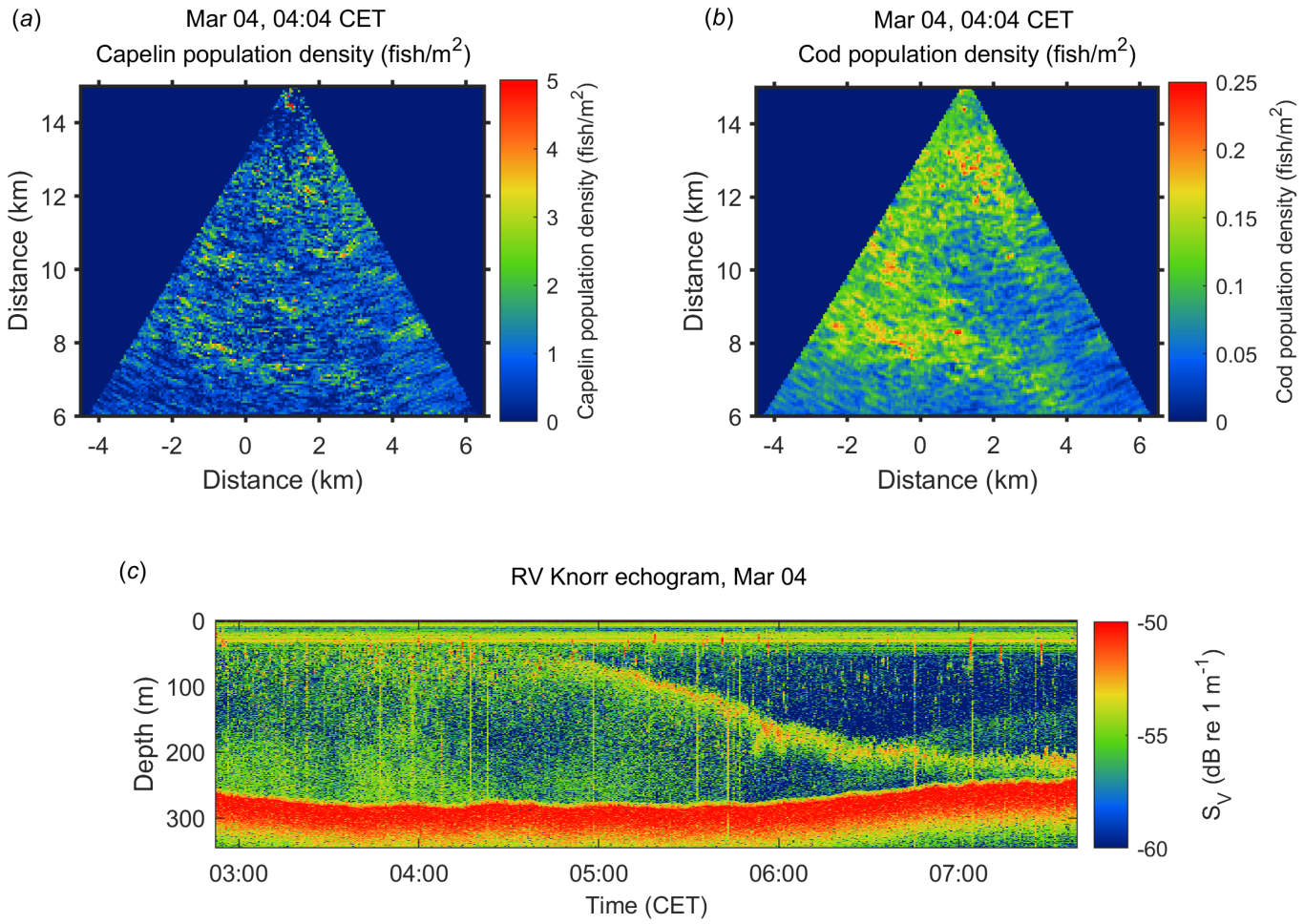

Figure 1-12: Diffuse capelin schools approximately 2.5 hours prior to local sunrise on March 04, 2014. (a) Capelin population density map at 04:04:39 CET with an estimated 18.9 million capelin individuals. Coordinate origin is taken to be 71.3987 deg N, 25.7098 deg E. (b) Cod population density map at 04:04:39 CET with an estimated 4.3 million cod individuals in the imaged area. Areal population densities of capelin and cod are estimated at each pixel from measured scattering strength data following the method outlined in Section 1.2. (c) Time depth profile from concurrent CFFS echosounder confirm vertical migration of diffuse capelin layers. Local sunrise time on March 04, 2014 in Finnmark is 06:33 CET.

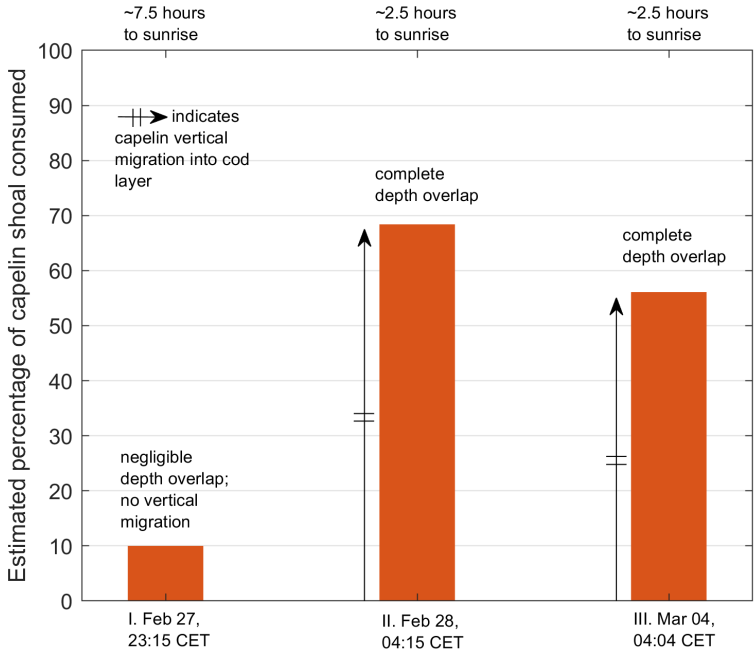

Figure 1-13: (a) Estimates of cod predation on capelin groups imaged using OAWRS on four different instances shown as percentage of capelin shoal consumed. The four instances are: (I) Capelin shoal within 50 m of sea-surface 7 hours after sunset and roughly 7.5 hours before sunrise, no downward migration, imaged on February 27, 23:15 CET (figure 1-10); (II) Discrete capelin shoal within 50 m of sea-surface approximately 2.5 hours before local sunrise, followed by capelin downward migration, imaged on February 28, 04:15 CET (figure 11); (III) Diffuse capelin within 50 m of sea-surface roughly 2.5 hours before local sunrise, followed by capelin downward migration, imaged on March 04, 04:04 CET (figure 1-12).

swimbladder resonance enabled robust classification on a per-pixel basis. An example of an event from the Barents Sea is presented where millions of predatory immature cod attack extensive defensive pre-spawning capelin group organized in coherent linear structure of over 14 km containing approximately 23 million individuals. It is estimated that the swarming cod could likely have consumed about 58% of the entire capelin group within 4 hours. Multiple instances of cod-capelin predator-prey interactions are presented showing varied behavioral dynamics of cod and capelin groups over the large scales observed here.

These observations were made with multispectral ocean acoustic imaging technique with instantaneous ecosystem-scale coverage which enabled remote species classification and simultaneous population density estimation over wide areas with average spatial resolution on the order of 100 m and temporal resolution of about 1 minute. Synoptic OAWRS imaging enabled continuous monitoring of ecological processes such as predator-prey interactions at areal rates roughly 10^4 times greater than traditional methods [59, 58]. Observations of such spatially and temporally explicit trophic interactions involving large fish groups would not have been possible using conventional techniques. While this technique may still work best in conjunction with trawl capture and echosounders, it has the potential to be a starting point for fish classification and quantification of predator-prey interactions over ecosystem scales with implications for future studies of ecosystem functioning, assessment and management of marine resources over wide areas, and for long term impact studies of global warming.

Chapter 2

Weber's Law of perception is a consequence of resolving the intensity of natural scintillating light with the least possible error

2.1 Introduction

The fluctuating intensities of natural terrestrial light contain pattern information vital to the survival of many biological organisms. Higher sensory efficiency in recognizing this information should be favored by natural selection because it leads to greater chances for survival through improved function within the environment. Psychophysical perception [23] investigations over more than one hundred years have consistently shown that human perception of controlled artificial light intensity approximately follows Weber's Law, e.g. Refs [43, 83, 11, 5, 10, 13, 29], which states that the smallest detectable change in a stimulus, known as the just-noticeable-difference, grows in direct proportion to the magnitude of the stimulus [28, 36]. Fechner developed a transformation from physical stimulus to what he called sensation magnitude by the assumption that a just-noticeable-difference in his sensation magnitude should

not vary with his sensation magnitude [23]. He did this for a system obeying Weber's Law and found his sensation magnitude then has a logarithmic dependence on physical stimulus magnitude without using statistical arguments. The logarithmic dependence is known as the Weber-Fechner Law.

Recent research notes a lack of quantitative evidence for how Weber's Law may provide advantages to a creature's survival [1, 49]. While a diverse literature exists on various hypothetical internal mechanisms of the visual systems that might lead to the observation of Weber's Law or its empirical approximations in historic psychophysical measurements, from the neurological and physiological [63, 50] to hypothetical internal noise within the visual systems [32, 67], these do not quantify nor delineate functional advantages Weber's Law may offer to a creature's survival in its environment.

Here we quantify how Weber's Law, Weber-Fechner's Law, and their empirical approximations from decades of psychophysical measurements made with artificial light, may be consistent with an evolutionary adaptation to attain statistically optimal intensity resolution, maximal information reception and optimal pattern recognition in naturally scintillating light. We first experimentally investigate the intensity scintillation statistics of natural light signals from thousands of environmental measurements, since these fluctuating intensities comprise the external input to the visual systems. These undergo natural fluctuation at every spatial pixel over repeated samples that is primarily from propagation and scattering through the random atmosphere and from terrestrial surfaces for light [87, 16]. We find the natural scintillation includes inherent signal-dependent noise where the intensity standard deviation or resolution footprint grows in proportion to the mean, as found in Weber Law. We then investigate the statistics of measured intensity after Fechner's sensation magnitude transformation. We do so using just-noticeable-differences that follow Weber's law exactly as well as those from psychophysical experiments making Fechner's sensation magnitude exactly and approximately log-transformed intensity, respectively. We find these Fechner sensation magnitude transformations consistently act as a variance stabilizing transformations and transformations to normality given our measured natural

light intensity scintillation.

We then find just-noticeable-differences in intensity from decades of psychophysical measurements with artificial light sources approximately attain the Cramer-Rao lower bound [74] on minimum mean square error in intensity estimation given natural scintillation of environmental light, and so are advantageously adapted to approximately attain optimal intensity resolution. We find the Cramer-Rao bound on intensity resolution follows Weber's law indicating Weber's Law is a consequence of optimal intensity resolution given the natural scintillation of environmental light from our measurements. From another perspective, to attain the Cramer-Rao bound or minimum mean-square error in intensity estimation, we find system resolution should be constant in variance-stabilizing-transformed intensity rather than in intensity given natural scintillation of environmental light and this leads to Weber's Law in intensity resolution without the need for hypothetical internal noise in the visual systems.

We then quantify pattern recognition performance using fundamental metrics of information, detection and estimation theory. The performance metrics include maximization of received information, true-positive pattern detection rate maximization, and pattern correlation error minimization. We experimentally and theoretically find that sensing with the intensity resolution found in the exact Weber's law, or that found empirically with just-noticeable-differences obtained from decades of psychophysical measurements with artificial light intensity, both lead to approximately optimal pattern recognition and maximal information reception given the natural fluctuations in environmental light intensity we measure. We find this is achieved by homeomorphic variance-stabilizing transformation of signal-dependent intensity scintillation typically found in natural environmental light, from random multiplicative factors, to additive signal-independent noise that tends to be normally distributed as a consequence of the central limit theorem. The resulting signal-independent noise can then be canceled without loss of signal information by simple pattern matching that requires only knowledge of the mean signal pattern to be recognized and not higher statistical moments. This pattern matching entails a linear matched filter correlation [14] in variance-stabilizing transformed intensity, which is equivalent

to log-transformed or Fechner's sensation-magnitude transformed intensity. We find this is not possible with untransformed scintillating light intensities, because noise that carries signal information is canceled by such a simple matched filter correlation in intensity, making it suboptimal. Also, the higher statistical moments of intensity vary for each signal and each pixel within the signal making them impractical to determine, for statistically optimal pattern recognition, without the equivalent of a variance-stabilizing transformation such as the Fechner sensation magnitude or log-transformation.

2.2 Results

Static scenes of natural objects including leaves, feathers, branches, earth, tree bark and stones were imaged thousands of times, every second over daytime hours. This was done to form different observations of the same scene changed at each pixel only by variations in natural lighting, which scintillated under varying atmospheric and cloud conditions. The statistical fluctuations of natural light at each pixel in respective intensity images were obtained using temporal, spatial and frequency samplings consistent with those found for the human visual (figure 2-1) system (Section 2.4).

2.2.1 Signal-Dependent Noise Found in Environmental Light Intensity with a Standard Deviation Proportional to the Mean

In each case we find intensity fluctuates with signal-dependent noise at each pixel such that the standard deviation characterizing the scale of fluctuations is approximately proportional to the mean intensity which defines the signal (figure 2-1b). In other words, the intensity standard deviation is a constant percentage of the mean. Noise is then directly dependent on the signal and so contains signal information. To eliminate noise, and not lose signal information, a variance-stabilizing transformation can be applied by requiring a differential element of the transformed intensity be

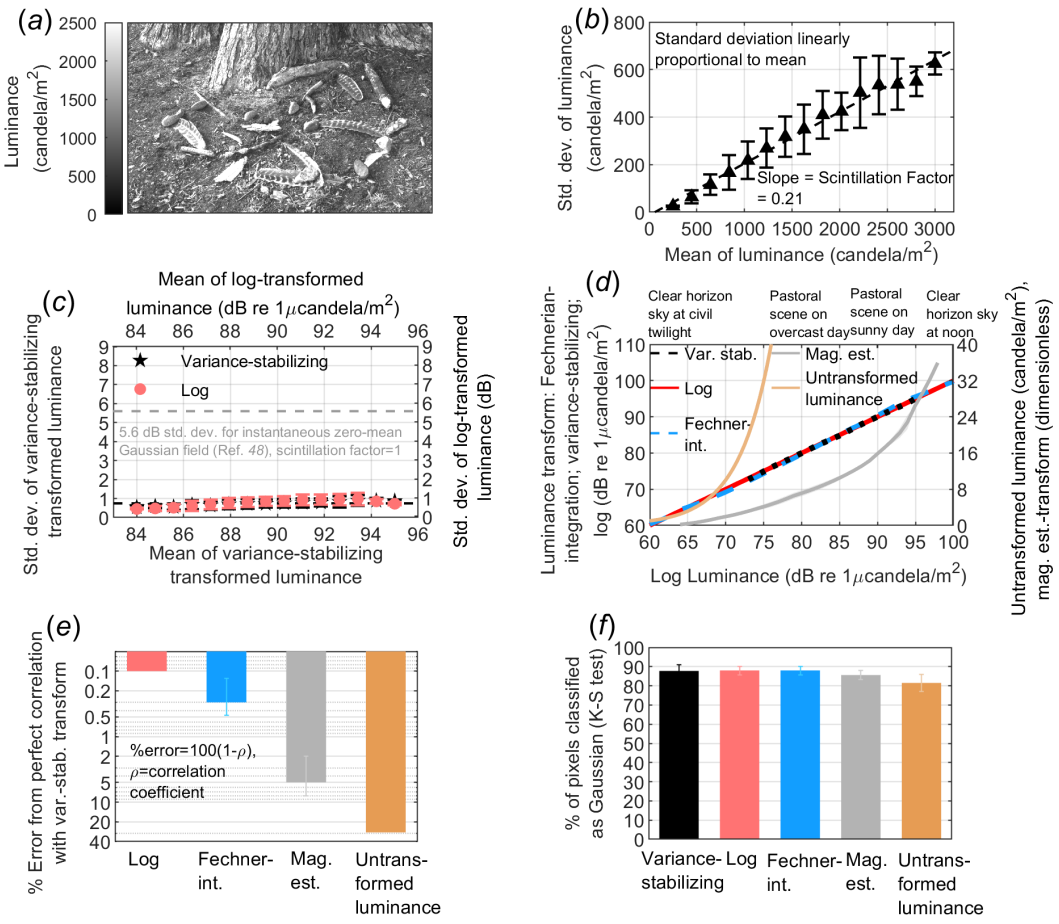

Figure 2-1: Signal-dependent scintillation in luminance of natural objects illuminated by fluctuating terrestrial daylight over repeated measurements is variance-stabilized to signal-independent noise by log-transformation or equivalently Fechnerian-integration transformation which also leads to normal statistics. (a) Single measurement sample of scene with static natural objects at 1 arc-minute resolution per pixel approximately that of human eye in luminance (spectrally filtered, normalized intensity). (b-f) Analysis for data in naturally scintillating daylight (51-69% varying cloud cover) at 1 s sampling of scene in a: (b) Standard deviation linear in mean for luminance. (c) Standard deviation constant function of mean for variance-stabilizing and log transformed luminance. (d) Intensity transforms versus log-intensity. variance-stabilizing transform is obtained from the measured luminance data, Fechnerian-integration and magnitude estimation transform derived from decades of independent psychophysical investigations [43, 83, 11, 13, 84, 69], for data above the rod range (Sections 2.4.2, 2.4.3). (e) Percent error from unity correlation with variance-stabilizing transform for each transform in d. (f) Percentage of normally distributed pixels from Kolmogorov-Smirnoff test (Section 2.4.4). Similar results are found under different cloud conditions (Appendix F figures F-2 to F-5).

constant and equal to the number of intensity standard deviations per differential element of mean intensity [3]. We consistently find such a variance-stabilizing transform derived from and applied to the measured intensity data of natural light is very well approximated by a logarithmic transform (figure 1*d*). They each homomorphically convert signal-dependent scintillation in the intensity data to signal-independent noise in the transformed data such that the standard deviation is approximately constant as a function of the mean after transformation (figure 2-1*c*) which defines variance-stabilization. Canceling noise that does not depend on the signal does not lose signal information.

2.2.2 Fechnerian-integration Transformation from Decades of Just-Noticeable-Difference Data is Highly Correlated with the Ideal Weber-Fechner Logarithmic Transformation Law

Interestingly, from decades of psychophysical measurements with controlled artificial light sources rather than natural ones, the smallest detectable change in intensity stimulus, known as the just-noticeable-difference obtained by human test subjects reflexively signaling this perceived change in external stimulus, also grows approximately in proportion to stimulating intensity for light intensity over the same ranges as our natural data (figure 2-2). They then approximately follow Weber's Law. When Weber's Law holds, Fechnerian integration of just-noticeable differences of a stimulus leads to a logarithmic transformation of the stimulus, known as the Weber-Fechner Law [23, 37, 46, 76, 65]. When derived from decades of psychophysical just-noticeable-difference data for light intensity, we find the Fechnerian integration transformation is very highly correlated with a log transformation as well as the variance-stabilizing transformation of stimulating intensity found empirically from our natural light data (figure 2-1*d*,*e*).

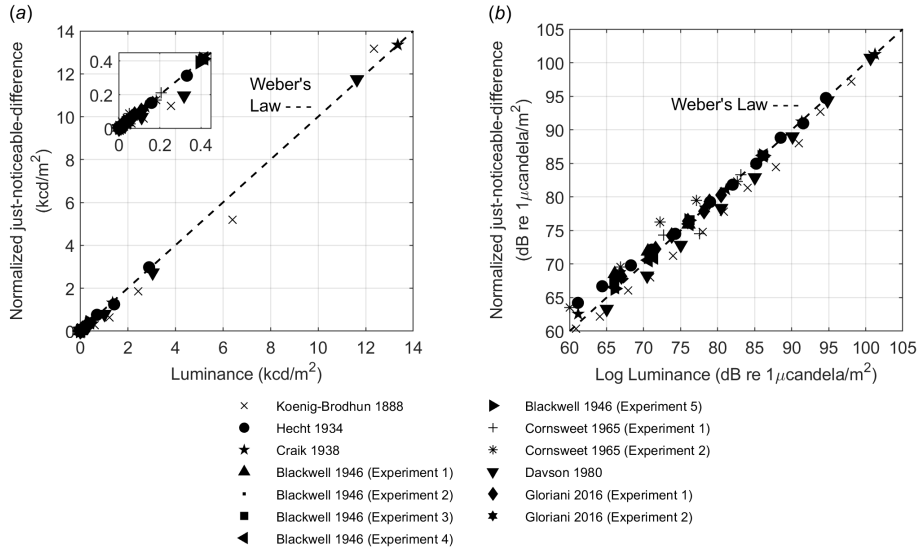

Figure 2-2: Just-noticeable-differences from decades of psychophysical measurements as a function of optical luminance approximately follow Weber's Law. (a) Normalized just-noticeable-differences vs luminance for luminance data obtained from decades of psychophysical experiments measuring human response to light intensity stimulus [43, 83, 11, 5, 10, 13, 29] over daylight range. Inset image shows magnification towards lower intensities. (b) shows the same plot in the log-log scale.

2.2.3 Fechnerian-integration Transformation Acts as a Variance-stabilizing Transformation for Environmental Light Intensity

Here we mathematically prove that when Weber's Law holds for psychophysical just-noticeable differences, and stimulating intensity has a standard deviation that grows in proportion to the mean, Fechnerian-integration transformation is a variance-stabilizing transformation. This equality has been shown to be approximately the case in Section 2.2 figures 2-1 and 2-2 with decades of psychophysical data and our measurement of thousands of intensity images made with natural light.

Fechnerian integration leads to an intensity transformation

$$T_F(I) = \int_{I_0}^{I} \frac{1}{\Delta I(\bar{I})}\, d\bar{I} \tag{2.1}$$

mathematically identical to variance-stabilizing transformation

$$T_V(I) = \alpha_0 \int_{I_0}^{I} \frac{1}{\sigma_I(\bar{I})}\, d\bar{I} \tag{2.2}$$

of intensity I, from minimum signal value I_0, when just-noticeable-differences $\Delta I(\bar{I})$ have the same functional dependence on mean intensity $\bar{I}$ as the standard deviation $\sigma_I(\bar{I})$ of natural light intensity I, to within a constant factor such that,

$$\sigma_I(\bar{I}) = \alpha_0 \Delta I(\bar{I}) \tag{2.3}$$

The equality $T_V(I) = T_F(I)$ is confirmed experimentally by the high correlation between measured variance-stabilizing transformations and Fechnerian-integration transformations obtained from decades of psychophysical measurements (figures 2-1i and 2-2e), which implies equation (2.3). Experimental confirmation of equation (2.3) is also seen by $\sigma_I(\bar{I})$ and $\Delta I(\bar{I})$ being directly proportional to $\bar{I}$ for light intensity in figures 2-1b and 2-2a. With Fechnerian-integration transformed intensity $S(I) = T_F(I)$, which may be interpreted as the perceived output of this transformation, and employing observed constancy of measured intensity scintillation factor $\frac{\sigma_I(\bar{I})}{\bar{I}} = \beta_0$ in equations (2.1-2.3) leads to the variance-stabilized solution for Fechnerian-integration transformed intensity

$$S(I) = \frac{\alpha_0}{\beta_0} log(I) + \gamma_0 \tag{2.4}$$

that is a logarithmic transform of received intensity stimulus, consistent with historic psychophysical measurements in figures 2-1h and 2-2d, and α_0, β_0 and γ_0 are constants.

2.2.4 Magnitude-estimation Transformations have Significantly Lower Correlation with Variance-stabilizing Transformation than Fechnerian-integration Transformations

We also investigate empirical psychophysical transformations of light intensity as quantified by a magnitude estimation process [84, 85]. Magnitude estimation requires test subjects assess and assign a numerical value to a perceived change in intensity stimulus, and so is affected by a further intellectual process beyond detecting and reporting a just-noticeable-difference [47]. Psychophysical transformations from physical intensity stimulus by magnitude estimation from decades of historical magnitude-estimation measurements also show significant but not so high a correlation as log or Fechnerian-integration transformations do with variance-stabilizing transformation (figure 2-1*d*,*e*). Here all psychophysical data are shown above the rod range for visual data to avoid special effects expected near these lowest detectable levels.

2.2.5 Approximate Normality of Variance-stabilizing-transformed Intensity

The variance-stabilizing, Fechnerian-integration and log transforms all have excellent performance in transforming the measured optical intensity data at each pixel to a variate with a normal probability density, as quantified by Kolmogorov-Smirnov testing, in figure 2-1*f*. The fit to normality is consistently cruder for magnitude estimation and consistently worst for no intensity transformation. This hierarchy is identical to that found in correlation with the variance-stabilizing transform (figure 2-1*e*). This is consistent with a correlation noted between variance-stabilizing transformations and transformations to normality found more generally in statistics [3, 12].

Lognormal intensity scintillation is routinely seen in starlight twinkling [87, 16] and also appears in sunlight due to random atmospheric effects [92, 80, 27]. The natural terrestrial daylight intensity scintillation we observe at any pixel (figure 2-1*b*)

arises from sunlight scattering through and from multiple random and independent atmospheric layers [87, 16, 92, 80, 27], including clouds, and subsequent directional scattering by the object into a directional sensor such as the eye. Log transformation of intensity homomorphically converts random independent multiplicative factors to additive ones [86, 62]. This leads to a log-intensity standard deviation that is independent of the signal-bearing mean (figure 2-1c) as well as convergence to a lognormal intensity probability density by the central limit theorem. Adjustment to the average image level in any instantaneous image has precedent in observed visual system threshold shifting [81] and is here accomplished simply by its subtraction. This leaves only the pattern with any distortions from nonuniform lighting fluctuations across repeated samples of the image when perceived in variance-stabilizing, log, or Fechnerian-integration transformed intensity. The corresponding fluctuations at any pixel relative to the instantaneous average level of the image are found to converge to a normal distribution for all transforms effective at variance stabilization (figure 2-1f) and tend to become free from correlation with other pixels (Section 2.4.7), with standard deviations that remain constant across the transformed variable and independent of the mean that have greater stability across atmospheric conditions.

2.2.6 Statistically Optimal Intensity Resolution Leads to Weber's Law for Natural Scintillating Environmental Light Data

Given the approximate normality of log-transformed intensity found for natural scintillating environmental light with a variance independent of the mean (figure 2-1), the Cramer-Rao Lower Bound (CRLB) or minimum variance on intensity resolution for a single random intensity sample I [74] is

$$CRLB(I) = \sigma^2_{log(I)} \Big(\frac{dlog(\bar{I})}{d\bar{I}} \Big)^{-2} \tag{2.5}$$

where $\sigma_{log(I)}$ is the standard deviation of log-transformed intensity, which is independent of mean intensity $\bar{I}$, and inverse of the CRLB in equation (2.5) is the Fisher information [74] for intensity sample I. The smallest possible standard deviation in an unbiased intensity estimate with this sample must then be greater than or equal to

$$\sqrt{CRLB(I)} = \sigma_{log(I)}\bar{I} \tag{2.6}$$

which is proportional to mean intensity. The square root of the Cramer-Rao lower bound, minimum root-mean-square intensity estimation error or the optimal intensity resolution, of naturally scintillating environmental light intensity then follows Weber's law according to our measurements (figure 2-3).

Remarkably, just-noticeable-differences in intensity in psychophysical measurements with artificial light (figure 2-2) are found to be approximately equal to the minimum realizable root-mean-square error in intensity estimation, namely the Cramer-Rao lower bound of equation (2.6) (figure 2-3a) found from our naturally scintillating environmental light intensity data (figure 2-1) which follows Weber's Law. They can be interpreted as resolution thresholds that yield true positive rates for detection of a change in intensity of 92$\pm$10% for optical data, consistently for all mean intensities measured (figure 2-3b). In contrast, if just-noticeable-differences or intensity resolution did not vary with mean intensity as in Weber's Law but were set to be constant across mean intensity, true positive detection rates of intensity, and their corresponding reliability, vary drastically with mean intensity. Such non-uniform errors lead to significant inefficiencies in sensing system performance. Optimal intensity resolution so requires system resolution be constant in variance-stabilizing transformed intensity rather than in mean intensity.

Equivalently, by a simple one-to-one transformation of random variables, optimal sensing resolution must be constant in variance-stabilizing-transformed intensity, which we have found is approximately the same as log-transformed intensity from

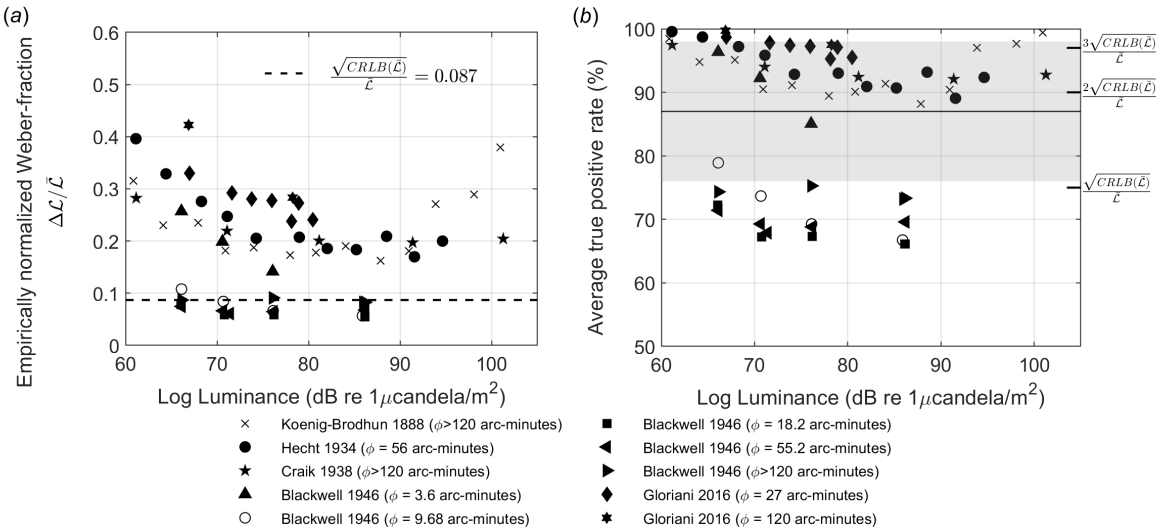

Figure 2-3: Psychophysical just-noticeable-differences in artificial light intensity resolution approximately attain the Cramer-Rao bound for natural light scintillation with corresponding true positive detection rates. (a) Just-noticeable-differences vs intensity for luminance data obtained from decades of psychophysical experiments measuring human response to light intensity stimulus [43, 83, 11, 5, 10, 13, 29] with just-noticeable-differences adjusted to single pixel angular resolution of the visual system (Section 2.4.6). Cramer-Rao lower bound of equation (2.6) is computed with measured log-transformed luminance probability densities from natural objects in figure 2-1a. Cramer-Rao lower bounds for other cloud conditions (Appendix F) are within 20% of this bound. (b) Average true positive detection rate across all false positive rates for intensity change equal to psychophysically measured just-noticeable-differences with artificial light given probability density of naturally scintillating light.

our measurements (figure 2-1c). It can be readily proven since the Cramer-Rao bound or minimum root-mean-square error for a single sample random sample of log-transformed intensity $log(I)$ is

$$\sqrt{CRLB(log(I))} = \sigma_{log(I)} \tag{2.7}$$

which is a tight bound equal to the standard deviation of $log(I)$ which we find is independent of $\bar{I}$ as shown in figure 2-1c. The best possible resolution of log-transformed intensity is then a constant independent of mean intensity $\bar{I}$. This is consistent with the log-transform behaving as a variance stabilizing transformation and a transformation to normality (figure 2-1).

2.2.7 Maximization of Received Information and Signal-to-Noise Ratio in Variance-stabilizing-transformed Intensity Data

The likelihood function, namely the probability density function governing the scintillation of image intensity evaluated at all measured intensities at each pixel, contains all information in the image data required for pattern recognition, pattern parameter estimation and pattern detection according to information, estimation and detection theories [14, 24]. For multivariate normal image data, which is consistently found here for our natural light intensity measurements after effective variance-stabilizing transformation, including log-transformation, (figure 2-1f), the likelihood function has advantages in requiring only knowledge of the expected or mean signal pattern to be detected to within a constant factor. This is because the covariance of the image data with maximum likelihood is found to have the generic signal-independent form of a scaled identity matrix [14] (Section 2.4.7). Assuming a normal likelihood function, we consistently find that transformations of intensity that are highly correlated with variance-stabilizing transformation lead to maximum and significantly higher mean likelihood than with the fluctuating intensity of natural light (figure 2-4a).

2.2.8 Optimal Pattern Recognition with Variance-stabilizing-transformed Intensity Data

A sufficient statistic, containing all the information in the image data needed for optimal pattern recognition by hypothesis testing, is then a simple and intuitive linear correlation between an expected pattern and a measured one known as a matched-filter [14, 66]. Remarkably, no higher statistical moments are necessary beyond the first, namely the mean pattern (Section 2.4.7). This is extremely advantageous because it requires the most minimal statistical sampling of the environment possible, which can be performed rapidly in hostile or competitive environments. This simple form for the sufficient statistic then only requires natural light intensity images

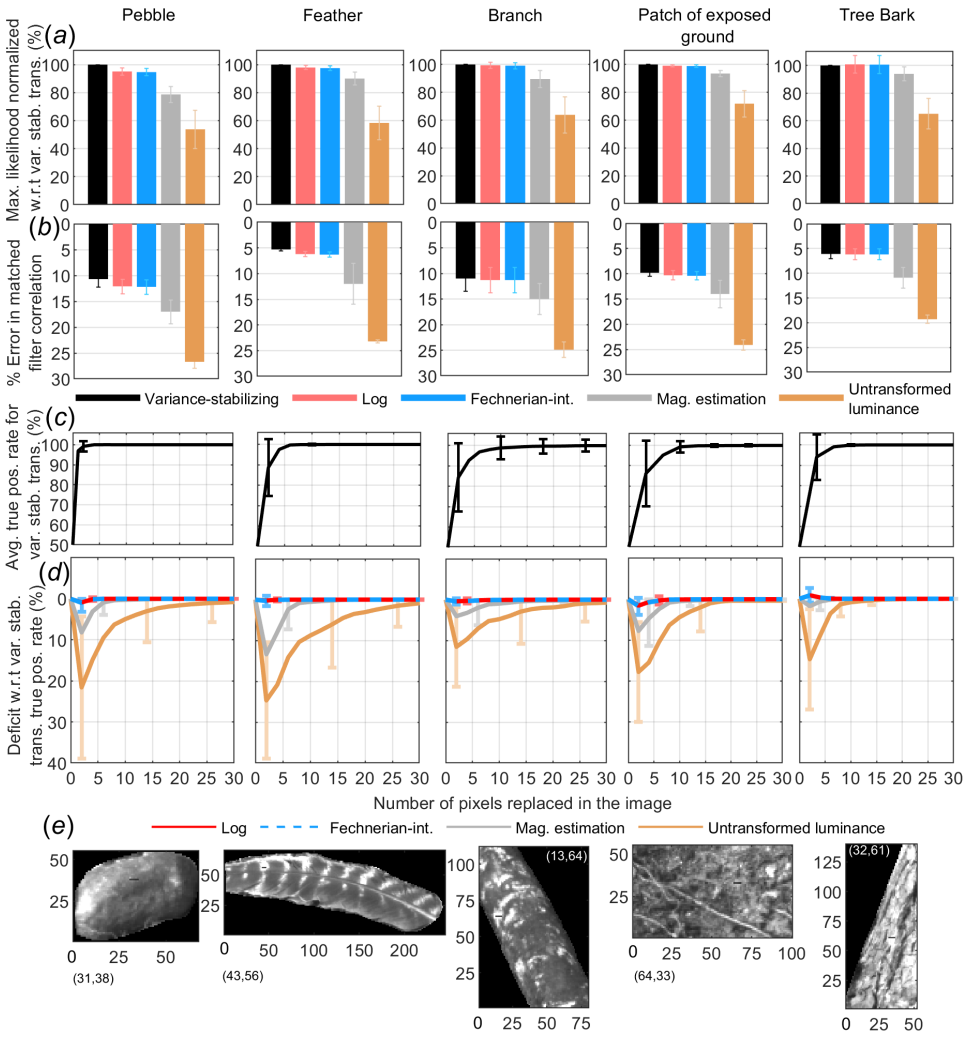

Figure 2-4: Information reception and pattern recognition performance compared across transforms of natural scintillating luminance images of objects in daylight. (a) Maximum of the likelihood function across transforms for objects indicated illuminated with daylight and imaged as in figure 2-1, where H_0 uses 4500 snapshots of each object, H_1 a different 4500 snapshots. Multivariate normal image probability density function first assumed for intensity and all intensity transforms, then converted to common unit for quantitative likelihood comparison with measured data, normalized by variance stabilizing likelihood and image sample sizes (Appendix H). (b) Percentage error for matched filter correlation across all event trials and signatures, error is standard deviation-to-mean ratio. (c-e) Hypothesis testing between null (H_0) and alternate hypothesis (H_1) over distinct trials of same object where the number of adjacent linear horizontal pixels indicated in c-d are replaced with dark earth pixels over all possible locations for each object and trial. (c) Average true positive rate across all false positive rates for variance-stabilizing transformed intensity, H_1 and H_0 indistinguishable to completely distinguishable as number of changed pixels increases. (d) Percent deficit from variance-stabilizing performance in c for other transforms of same intensity data. (e) Example of H_1 image for each object with 5 pixels replaced starting at given coordinate. Similar results are found under different cloud conditions (Appendix F).

undergo a transform that is highly correlated with a variance-stabilizing transform, such as Fechnerian-integration and log, to transform the data to normality and eliminate signal-dependent noise. In such matched filter pattern correlation, intensity transforms more effective at variance-stabilization and conversion to normality (figure 2-1f) have lowest percent correlation error and corresponding highest signal-to-noise ratio, which is the inverse square of the fractional correlation error, when applied to our optical data (figure 2-4b). Intensity transformations most effective at variance-stabilization (figure 2-1e) and transformation to normality (figure 2-1f) as expected perform best in optimal hypothesis testing (figure 2-4c,d), which yield the highest true-positive detection rate possible for a receiver's given false-positive rate [74, 14, 66]. Variance-stabilizing, log and Fechnerian-integration transformation yield nearly identical and best pattern recognition, far better than untransformed intensity, while magnitude estimation transformation has consistently poorer performance than all other transformations but tends to perform better than untransformed intensity (figure 2-4c,d). The far less optimal performance of magnitude estimation transformation may arise from judgment processes that are unnecessary in perceiving just-noticeable-differences in intensity. The just-noticeable-difference metric has the advantage of being quantifiable as a standard and practical physical unit, namely the incident power per unit area on a sensor.

The optimal hypothesis tests employed are designed to quantify advantages of an intensity transform trait that enables increasingly subtler pattern changes to be reliably detected. Pattern change detection is tested between an image and the same image with a patch of pixels replaced by dark natural material in the visual examples (figure 2-4e). The visual patch, for example, could contain information about a potential food source or harmful pest. The visual patch would be lost in signal-dependent noise, go frequently undetected and so lead to potentially significant disadvantages to organisms, systems or machines that do not employ variance-stabilizing, log or empirically determined Fechnerian-integration transformation of intensity before pattern matching (figure 2-4c,d) or the equivalent.

2.3 Discussion and Conclusion

These experimental and theoretical findings quantitatively show intensity resolution that obeys Weber's Law, or its approximations from decades of psychophysical just-noticeable-difference data obtained with artificial light, is advantageous as a trait in visual sensing given environmental intensity scintillation in natural light. This natural scintillation has predictable properties converged upon by the central limit theorem from diverse physical mechanisms that make such adaptation possible. Sensing resolution that follows Weber's Law is found to be necessary to attain Fisher's minimum mean-square error, or the Cramer-Rao lower bound, in intensity estimation given the natural scintillation of environmental light we measure. Observation of Weber's law does not require hypothetical internal sensing system noise as an explanation. We also find just-noticeable-differences in light intensity from decades of psychophysical measurements with artificial light sources approximately attain the respective Cramer-Rao lower bounds on minimum possible intensity estimation error expected from natural light scintillation and so are to a good approximation optimally adapted to these environmental fluctuations with Weber's Law as a consequence.

Transformation from physical intensity to Fechnerian-integration transformed intensity by the Weber-Fechner logarithmic law or a close empirical correlate of it behaves as a variance-stabilizing transformation that homomorphically converts multiplicative signal-pattern-dependent scintillation received to signal-pattern-independent and normally distributed noise perceived that can be optimally canceled without loss of signal information. After this transformation, which follows from Weber's Law in intensity resolution and consequently constant system resolution in variance-stabilizing transformed intensity, only the measured fluctuating pattern and the expected pattern stored in memory are needed to maximize received information, minimize recognition error and maximize true positive pattern detection rate. Without such variance-stabilizing transformation or equivalent 'hard wired' system adaptation or tuning to the underlying scintillation statistics of natural terrestrial light, optimal pattern recognition would require expensive sampling and learning of the

higher statistical moments of every signal pattern to be recognized due to the inherent signal-dependent noise of the intensity scintillation at each pixel. This extensive sampling and training requirement is impractical in a hostile or highly competitive environment where rapid and accurate sensing is essential and is unnecessary given the advantageous properties of the simple variance-stabilizing transformations described here.

Along these lines, the standard practice of measuring such scintillating intensity data with decibel units in acoustics, optics, radar and other scientific and engineering disciplines is analogous to a variance-stabilizing transformation or a Fechnerian-integration transformation that enables optimal pattern recognition via simple linear unweighted correlation by virtue of the central limit theorem [56, 55, 90, 59, 58].

2.4 Materials and Methods

2.4.1 Luminance Measurements of Natural Objects Imaged with Natural Light

A static scene with natural objects was imaged with natural scintillating daylight with a Phantom UHS12 camera which provided 12 bit depth or 4096 discrete luminance values at each pixel of a 1280 by 800 image, where the angular resolution of each pixel was approximately 1 arc-minute, similar to that of the human eye [52]. The entire scene was measured every second over two and a half hours at midday in Massachusetts under partly sunny sky conditions with 51% to 69% varying cloud cover leading to $N = 9000$ complete images of the entire scene. Luminance data at any pixel (x, y) in the j^{th} measurement of the entire scene is denoted as $\mathcal{L}_j(x, y)$, where the corresponding log-transformed luminance is $T_L(\mathcal{L}_j(x, y)) = 10log_{10}\left(\frac{\mathcal{L}_j(x,y)}{\mathcal{L}_{ref}}\right)$ dB re $\mathcal{L}_{ref} = 1\mu candela/m^2$, variance-stabilizing transformed luminance is $T_V(\mathcal{L}_j(x, y))$, Fechnerian-integration transformed luminance is $T_F(\mathcal{L}_j(x, y))$ and magnitude estimation transformed luminance is $T_{ME}(\mathcal{L}_j(x, y))$. Let $T(\mathcal{L}_j(x, y))$ be some transform of luminance, then

$$\tau(\mathcal{L}_j(x,y)) = T(\mathcal{L}_j(x,y)) - \frac{1}{N_x N_y}\sum_{x=1}^{N_x}\sum_{y=1}^{N_y} T(\mathcal{L}_j(x,y)) \tag{2.8}$$

is the corresponding transformed luminance of the j^{th} luminance image minus the average level over all pixels in that image, which does not alter the pattern, and $N_x N_y$ is the number of pixels. The coherence time scale or autocorrelation e-folding time scale of log-transformed luminance image minus the average level over all pixels in that image, which does not alter the pattern, across consecutive measurements j is found to be roughly 55 s and is primarily due to changes in atmospheric conditions including cloud variation, with similar values found for the various other transforms of luminance. Since this coherence time is much larger than the roughly 10-15 ms integration time of the visual system [52], a 1 s sampling interval over hours is more than sufficient to adequately describe the relevant scintillation statistics. The mean signal $\bar{\mathcal{L}}(x,y)$ and standard deviation $\sigma_{\mathcal{L}}(x,y)$ are computed at any pixel over all $j = 1, 2, 3, ...N$ measurements of the entire scene $\mathcal{L}_j(x,y)$ shown in figure 2-1a. The mean $\bar{\mathcal{L}}(x,y)$ and standard deviation $\sigma_{\mathcal{L}}(x,y)$ data across pixels (x,y) are sorted to obtain standard deviation as a function of mean luminance $\sigma_{\mathcal{L}}(\bar{\mathcal{L}})$ in figure 2-1b. Similarly, the standard deviation vs mean of the log transformed luminance $T_L(\mathcal{L}(x,y))$ and that for the variance-stabilizing transformed data $T_V(\mathcal{L}(x,y))$ is shown in figure 2-1c. Nearly continuous mean luminance levels $\bar{\mathcal{L}}$ and mean transformed luminance levels from the data are uniformly sampled at discrete points for presentation purposes only in figure 2-1b and figure 2-1c respectively. Similar results are obtained for objects shown in Appendix figure F-1 and for scenes illuminated on other days with different natural daylight conditions, ranging from sunny, partly sunny to overcast skies as shown in Appendix F, figures F-3 to F-5.

A threshold adjustment is applied to any instantaneous untransformed or transformed luminance image by subtracting the average image level which leaves only the pattern with no additive offsets (equation (2.8)). $T_L(\mathcal{L}_j(x,y))$, $T_V(\mathcal{L}_j(x,y))$, $T_F(\mathcal{L}_j(x,y))$, $T_{ME}(\mathcal{L}_j(x,y))$ and $\mathcal{L}_j(x,y)$ represent offset adjusted luminance data

at pixel (x,y) for the j^{th} measurement following equation (2.8) for log, variance-stabilizing, Fechnerian-integration, magnitude estimation transformation of luminance as well as untransformed luminance respectively. This simple offset adjustment does not affect the relative performance hierarchy of the various transforms of luminance data shown in figure 2-4, but is advantageous because it does enable the covariance matrix to be a scaled identity matrix and leads to a higher percentage of Gaussian pixels in figure 2-1*f*. We also find that the standard deviation of offset adjusted log-transformed luminance data $T_L(\mathcal{L}_j(x,y))$ averaged across pixels (x,y) is relatively stable across different atmospheric conditions with values of 0.378 dB, 0.252 dB and 0.391 dB for scenes illuminated on days with partly sunny, sunny and overcast sky conditions respectively. Offset adjustment is only applied for the analysis shown in figure 2-1f and not in the preceding figure 2-1(a-e).

2.4.2 Psychophysical transforms

Fechnerian-integration

Empirical Fechnerian-integration transforms for the visual system (figures 2-1 and 2-4) are obtained from decades of psychophysical experiments measuring human response to light intensity [43, 83, 11, 13] stimulus by Fechnerian integration [37, 46, 76] of just-noticeable-differences ΔI in intensity [65, 47, 26]

$$S_i(I) = c_0 \int_{I_0}^{I} \frac{1}{\Delta I_i(\bar{I})} d\bar{I} \tag{2.9}$$

where $S_i(I)$ is Fechnerian-integration transformed intensity [65] for the i^{th} of N_F historic measurements of just-noticeable-differences $\Delta I_i(\bar{I})$ as a function of input intensity $\bar{I}$ stimulus, I_0 is the minimum signal intensity, and c_0 is a constant.

Empirical just-noticeable-difference functions $\Delta\mathcal{L}_i(\mathcal{L})$ from $i = 1, 2, 3...N_F^{\mathcal{L}} = 4$ independent tests [43, 83, 11, 13] yielded $i = 1, 2, 3...N_F^{\mathcal{L}} = 4$ Fechnerian-integration

transformed intensity curves $S_i(\mathcal{L})$ via equation (2.9), where $I = \mathcal{L}, I_0 = \mathcal{L}_0$, and $\Delta I_i(\bar{I}) = \Delta\mathcal{L}_i(\bar{\mathcal{L}})$, and $T_{F_i}(\mathcal{L}) = S_i(\mathcal{L})|_{c_0=1}$ for $i = 1, 2, ..., N_F^{\mathcal{L}}$ are the Fechnerian-integration transforms for the optical case used in figure 2-1*e,f* and figure 2-4. Only historic measurements of $\Delta\mathcal{L}(\mathcal{L})$ that cover the range of our optical luminance data from 73 to 95 dB re $1\mu candela/m^2$ are used in obtaining $S_i(\mathcal{L})$. Fechnerian-integration transformed intensities from Fechnerian integration of historic just-noticeable-differences $\Delta\mathcal{L}(\mathcal{L})$ that lie below the range of our luminance data but above the operational range of the rod system, i.e. roughly luminance $\mathcal{L} > 1$ $candela/m^2$, still have an average correlation of 0.98 with the log transformation within their respective luminance ranges. For plotting in figure 2-1*d* only, the mean and standard deviation over i of $S_i'(\mathcal{L}) = a_1 S_i(\mathcal{L}) + b_1$ are determined and shown in figure 2-1*d*, where a_1 and b_1 are normalization constants such that $S_i'(\mathcal{L})|_{\mathcal{L}=60 \text{ dB re } 1\mu candela/m^2} = 60$ and $S_i'(\mathcal{L})|_{\mathcal{L}=100 \text{ dB re } 1\mu candela/m^2} = 100$. The normalization constants a_1, b_1 are chosen so that $S_i'(\mathcal{L})$ can be visually compared with other transforms shown in figure 2-1*d*.

Magnitude estimation

Empirical Magnitude Estimation transforms for the visual system (figures 2-1 and 2-4), are obtained from decades of psychophysical experiments measuring human response to light intensity [84, 69] stimulus respectively, via subjective magnitude estimation method [26]. As in the Fechnerian-integration case, only historic measurements that roughly cover the range of our optical luminance data from 73 to 95 dB re $1\mu candela/m^2$ are used in obtaining magnitude estimation transforms as a function of intensity W and luminance $\mathcal{L}$ respectively.

Psychophysical experiments using magnitude estimation method from $i = 1, 2$ independent tests [84, 69] yielded $i = 1, 2$ magnitude estimation transforms $T_{ME_i}(\mathcal{L})$ as a function of input luminance $\mathcal{L}$ stimulus. The mean and standard deviation of $T_{ME_i}(\mathcal{L})$ over i are plotted in figure 2-2*d*. As in the Fechnerian-integration case, only historic measurements that cover the range of our optical luminance data from 73 to 95 dB re $1\mu candela/m^2$ are used in obtaining magnitude estimation transforms, which restricts the number of curves used in this case.

2.4.3 Variance-stabilizing transform

For random variable I with mean $\bar{I}$ and standard deviation σ_I that depends on this mean, a variance-stabilizing transformation leads to the random data variable [15]:

$$T_V(I) = a_0 \int_{I_0}^{I} \frac{1}{\sigma_I(\bar{I})} d\bar{I} + b_0 \tag{2.10}$$

that has standard deviation $\sigma_{T_V} = \sqrt{\langle T_V^2 \rangle - \langle T_V \rangle^2}$ independent of the mean , where I_0 is the minimum signal value, and constants a_0 and b_0 have no effect on variance stabilization.

Variance-stabilizing transformation $T_V(\mathcal{L})$ for optical luminance data is obtained via equation (2.10) with $I = \mathcal{L}, \bar{I} = \bar{\mathcal{L}}, I_0 = \mathcal{L}_0$ and $\sigma_I(\bar{I}) = \sigma_{\mathcal{L}}(\bar{\mathcal{L}})$. Constants a_0 and b_0 are chosen such that $T_V(\mathcal{L})|_{\mathcal{L}=60 \text{ dB re } 1\mu candela/m^2} = 60$ and $T_V(\mathcal{L})|_{\mathcal{L}=100 \text{ dB re } 1\mu candela/m^2} = 100$ for the purpose of visual comparison with the other transforms shown in figure 2-1*d*.

In figure 2-1*d*, variance-stabilizing transform curves $T_V(\mathcal{L})$ obtained from three days of image measurement under different sky conditions, i.e sunny, partly sunny and overcast, are scaled, normalized via equation (2.10) and combined over the full luminance range of data from 73 to 95 dB re $1\mu candela/m^2$. The combined curve is obtained by concatenating the individual variance-stabilizing transform curves and averaging over any region of overlap between the curves. Results in figures 2-1*f* and 2-4 for the variance-stabilizing transformed luminance data of the partly sunny day are evaluated with the variance stabilizing curve shown in figure 2-1*d*.

2.4.4 Kolmogorov-Smirnov test for Gaussianity

In figure 2-1*f*, the Kolmogorov-Smirnov (K-S) test [44, 82] for Gaussianity is applied.

For the optical data, $G(x, y)$ denotes an empirical random image where $G_j(x, y)$ is the j^{th} measured sample of the entire image that is offset-adjusted as described in equation (2.8), after any of the transformations of luminance or with untransformed

luminance. The K-S test at 5% significance level is individually applied to each pixel (x, y) in image $G_j^O(t)$ of object O, where object O could be any of the ones shown in figure 2-4*e*, namely pebble, feather, branch, exposed ground and bark. Offset adjustment is done for each object O individually by subtracting the instantaneous levels by the average level over all pixels within that object. For each object, the fraction of pixels that pass the test can be obtained as $q_g^O = 100\frac{N_g^O}{n^O}$, where N_g^O denotes the number of Gaussian pixels and n^O is the total number of pixels within the object. Figure 2-1*f* shows the mean $\bar{q_g}$ and standard deviation σ_{q_g} across objects.

The K-S test as applied in figure 2-1*f* requires the number of independent observations N_{ind} of the random image used to form the empirical distribution. For the optical data, the number of statistically independent observations N_{ind} due to natural lighting fluctuation is estimated from the sample autocorrelation function of $T_L(\mathcal{L}_j(x,y)) - \frac{1}{N_x N_y}\sum_{x=1}^{N_x}\sum_{y=1}^{N_y} T_L(\mathcal{L}_j(x,y))$ for pixel (x, y) across measurements in j. The fluctuations of the autocorrelation function at lags away from zero, where the correlation peak occurs, form a normal distribution with zero mean and variance given by the reciprocal of the number of independent observations [7]. By finding the stable bound, Δ, of the autocorrelation function at lags away from zero that leads to a 95% confidence interval, the number of independent observations can be computed as $N_ind = (\frac{1.96}{\Delta})^2$. Similar results are also obtained by dividing the total measurement time by the e-folding autocorrelation time of $T_L(\mathcal{L}_j(x,y)) - \frac{1}{N_x N_y}\sum_{x=1}^{N_x}\sum_{y=1}^{N_y} T_L(\mathcal{L}_j(x,y))$.

For Fechnerian-integration and magnitude estimation, individual transform curves across respective independent psychophysical studies are independently applied to the data to perform the K-S test, so that resultant mean and standard deviations across independent psychophysical studies are presented in figure 2-1*f*.

2.4.5 Empirical just-noticeable-difference functions

Empirical just-noticeable-difference functions $\Delta\mathcal{L}_i(\mathcal{L})$ of luminance $\mathcal{L}$ from $i = 1, 2, 3...N_F^{\mathcal{L}} = 13$ independent tests measuring human response to light intensity stimulus [43, 83, 11, 5, 10, 13, 29] are plotted in linear-linear scale in figure 2-2*a* and in log-log scale

for increased visual clarity in figure 2-2b. Only just-noticeable-differences $\Delta\mathcal{L}$ above the operating range of rod system, i.e. roughly luminance $\mathcal{L} > 1$ $candela/m^2$, are shown in figures 2-2a and 2-2b. The just-noticeable-difference function, $\Delta\mathcal{L}_i(\mathcal{L})$ in the optical case, from each independent test i is scaled by a constant such that the slope of the best-fit line through the normalized just-noticeable-differences is 1.

2.4.6 Just-noticeable-differences from Psychophysical Measurements with Artificial Light Sources and Their Normalizations

Just-noticeable-differences $\Delta\mathcal{L}_i$ in luminance $\mathcal{L}$ obtained from $i = 1, 2, 3...10$ independent tests measuring human response to light intensity stimulus [43, 83, 11, 5, 10, 13, 29] are compared in figure 2-3a with adjustments to compensate for differences in the size of the illuminated patch used for the stimulus. From Blackwell's measurements of just-noticeable-difference functions $\Delta\mathcal{L}_i(\mathcal{L})$ for different visual patch sizes [5], we find the slope of the best fitting line to the just-noticeable-difference data $\Delta\mathcal{L}$ approximately has a power-law dependence on stimulating patch size diameter D, such that the slope is proportional to $D^{-0.5}$ (Appendix F, figure F-6). We then multiply the original measured just-noticeable-differences $\Delta\mathcal{L}_i$ for each independent test i with corresponding stimulus diameter D_i by $(D_i/D_e)^{0.5}$ to obtain the just-noticeable-differences empirically adjusted to D_e, where D_e is approximately 1 arc-minute or roughly the resolution of the eye. We observe the effect of stimulus diameter on measured just-noticeable-differences to hold true up to stimulus diameter of 2 degrees. When stimulus diameter is greater than 2 degrees, we find just-noticeable-differences do not vary with stimulus size. This could be attributed to spatial integration limit of independent intensity changes to foveal vision which spans about 2 degrees of the visual field from the center of gaze [51], where fovea is the region of maximum resolution. Spatial integration for the measured just-noticeable-differences where stimulus diameter is greater than 2 degrees, such as for Refs [43, 11], is then limited to 2 degrees, such that the effective stimulus diameter is taken to be 2 degrees, and the

corresponding just-noticeable-differences are then normalized to the resolution of the eye. References that do not provide stimulus diameter have been excluded as there is insufficient information to quantitatively compare the just-noticeable-differences.

To obtain figure 2-3b, two competing hypotheses H_0 and H_1 which are normally distributed are considered. From K-S test results, log-transformed intensity at any pixel is approximately normal (figure 2-1f). Empirically adjusted just-noticeable-difference functions $\Delta\mathcal{L}_i(\mathcal{L})(D_i/D_e)^{0.6}$ of luminance $\mathcal{L}$ from $i = 1, 2, 3...10$ independent tests measuring human response to light intensity stimulus [43, 83, 11, 5, 10, 13, 29] are used to obtain the alternate hypothesis H_1 such that H_0 is a normal distribution with mean $log(\mathcal{L})$ and standard deviation $\sigma_{log(\mathcal{L})}$ which is an average standard deviation for log-transformed luminance $log(\mathcal{L}(x, y))$ after offset adjustment, across all pixels (x, y) and different objects on the partly sunny day. H_1 is a normal distribution with mean $log(\mathcal{L} + \Delta\mathcal{L}_i(\mathcal{L})(D_i/D_e)^{0.6})$ and the same standard deviation as H_0. Average true positive rates obtained as area under the receiver operating characteristic (ROC) across all false positive rates are shown in figure 2-3b as a function of intensity or luminance.

Average true positive detection rates for luminance data of scenes under different cloud conditions are $96 \pm 6\%$ for Appendix F figure F-2a scene and $92 \pm 10\%$ for Appendix F figure F-4a scene.

2.4.7 Log-likelihood function

Let $\mathbf{G}_j$ be an n-dimensional vector of transformed or untransformed intensity over the n pixels of the optical image for the j^{th} image sample. For the optical image data, $\mathbf{G}_j$ is the vectorized form of the 2D offset-adjusted transformed or untransformed luminance image. $\mathbf{G}_j$ is assumed to be a particular measurement of a multi-variate normal random vector $\mathbf{G}$ with mean $\bar{\mathbf{G}}$ and covariance C.

The covariance for offset adjusted luminance and transformed luminance images is well approximated by a diagonal matrix, with a mean correlation coefficient magnitude between any two distinct pixels roughly 0.02 over all objects. For variance-stabilizing, log and Fechner-sensation transformed acoustic intensity and optical lu-

minance images, the covariance matrix is well approximated by $C = \sigma^2 I$, where I is the identity matrix of size nxn, where n is the number of pixels and σ^2 is a signal-independent parameter. Following the standard definition of a Gaussian likelihood function, the log-likelihood function is obtained as:

$$l(\bar{\mathbf{G}}, \sigma^2) = \sum_{j=1}^{N} \Big\{ -\frac{1}{2}\frac{(\mathbf{G}_j - \bar{\mathbf{G}})^T(\mathbf{G}_j - \bar{\mathbf{G}})}{\sigma^2} - \frac{n}{2} log(\sigma^2) \Big\} + d \qquad (2.11)$$

where the signal-independent scaling parameter σ^2, equivalent to the variance at any pixel, is obtained via maximum likelihood estimation with sample image data $\mathbf{G}_j$ for $j = 1, 2, ...N$, and $d = -N(\frac{n}{2})log(2\pi)$ is a constant.

The generic covariance structure follows because image data is uncorrelated on average for the optical data when perceived relative to the instantaneous average image level. The diagonal elements are constant because all signal-specific variance-stabilizing transforms for our optical data are highly correlated with a generic logarithmic transform, as are the empirical Fechnerian-integration transforms, (figure 2-1(d-e)), and so yield covariances that tend to converge to a generic form. The scaled identity matrix covariance also has advantages in its stability, predictability, generality and simplicity to implement.

The purpose now is to use the method of maximum likelihood to quantify which transform produces the maximum likelihood given our measured optical data under the Gaussian assumption with uncorrelated covariance structure of equation (2.11). Likelihood functions computed for each transform have the same units as probability density functions. The likelihoods they quantify, including the maximum likelihood across transforms, for the same data and the uncorrelated multivariate Gaussian model in that transform domain can then only be compared when the respective probability density functions are either in or are converted to the same base transform. Since each of the transforms considered here are one-to-one functions of one another (figure 2-1d), we use the rule for transformation of random variables [14] to covert probability density functions in any transform such as untransformed intensity to a

common base transform, which is chosen to be the variance-stabilizing transform. Section III in electronic supplementary material provides a detailed description of the maximum likelihood comparison across transforms.

2.4.8 Percentage error of a simple matched filter

For a given measurement j of the entire image, the squared Mahalanobis distance [74] $\frac{(\mathbf{G}_j-\bar{\mathbf{G}})^T(\mathbf{G}_j-\bar{\mathbf{G}})}{\sigma^2}$, from the log-likelihood function in equation (2.11), is a sufficient statistic for estimating parameters contained in the mean $\bar{\mathbf{G}}$ (Ref [42]) including signal patterns. The simpler matched filter correlation $M_j = \mathbf{G}_j^T\bar{\mathbf{G}}$, which is the cross term in the squared Mahalanobis distance without the scale factor σ^2, is a sufficient statistic for pattern recognition via optimal Neyman-Pearson hypothesis testing as shown in the following section. With all realizations $j = 1, 2...N$, an empirical distribution can then be found for M. The ratio of standard deviation of M, σ_M, to its mean $\bar{M}$ gives the %error, E, as $E = 100(\frac{\sigma_M}{\bar{M}})$. Note, percentage error relates to a common definition of signal-to-noise ratio (SNR) as $SNR = \frac{\bar{M}^2}{\sigma_M^2} = \frac{100^2}{E^2}$. As in log-likelihood analysis, an ensemble of small sample means $\bar{\mathbf{G}}_m$'s are used to obtain the mean and standard deviation of E_m over independent samples m for use in figure 2-4*b*.

2.4.9 Detection analysis using likelihood-ratio test

Optimal binary hypothesis testing using Neyman-Pearson lemma [74, 14, 42] obtains a decision variable Λ_j that selects alternate hypothesis H_1 over null hypothesis H_0 when $\Lambda_j = \mathbf{G}_j^T\bar{\mathbf{G}}_1 - \mathbf{G}_j^T\bar{\mathbf{G}}_0 = M_{1j} - M_{0j} > \beta$ where the left-hand-side is the difference between the matched filter correlation of the measured image data with the expected mean signal of hypothesis one M_{1j} and the matched filter correlation of the measured image data with the expected mean signal of hypothesis zero M_{0j}, and the threshold β is determined from the given false-positive probability. In other words, the optimal decision is based on the simple difference between two elementary matched filter correlations of the data image with different potential mean signal patterns. Knowledge of statistical moments higher than the first, corresponding to the mean signal pattern,

are not necessary.

In the optical case, detection analysis using hypothesis testing is carried out between a null hypothesis H_0 corresponding to the $N = 9000$ image measurements, that is, $\mathbf{G}_j^{H_0} = \mathbf{G}_j$ and an alternate hypothesis H_1 generated by replacing a particular number of pixels by a mud patch starting at a pixel location (x, y) for each measurement $\mathbf{G}_j$, creating a new set of $N = 9000$ altered images $\mathbf{G}_j^{H_1}$. Note, the average level for offset adjustment in any instantaneous image is computed over pixels in the original image $\mathbf{G}_j^{H_0}$ and is also used for offset adjustment in the altered image $\mathbf{G}_j^{H_1}$ ensuring that the only difference in images $\mathbf{G}_j^{H_0}$ and $\mathbf{G}_j^{H_1}$ are the replaced pixels. The alternative approach of using a distinct offset computed from the H_1 data leads to negligible differences in pattern recognition performance for the optical examples used here. The replaced pixels were obtained from a mud patch from the scene shown in figure 2-1a but distinct from the 'patch of exposed ground' example in figure 2-4. The replaced pixels were from a patch of darker mud giving the appearance of a dark spot on the image, as seen in figure 2-4e. The replaced patch of t_n pixels is moved across different starting locations on the image. Figure 2-4c shows mean and standard deviation of average true positive rate, determined as area under the ROC curve, as a function of the number of replaced pixels t_n across multiple template means (Section 2.4) and for the different starting coordinates of the patch on the image for the offset-adjusted variance stabilizing transformed luminance data. Figure 2-4d shows mean and standard deviation of deficit from the variance-stabilizing transform average true positive rate as a function of the number of replaced pixels t_n for the other transforms.

See electronic supplementary material for more details on the relation between luminance and intensity, parameters used in the K-S test, and binary hypothesis testing for detection analysis.

2.5 Author Contributions

This chapter comprises of work appearing in Ref.[70] co-authored by Shourav Pednekar, Arun Krishnadas, Byunggu Cho and Nicholas C. Makris. Analysis and development shared by collaboration between all authors; S.P., A.K. and B.C. measured, reduced and processed experimental data with guidance from N.C.M.; Materials and Methods and electronic supplementary material primarily written by S.P. and A.K. with contributions from all authors; N.C.M. conceived, developed basic theory, and supervised overall project, primarily wrote main text, conducted overall editing with contributions from all authors.

Appendix A

Transmission Loss modeling

The depth-averaged two-way transmission loss integrated over the OAWRS resolution footprint $A(\rho_c, f_j)$, $TLA(\rho_c, f_j)$ [40], for a uniform distribution of fish in a thickness layer H within the OAWRS resolution footprint centered at horizontal location ρ_c, is given by

$$TLA(\rho_c, f_j) = 10\log_{10}\left(\int_{A(\rho_c, f_j)} \frac{1}{H}\int_{z_0-H/2}^{z_0+H/2} \chi(\boldsymbol{r}, \boldsymbol{r_S}; \boldsymbol{r_T}) dz_T d\boldsymbol{\rho}_{\boldsymbol{T}}^2 / r_{\text{ref}}^{-2}\right) \tag{A.1}$$

where

$$\chi(\boldsymbol{r}, \boldsymbol{r_S}; \boldsymbol{r_T}) = (4\pi)^4 \Big\langle |G(\boldsymbol{r}|\boldsymbol{r_T}; f_j, c(\boldsymbol{r_w}), d(\boldsymbol{r_w}))|^2 |G(\boldsymbol{r_T}|\boldsymbol{r_S}; f_j, c(\boldsymbol{r_w}), d(\boldsymbol{r_w}))|^2 |\boldsymbol{r_T}\Big\rangle \tag{A.2}$$

and $G(\boldsymbol{r}|\boldsymbol{r_T}; f_j, c(\boldsymbol{r_w}), d(\boldsymbol{r_w}))$ is the Green function between the target location $\boldsymbol{r_T} = (\boldsymbol{\rho_T}, z_T)$ and the receiver location $\boldsymbol{r}$, $\boldsymbol{\rho_T} = (x_T, y_T)$ is the target's horizontal location, $G(\boldsymbol{r_T}|\boldsymbol{r_S}; f_j, c(\boldsymbol{r_w}), d(\boldsymbol{r_w}))$ is the Green function between the source location $\boldsymbol{r_S} = (\boldsymbol{\rho_S}, z_S)$ and the target location $\boldsymbol{r_T}$. Here, H is the combined fish thickness layer inclusive of all independent depth layers of the different fish species. $c(\boldsymbol{r_w})$ and $d(\boldsymbol{r_w})$ are the sound speed and the seawater density respectively in the water column at any

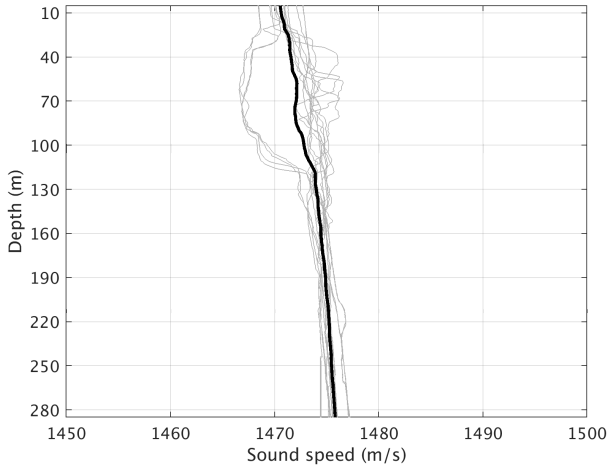

Figure A-1: Sound speed profiles from independent XBT measurements (solid grey lines) in the Finnmark region between February 26 and March 1, 2014. Black line shows mean sound speed profile.

point r_w in the propagation path. A range-dependent parabolic equation model [9] is used to calculate the Green functions in equation (5.2), which describe the random waveguide propagation to and from the target. The conditional expectation over the sound speed is determined by averaging five Monte-Carlo realizations, where the Green functions are calculated along the propagation path in range and depth for each realization. Each Monte-Carlo realization employs sound-speed profiles measured in the Finnmark region during the 2014 OAWRS experiment (figure A-1) at every 500 m along the propagation path.

Appendix B

Scatter function model of an individual fish

The backscattering cross section of an individual fish at depth z, neutral buoyancy depth z_{nb}, and fork length l at frequency f is determined [54] as

$$\left|\frac{S(z,z_{nb},l,f)}{k}\right|^2 = \frac{r^2(z,z_{nb},l)}{\frac{f_0^2(z,z_{nb},l)}{f^2}\eta^{-2}(z,z_{nb},l,f) + \left(\frac{f_0^2(z,z_{nb},l)}{f^2}-1\right)^2} \tag{B.1}$$

where $S(z,z_{nb},l,f)$ is the fish scatter function, k is the acoustic wavenumber, $r(z,z_{nb},l)$ is the equivalent radius of swimbladder, $f_0(z,z_{nb},l)$ is the swimbladder resonance frequency and $\eta(z,z_{nb},l,f)$ is the damping factor. The equivalent radius of swimbladder $r(z,z_{nb},l)$ is determined as

$$r(z,z_{nb},l) = \left[\frac{3}{4\pi}\frac{c_{nb}m_{flesh}(l)}{\rho_{flesh}}\frac{1+z_{nb}/10}{1+z/10}\right]^{1/3} \tag{B.2}$$

assuming that the swimbladder volume varies with pressure according to Boyle's law, where c_{nb} is the ratio of the swimbladder volume at neutral buoyancy to the volume of the fish flesh assumed to be 0.05 [ref], $V_{flesh} = m_{flesh}(l)/\rho_{flesh}$. Mass of a single

fish, $m_{flesh}(l)$, is empirically determined by the fork length l [31] and ρ_{flesh} is the density of the fish flesh. The resonance frequency of the swimbladder is determined by

$$f_0(z, z_{nb}, l) = \frac{\kappa(\epsilon(z, z_{nb}, l))}{2\pi r(z, z_{nb})} \sqrt{\frac{3\gamma P_{atm}(1 + z/10)}{\rho_{flesh}}} \tag{B.3}$$

where $\gamma = 1.4$ is the ratio of the specific heats of air, and $P_{atm} = 1.013{*}10^5$ Pa is the atmospheric pressure, $\kappa(\epsilon(z, z_{nb}, l))$ is the swimbladder correction term which is a function of the swimbladder's eccentricity $\epsilon(z, z_{nb}, l)$. The correction term $\kappa(\epsilon(z, z_{nb}, l))$ for a prolate spheroidal swimbladder [ref] is given by:

$$\kappa(\epsilon(z, z_{nb}, l)) = \frac{\sqrt{2}(1 - \epsilon^2(z, z_{nb}, l))^{1/4}}{\epsilon^{1/3}(z, z_{nb}, l)} \left[ln\left(\frac{1 + \sqrt{1 + \epsilon^2(z, z_{nb}, l)}}{1 - \sqrt{1 - \epsilon^2(z, z_{nb}, l)}} \right) \right]^{-1/2} \tag{B.4}$$

where $\epsilon(z, z_{nb}, l)$ is the ratio of the minor to major axis of a prolate spherical swimbladder given by $\epsilon(z, z_{nb}, l) = \left(\frac{c_{sb} l/2}{r(z, z_{nb}, l)} \right)^{-3/2}$ and c_{sb} is the ratio of the major axis of the swimbladder to the fish fork length l. The damping factor $\eta(z, z_{nb}, l, f)$ in equation (5.3) is obtained from:

$$\eta(z, z_{nb}, l, f) = \left[\frac{2\pi r(z, z_{nb}, l) f^2}{c} + \frac{\zeta}{\pi r^2(z, z_{nb}, l) \rho_{flesh}} \right]^{-1} f_0(z, z_{nb}, l) \tag{B.5}$$

where f is the frequency, c is the sound speed, and ζ is the viscosity of fish flesh.

Appendix C

Estimating neutral buoyancy depths of capelin and cod

Figures C-1 and C-2 show the method used to estimate neutral buoyancy depths of capelin and cod respectively. The black outline in figure C-1a marks the shoal boundary of the capelin scatterer. Mean measured scattering strength data SS_{data} across pixels within this boundary is shown in figure C-1b as a function of frequency and the errorbars represent the spread of the data across these pixels. Following equation (2.8), the modeled scattering strength of capelin can be expressed as

$$SS^{\text{capelin}}_{\text{model}}(z, z_{nb,cp}, H_{cp}, n_{A_{capelin}}, l_{cp}, f_j) = 10\log_{10}\left(\frac{1}{H_{cp}}\int_{z_{0,cp}-H_{cp}/2}^{z_{0,cp}+H_{cp}/2}\int_{l_{cp}}\left|\frac{S_{cp}(z, z_{nb,cp}, l_{cp}, f_j)}{k}\right|^2 g_{cp}(l_{cp})\,dl_{cp}\,dz.n_{A_{capelin}}\right) \tag{C.1}$$

where S_{cp} is the scatter function of an individual capelin, obtained from Love's model [54] following equations in Appendix B, in a uniformly distributed vertical layer over depth z with mean shoal depth $z_{0,cp}$, shoal thickness H_{cp}, neutral buoyancy depth $z_{nb,cp}$, capelin population density $n_{A_{capelin}}$, and length distribution $g_{cp}(l_{cp})$. Using local in-situ measurements of capelin shoal occupancy depths $z_{0,cp}$ from RV Knorr echosounder and capelin length distribution l_{cp} from trawl catch samples, neutral

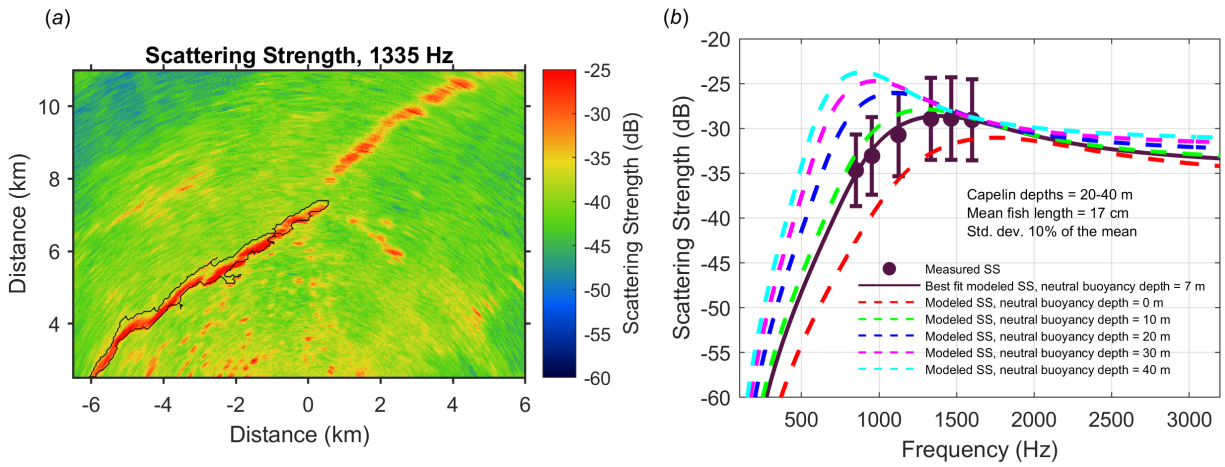

Figure C-1: (a) Instantaneous OAWRS scattering strength image at 05:25:49 CET for sensing frequency 1335 Hz . Location of OAWRS source, towed by RV Knorr, at 05:25:49 CET is taken to be the coordinate origin, at 71.2944 deg N, 25.7193 deg E. (b) Mean measured scattering strength data (brown marker points) across pixels within the capelin shoal boundary marked in black outline in (a) as a function of frequency and errorbars represent the spread of the data across these pixels. Uniform distribution of capelin assumed over occupancy depths of 20-40 m found from echogram measurements and standard deviation of 10% is assumed in mean capelin length of 17 cm from trawl samples. Neutral buoyancy depth of capelin is estimated to be approximately 7 m following least-squares fit between measured and modeled scattering strength. Capelin population density is estimated to be 12.6 $fish/m^2$.

buoyancy depth $z_{nb,cp}$ and capelin population density $n_{A_{capelin}}$ are determined by establishing the best fit between respective modeled and measured scattering strength of capelin. That is, the best estimate of capelin neutral buoyancy depth and population density are obtained by minimizing the magnitude of the weighted sum of square difference between the measured scattering strength and modeled capelin scattering strength:

$$\min_{z_{nb,cp},n_{A_{capelin}}} \left| \sum_{j=1}^{N_f} \left\{ -\frac{1}{2} \frac{(SS_{\text{data}}(f_j) - SS_{\text{model}}^{\text{capelin}}(f_j|z_{nb,cp}, n_{A_{capelin}}))^2}{\sigma_{f_j}^2} \right\} \right| \tag{C.2}$$

where the sum is over sensing frequencies f_j with $j = 1, 2, .., , N_f$.

The neutral buoyancy depth of cod is estimated in a similar manner. Mean measured scattering strength data SS_{data} is computed across pixels within a rectangular region as shown in figure C-2a. The measured scattering strength frequency response is shown in figure C-2b with errorbars representing spread of the data across these pixels. Following equation (2.10), the modeled scattering strength of cod is expressed as

$$SS_{\text{model}}^{\text{cod}}(z, z_{nb,cd}, H_{cd}, n_{A_{cod}}, l_{cd}, f_j) = 10 \log_{10} \left(\frac{1}{H_{cd}} \int_{z_{0,cd}-H_{cd}/2}^{z_{0,cd}+H_{cd}/2} \int_{l_{cd}} \left| \frac{S_{cd}(z, z_{nb,cd}, l_{cd}, f_j)}{k} \right|^2 g_{cd}(l_{cd})\, dl_{cd}\, dz . n_{A_{cod}} \right) \tag{C.3}$$

where S_{cd} is the scatter function of an individual cod in a uniformly distributed vertical layer over depth z with mean shoal depth $z_{0,cd}$, shoal thickness H_{cd}, neutral buoyancy depth $z_{nb,cd}$, cod population density $n_{A_{cod}}$ and length distribution $g_{cd}(l_{cd})$. Cod scatter function S_{cd} is obtained using the equations in Appendix B. Cod occupancy depths $z_{0,cd}$ are obtained from RV Knorr echosounder and cod length distribution l_{cd} from trawl catch samples. Cod neutral buoyancy depth $z_{nb,cd}$ and cod population density $n_{A_{cod}}$ are then obtained by minimizing the magnitude of the weighted sum of square difference between the measured scattering strength and modeled cod

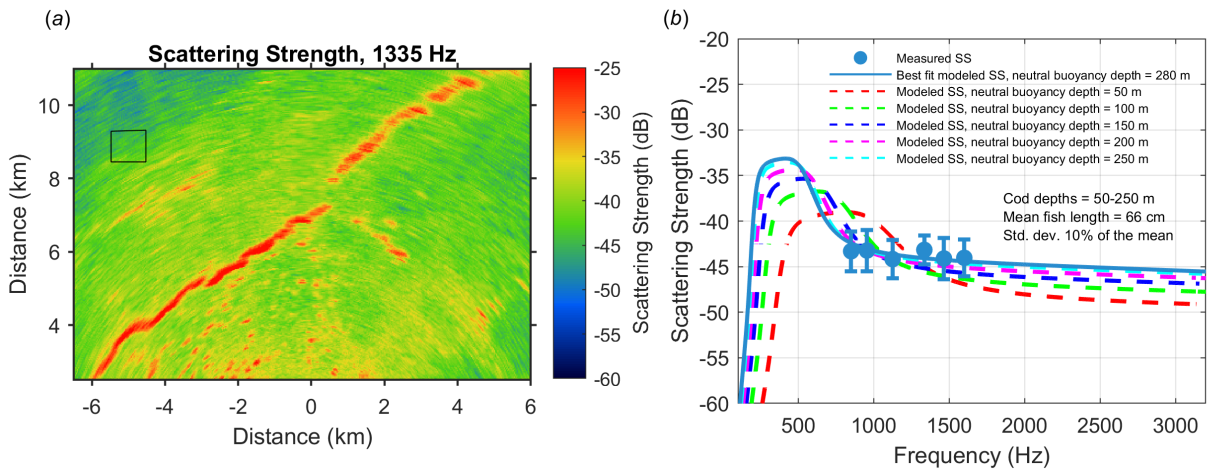

Figure C-2: (a) Same as figure C-1a but with black rectangular box outlining a region with relatively low scattering strength levels. (b) Mean measured scattering strength data (blue marker points) across pixels within the black rectangular box in (a) as a function of frequency and errorbars represent the spread of the data across these pixels. Uniform distribution of cod assumed over occupancy depths of 50-250 m obtained from echogram measurements and standard deviation of 10% is assumed in mean cod length of 66 cm from trawl samples. Neutral buoyancy depth of cod is estimated to be approximately 280 m following least-squares fit between measured and modeled scattering strength. Cod population density is estimated to be 0.025 $fish/m^2$.

scattering strength:

$$\min_{z_{nb,cd},n_{A_{cod}}} \left| \sum_{j=1}^{N_f} \left\{ -\frac{1}{2} \frac{(SS_{\text{data}}(f_j) - SS^{\text{cod}}_{\text{model}}(f_j|z_{nb,cd},n_{A_{cod}}))^2}{\sigma^2_{f_j}} \right\} \right| \tag{C.4}$$

where the sum is over sensing frequencies f_j with $j = 1, 2, .., , N_f$.

Appendix D

Seafloor scattering strength frequency response in Finnmark

Seafloor scattering frequency response is analyzed for a region with low scattering strength levels compared to measured fish scattering strength levels in the Finnmark region (figure D-1). Figure D-1a shows scattering strength map at 955 Hz, but relatively low scattering strength measurements were obtained for all frequencies within the white rectangular box marked in (a). Measured mean scattering strength for frequencies between 955 and 1600 Hz show a frequency dependence that approximately follows $f^{2.3}$ as shown in figure D-1b with the x-axis plotted in log-scale. The detection ranges at all frequencies were found to be at least 20 km. The analysis region marked as white rectangular box in figure D-1a was within 10 km from the source location at this time instant and so the received scattered field is not masked by ambient noise floor. Measured scattering strength data at sensing frequency 850 Hz is not plotted as the scattered returns at that frequency were contaminated by ship beams. Minimum cod population density detectable 3 dB above seafloor scattering levels at 955 Hz is estimated to be 0.01 $fish/m^2$. Minimum capelin population density detectable 3 dB above seafloor scattering levels at 955 Hz is estimated to be 0.24 $fish/m^2$.

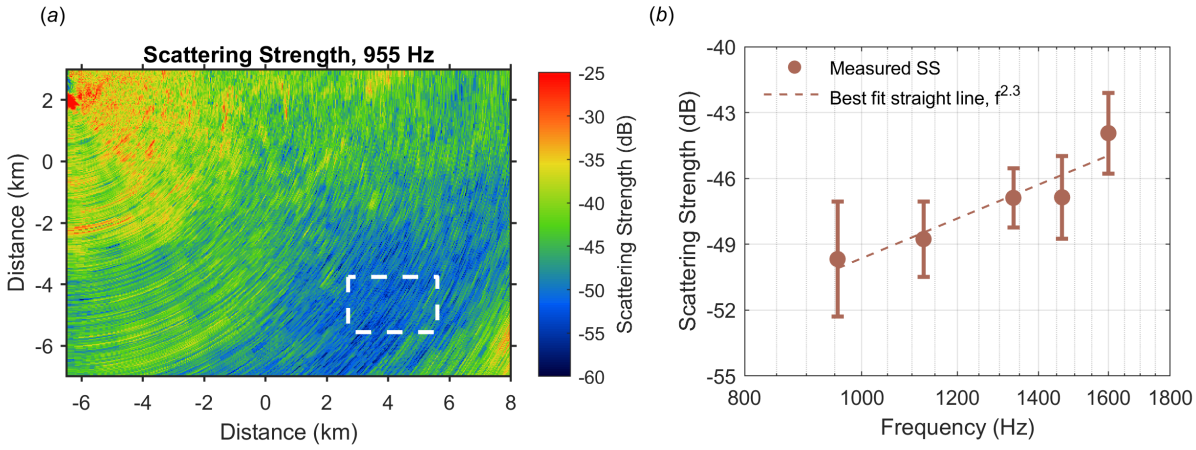

Figure D-1: (a) Instantaneous OAWRS scattering strength image on February 27, 04:15 CET for sensing frequency 1335 Hz . Coordinate origin at 71.2944 deg N, 25.7193 deg E. Dashed white rectangular box marks the analysis region. (b) Mean measured scattering strength data (brown marker points) over pixels within the white rectangular box in (a) as a function of frequency, errorbars show the spread of the data across these pixels. Measured seafloor scattering strength levels found here are lower than measured fish scattering strength levels. Mean scattering strength measurements show a frequency dependence that approximately follows $f^{2.3}$ for frequencies between 955 and 1600 Hz.

Appendix E

Luminance and Intensity

Total power in Watts received by a sensing aperture of area A may vary with time as

$$\Phi(t) = \int \phi(\lambda, t) d\lambda \tag{E.1}$$

where ϕ is the power spectral density as a function of wavelength λ measured over very short times and may be seen to vary due to random or deterministic processes over longer times t. The total luminous flux, in units of lumens, a spectrally filtered and normalized power, is defined as

$$\Phi_v(t) = \int_{\lambda_1=380nm}^{\lambda_1=750nm} \phi(\lambda, t).v(\lambda) d\lambda \tag{E.2}$$

where $v(\lambda)$ is a spectral weighting, or luminous efficacy for photopic vision, also known as the photopic sensitivity function, in units of lumens/W.

Total incident intensity unfiltered by the receiver is (in units of W/m^2),

$$I(t) = \frac{d\Phi(t)}{dA} \tag{E.3}$$

Surface luminance is then spectrally filtered and normalized intensity received via

$$\mathcal{L}_p(t) = \frac{d\Phi_v(t)}{dA}.\alpha^{-1} \tag{E.4}$$

where α, the solid angle resolution of the receiver for a given pixel, is a time-independent constant.

Luminance has the same time dependence and statistical fluctuations scaled only by a constant time-invariant factor as spectrally filtered intensity.

Appendix F

Supplementary figures for Weber's Law of perception is a consequence of resolving the intensity of natural scintillating light with the least possible error

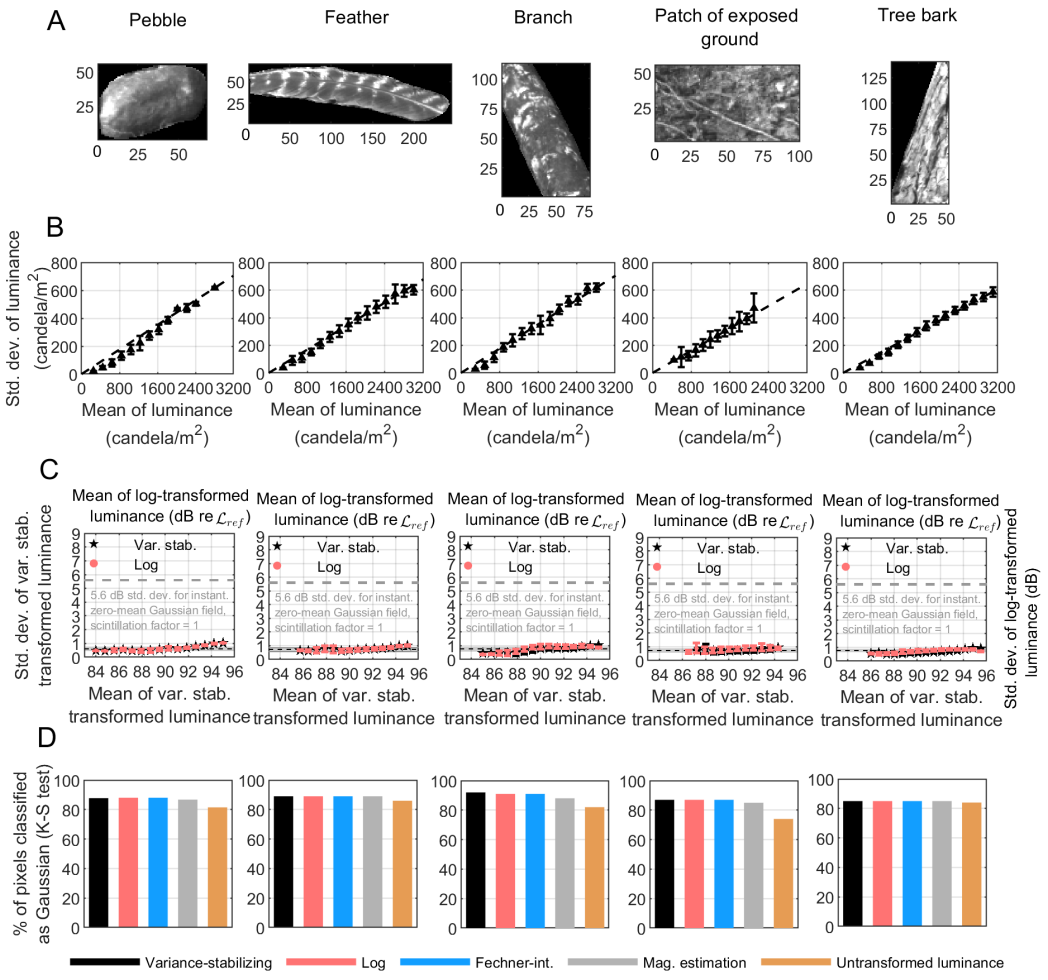

Figure F-1: Same as Fig 2-1 (a-c) and (f), reproduced for individual objects within the scene shown in Fig 2-1a. Note, $\mathcal{L}_{ref} = 1\mu$ candela/m2.

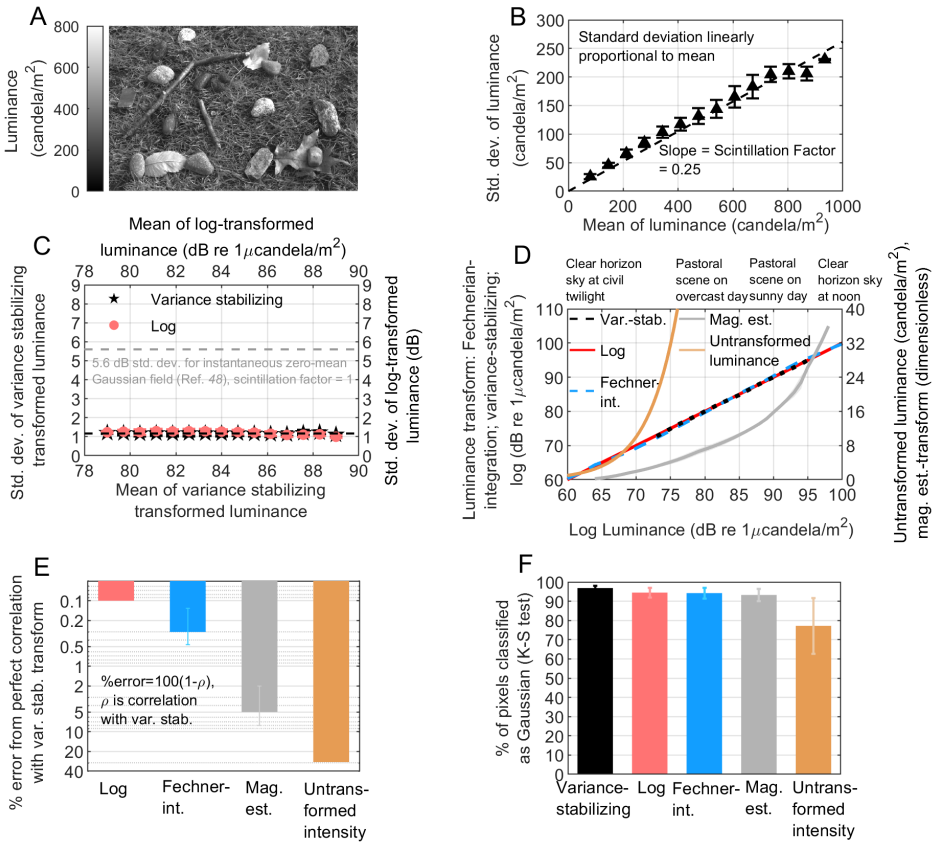

Figure F-2: Same as Fig 2-1 for a scene on sunny day with <25% cloud cover. Entire scene sampled every second over roughly 1 hour in the afternoon. Standard deviation of log-transformed luminance across pixels is 0.252 dB after instantaneous image offset of equation 2.8. The e-folding time scale of the autocorrelation is found to be roughly 150 s.

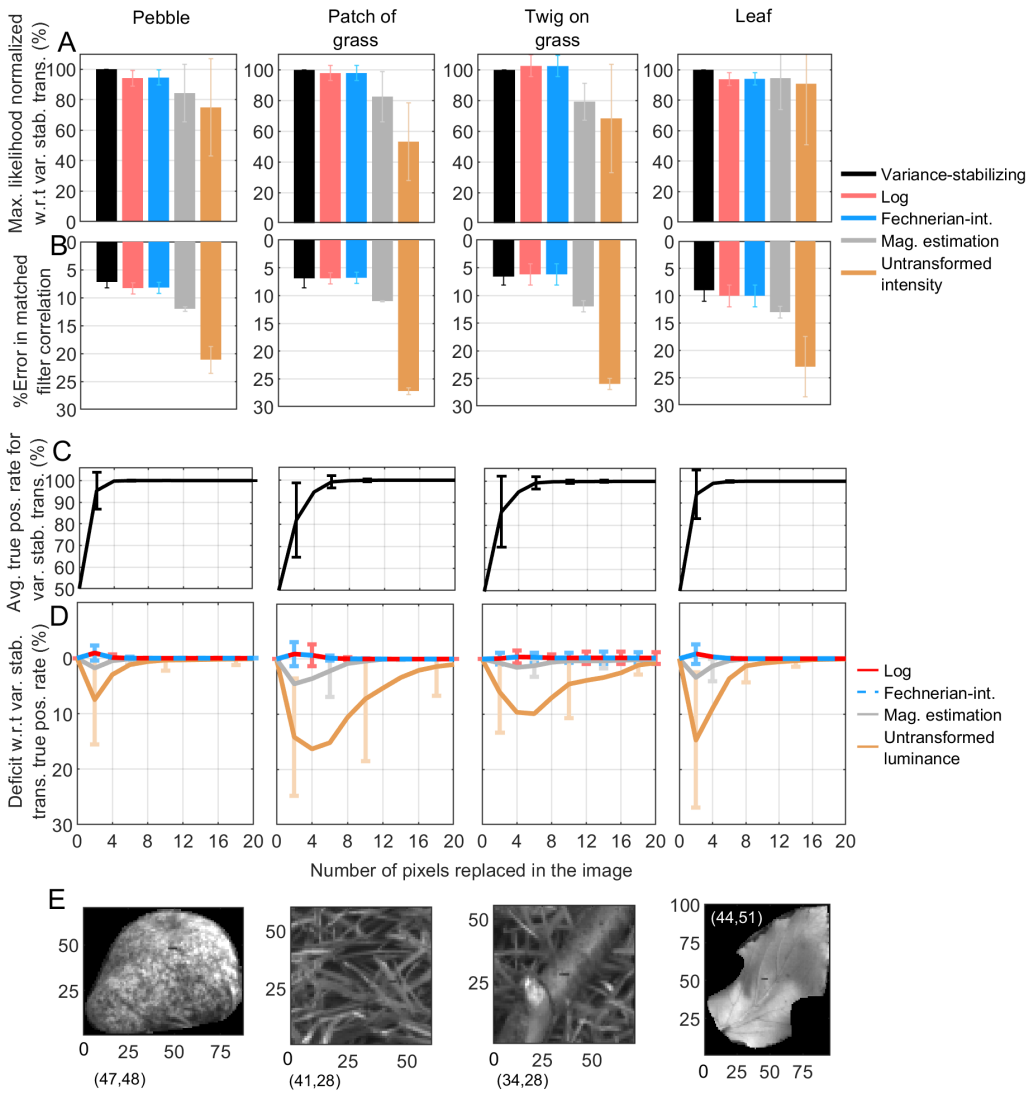

Figure F-3: Same as Fig 2-4 for objects on sunny day with <25% cloud cover.

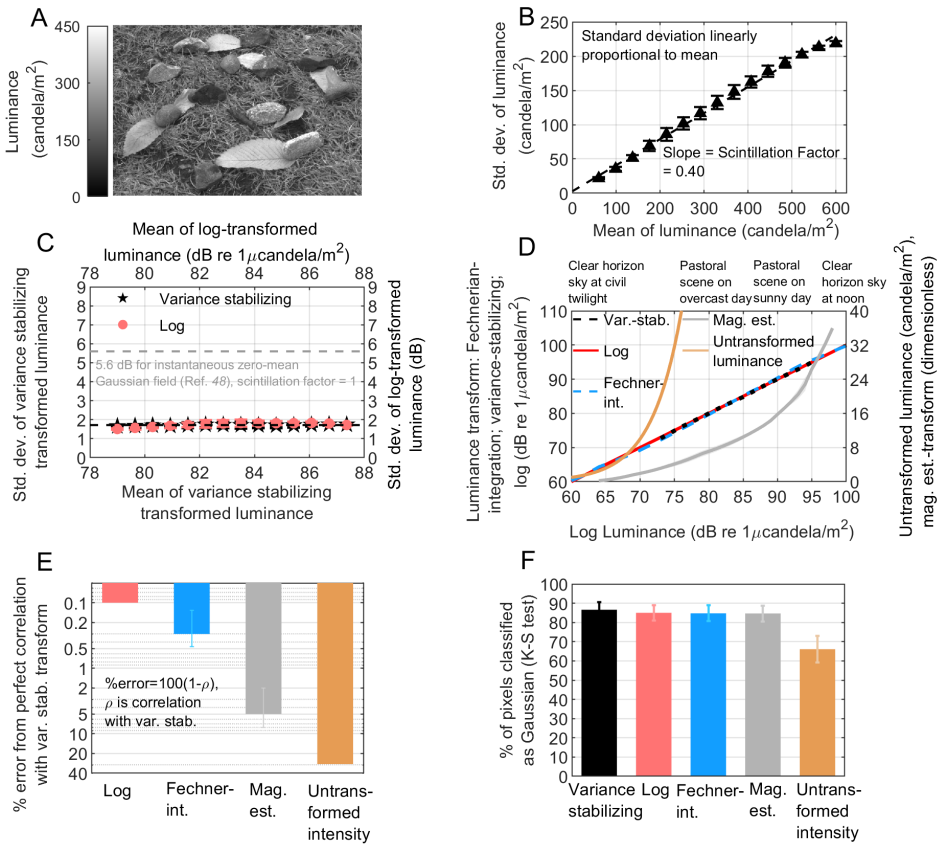

Figure F-4: Same as Fig 2-1 for a scene on overcast day with >70% cloud cover. Entire scene sampled every second over roughly 3.5 hours at midday. Standard deviation of log-transformed luminance across pixels is 0.391 dB after instantaneous image offset of equation 2.8. The e-folding time scale of the autocorrelation is found to be roughly 121 s.

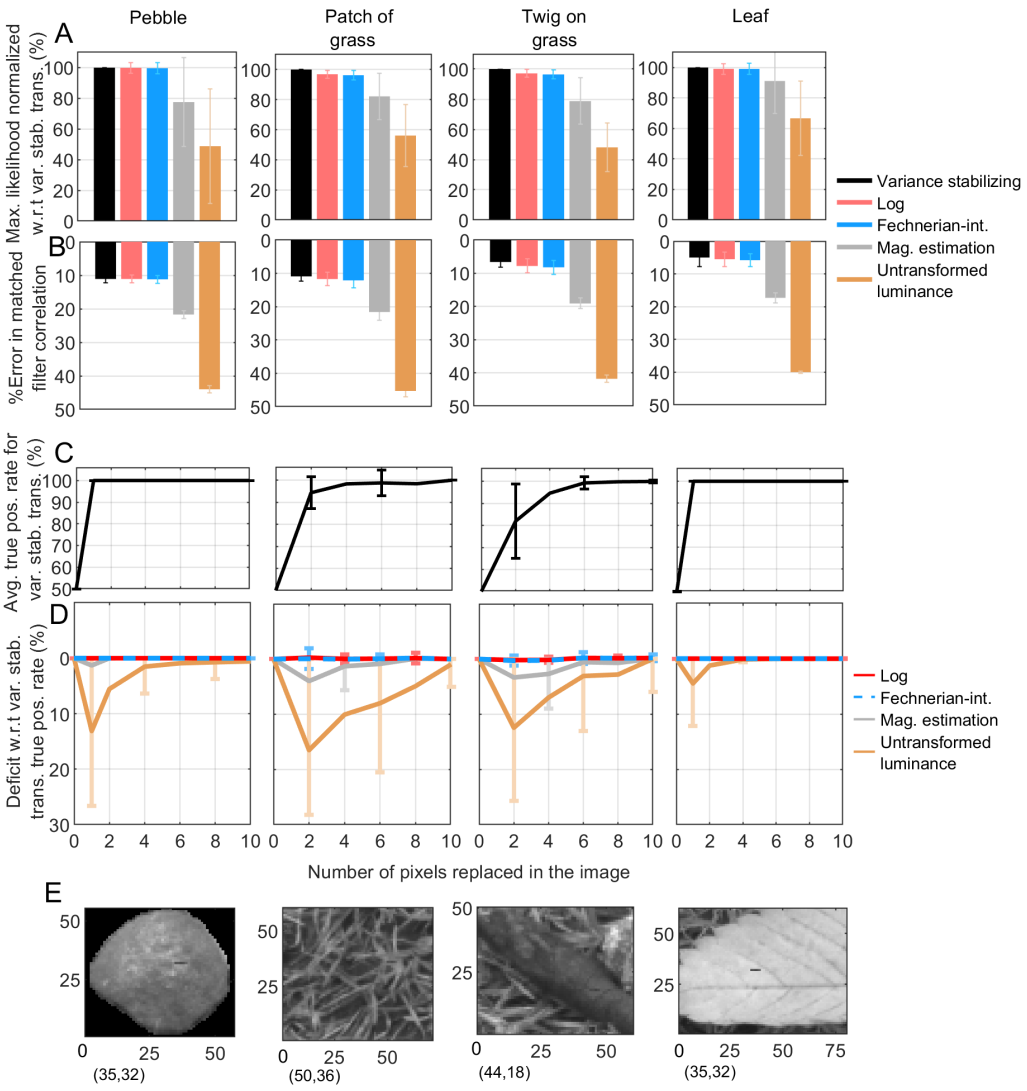

Figure F-5: Same as Fig 2-4 for objects on overcast day with >70% cloud cover.

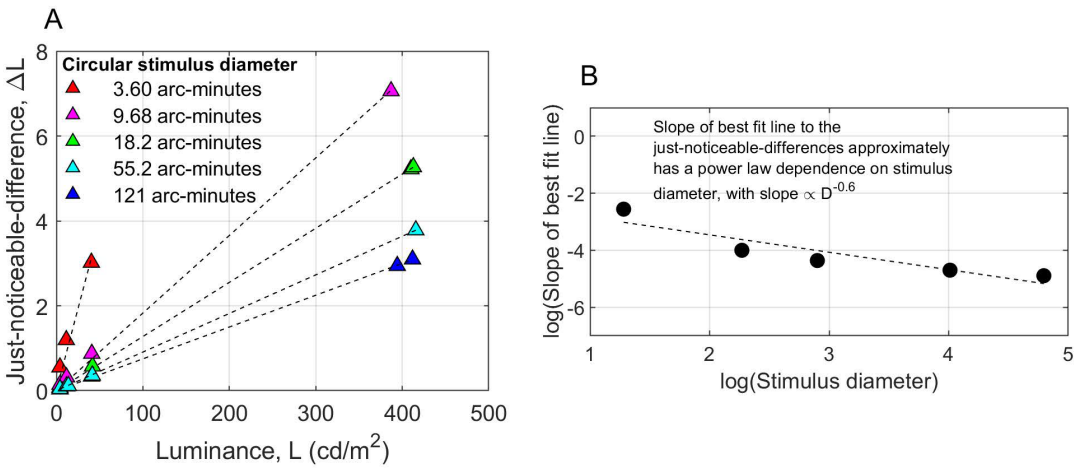

Figure F-6: Effect of illuminated patch size on measured just-noticeable-differences. (A) Blackwell's measurements of just-noticeable-difference functions for different visual patch sizes (Ref. [5]). (B) Slope of the best fitting line to the just-noticeable-difference data as a function of stimulating patch size diameter in the log-log scale.

Appendix G

Correlation with Variance-stabilizing transform

Figure 2-1e show correlation coefficients ρ_T for each transform indicated with the corresponding variance stabilizing transform $T_V(I)$ from Fig 2-1d respectively. The correlation coefficients ρ_T are computed across the 22 dB dynamic range of all the natural light intensity data on all days in Fig 2-1e. The correlation coefficient ρ_{FS_i} between $T_{FS_i}(I)$ and $T_V(I)$ is computed for the Fechner-sensation transform obtained from the i^{th} independent set of psychophysical just-noticeable-difference measurements, so that the mean and standard deviation of ρ_{FS_i} across i are shown in Fig 2-1e for the visual case. Similarly, correlation coefficient for magnitude estimation ρ_{ME_i} between $T_{ME_i}(I)$ (I) and $T_V(I)$ is shown in Fig 2-1e as the mean and standard deviation of ρ_{ME_i} across independent psychophysical investigations i.

Appendix H

Log-likelihood function

For the optical image data, let the offset-adjusted transformed luminance data be $G_j(x,y) = \tau(\mathcal{L}_j(x,y))$ at pixel (x,y) for measurement j, where $\tau(\mathcal{L}_j(x,y)) = \mathcal{L}_j(x,y) - \frac{1}{N_x N_y}\sum_{x=1}^{N_x}\sum_{y=1}^{N_y}\mathcal{L}_j(x,y)$ in the untransformed domain and $\tau(\mathcal{L}_j(x,y)) = T(\mathcal{L}_j(x,y)) - \frac{1}{N_x N_y}\sum_{x=1}^{N_x}\sum_{y=1}^{N_y}T(\mathcal{L}_j(x,y))$ in the transformed domain where T could be T_V, T_L, T_{FS} or T_{ME}. For convenience, let $\mathbf{G}_j = [G_j(1,1), G_j(1,2), ..., G_j(1,N_y), G_j(2,1), G_j(2,2), G_j(2,N_y), ..., G_j(N_x,N_y)]$ be an n-dimensional vector over the $n = N_x N_y$ pixels of the transformed or untransformed luminance image for the j^{th} sample of the entire image.

All the information necessary for statistical inference is contained in the likelihood function [24] given image measurement $\mathbf{G}_j$ via

$$p(\mathbf{G}_j|\bar{\mathbf{G}}, C) = \frac{1}{\sqrt{|C|(2\pi)^n}} e^{-\frac{1}{2}(\mathbf{G}_j - \bar{\mathbf{G}})^T C^{-1}(\mathbf{G}_j - \bar{\mathbf{G}})} \tag{H.1}$$

where $\mathbf{G}_j$ is a particular measurement of a multi-variate normal random vector $\mathbf{G}$ with mean $\bar{\mathbf{G}}$ and covariance C. For $j = 1, 2, ..., N$ independent measurements, the likelihood function becomes $\Pi_{j=1}^{N} p(\mathbf{G}_j|\mathbf{G}, C)$, and the log-likelihood function is given by

$$l(\bar{\mathbf{G}}, C) = \sum_{j=1}^{N} logp(\mathbf{G}_j|\bar{\mathbf{G}}, C) \tag{H.2}$$

such that

$$l(\bar{\mathbf{G}}, C) = \sum_{j=1}^{N}[-\frac{1}{2}(\mathbf{G}_j - \bar{\mathbf{G}})^T C^{-1}(\mathbf{G}_j - \bar{\mathbf{G}}) - \frac{1}{2} log|C|] + d \tag{H.3}$$

where d is a constant.

To compare likelihood functions across domains, the rule for transformation of random variables [14] to covert probability density functions in any transform to a common base transform, which is chosen to be the variance-stabilizing transform. Let the multivariate probability density function assuming the random vector is normal in any transformed domain $\mathcal{T}$, where $\mathcal{T}$ could be $\tau_V, \tau_L, \tau_{FS}, \tau_{ME}$ or the offset-adjusted untransformed domain in the optical case, be represented as $\mathcal{N}(\mathcal{T}(\mathbf{I}))$, where $\mathbf{I}$ is $\boldsymbol{\mathcal{L}} = [\mathcal{L}(1,1), \mathcal{L}(1,2), ..., \mathcal{L}(1,N_y), \mathcal{L}(2,1), \mathcal{L}(2,2), \mathcal{L}(2,N_y), ..., \mathcal{L}(N_x,N_y)]$ over $n = N_x N_y$ pixels. Further let the variance-stabilizing transformed random variable at pixel t be $\mathcal{T}_V(I(t)) = \mathcal{V}(t)$, for example. Then a random variable in any transformed domain $\mathcal{T}(I(t))$ can be written out explicitly in terms of the random variable in the variance-stabilizing transform $\mathcal{V}(t)$ as $\mathcal{T}(I(t)) = \mathcal{T}(\mathcal{T}_V^{-1}(\mathcal{V}(t))) = f_{\mathcal{T}}(\mathcal{V}(t))$, where the one-to-one function $f_{\mathcal{T}}$ converting from the variance-stabilizing transform to transform $\mathcal{T}$ is written as f_V, f_L, f_{FS}, f_{ME} and f_U for variance-stabilizing, log, Fechner-sensation, magnitude estimation, and untransformed intensity where $f_V(x) = x$ since a variance stabilizing transformed variable transforms to itself.

The Gaussian probability density functions for any transform $\mathcal{T}$, when converted to the variance-stabilizing transformed intensity is $\mathcal{N}(f_{\mathcal{T}}(\boldsymbol{\mathcal{V}}))|J_{\mathcal{T}}|$, where $J_{\mathcal{T}}$ is the Jacobian matrix between the transform $\mathcal{T}$ (where $\mathcal{T}$ could be $\mathcal{T}_{\mathcal{L}}, \mathcal{T}_{\mathcal{FS}}, \mathcal{T}_{\mathcal{ME}}$ or untransformed intensity) and the variance-stabilizing transform $\mathcal{T}_{\mathcal{V}}$. For the optical case, the determinant of the Jacobian matrix across transforms is invariant to offset-adjustment

such that $|J_{\mathcal{T}}| = \Pi_{t=1}^{t=n} \frac{\partial h[f_{\mathcal{T}}(\mathcal{V}(t))]}{\partial h[\mathcal{V}(t)]}$, where h is the one-to-one mapping that converts $\tau(I(t))$ to $T(I(t))$, where τ and T could be the respective pairs: τ_V and T_V, τ_L and T_L, τ_{FS} and T_{FS}, τ_{ME} and T_{ME}, or the offset-adjusted luminance and luminance $\mathcal{L}$. When finally converted to the variance-stabilizing domain by this procedure, the assumed Gaussian probability density function becomes for the: (1) variance-stabilizing transform $\mathcal{N}(\boldsymbol{\mathcal{V}})$; (2) the log transform $\mathcal{N}(f_L(\boldsymbol{\mathcal{V}}))|J_L|$; (3) Fechner-sensation transform: $\mathcal{N}(f_{FS}(\boldsymbol{\mathcal{V}}))|J_{FS}|$; (4) magnitude estimation transform $\mathcal{N}(f_{ME}(\boldsymbol{\mathcal{V}}))|J_{ME}|$; (5) untransformed intensity $\mathcal{N}(f_U(\boldsymbol{\mathcal{V}}))|J_U|$.

Using these probability density functions $\mathcal{N}(f_{\mathcal{T}}(\boldsymbol{\mathcal{V}}))|J_{\mathcal{T}}|$ and equation G.1, the likelihood function for any measurement j can be written as $\mathcal{N}(f_{\mathcal{T}}(\boldsymbol{\mathcal{V}}_j)|\bar{\mathbf{G}}, C)|J_{\mathcal{T}}(\boldsymbol{\mathcal{V}}_j)|$, where $\bar{\mathbf{G}}, C$ are the mean and covariance in that transformed domain $\mathcal{T}$ respectively, $f_{\mathcal{T}}$ is f_L, f_{FS}, f_{ME}, f_U or the identity function and $J_{\mathcal{T}}$ is J_L, J_{FS}, J_{ME}, J_U or the identity matrix. The corresponding log likelihood function becomes $l(\bar{\mathbf{G}}, C) + \sum_{j=1}^{N} log|J_{\mathcal{T}}(\boldsymbol{\mathcal{V}}_j)|$. From the identity form of the covariance this becomes $l(\bar{\mathbf{G}}, \sigma^2) + \sum_{j=1}^{N} log|J_{\mathcal{T}}(\boldsymbol{\mathcal{V}}_j)|$ which we denote by $l^{\mathcal{T}\rightarrow\mathcal{T}_V}(\bar{\mathbf{G}}, \sigma^2)$.

To obtain the maximum likelihood with the Gaussian assumption across transforms, first, $l^{\mathcal{T}\rightarrow\mathcal{T}_V}(\bar{\mathbf{G}}, \sigma^2)$ is computed for the entire data set of $j = 1, 2, ..., N$ samples, where $N = 9000$ in the optical case, using a practical short-term sample mean $\bar{\mathbf{G}}_m = \frac{1}{k}\sum_{j=m(1)}^{j=m(k)} \mathbf{G}_j$ from a set of $k = 5$ consecutive samples in the optical case, with σ^2 obtained from maximum likelihood estimation. The optical data sets over j are segmented to form such short sample $\bar{\mathbf{G}}_m$'s, each of which is used to evaluate the log-likelihood function $l^{\mathcal{T}\rightarrow\mathcal{T}_V}(\bar{\mathbf{G}}_m, \sigma^2)$, defined for brevity as $l_m^{\mathcal{T}\rightarrow\mathcal{T}_V}$, and to determine its statistics for a given transform across distinct sets m. Log-likelihood function in any transform $\mathcal{T}$, $l_m^{\mathcal{T}\rightarrow\mathcal{T}_V}$ is normalized by dividing by $n * N$ to factor out the effect of specific data sampling, where n is the number of pixels and N is the number of independent measurements of the entire image. The corresponding normalized likelihood function is $e^{l_m^{\mathcal{T}\rightarrow\mathcal{T}_V}/(nN)}$ for each transform, the mean maxima and standard deviations across $m = 1, 2, ..., 20$ of which are shown in Fig 4A for quantitative comparison after dividing with a constant normalization factor $e^{l_m^{\mathcal{T}_V\rightarrow\mathcal{T}_V}/(nN)}$ such that the normalized likelihood function in any transformed domain with respect to the variance-stabilizing

transform domain is $\frac{e^{l_m^{\mathcal{T}\to\mathcal{T}_V}/(nN)}}{e^{l_m^{\mathcal{T}_V\to\mathcal{T}_V}/(nN)}}$.

When luminance training data is distinct from test data the scaled identity matrix leads to higher log-likelihood for the covariance matrix C than the sample covariance of the test data, due to statistical fluctuations between training and test data that are overcome by the scaled identity form to which both sets converge. A scaled identity matrix C is then used exclusively in Figure 2-4. The hierarchy of which transforms have higher log-likelihood is unaffected by use of large (long) or small (short) samples sizes (or sample durations) for the mean $\bar{\boldsymbol{G}}$. Smaller samples (or shorter sampling durations) are likely more practical in hostile environments where rapid sensing is necessary and advantageous.

Appendix I

Detection analysis using likelihood-ratio test

Binary hypothesis testing [14, 42] for a mean pattern in the image data $\mathbf{G}_j$ employs two competing hypotheses: H_0 with mean $\bar{\mathbf{G}}_0$ and covariance $C_0 = \sigma^2 I$; and H_1 with mean $\bar{\mathbf{G}}_1$ and covariance $C_1 = \sigma^2 I$, where σ^2 is a signal-independent scale factor. The respective likelihood functions are given by

$$p(\mathbf{G}_j|\bar{\mathbf{G}}_0) = \frac{1}{\sqrt{(2\pi)^n}} e^{-\frac{1}{2\sigma^2}(\mathbf{G}_j - \bar{\mathbf{G}}_0)^T(\mathbf{G}_j - \bar{\mathbf{G}}_0)} \tag{I.1}$$

and

$$p(\mathbf{G}_j|\bar{\mathbf{G}}_1) = \frac{1}{\sqrt{(2\pi)^n}} e^{-\frac{1}{2\sigma^2}(\mathbf{G}_j - \bar{\mathbf{G}}_1)^T(\mathbf{G}_j - \bar{\mathbf{G}}_1)} \tag{I.2}$$

The above equations give the likelihood that the j^{th} sample of the image data $\mathbf{G}_j$ is from the null hypothesis H_0 and from the alternative hypothesis H_1 respectively. Using the Neyman-Pearson Lemma [42, 66, 74], the optimal decision criterion selects H_1, where optimal means true-positive detection probability is maximized for a given false-positive probability, when

$$\lambda_j = \frac{p(\mathbf{G}_j|\bar{\mathbf{G}}_1)}{p(\mathbf{G}_j|\bar{\mathbf{G}}_0)} > \eta \tag{I.3}$$

where the threshold η is determined from the given false-positive probability, also known as the probability of false alarm [42].

The decision rule of relation H.3 can be written in a far more compelling form. Expanding the likelihood functions using equations H.1 and H.2 in H.3,

$$\lambda_j = e^{-\frac{1}{2\sigma^2}[(\mathbf{G}_j-\bar{\mathbf{G}}_1)^T(\mathbf{G}_j-\bar{\mathbf{G}}_1)-(\mathbf{G}_j-\bar{\mathbf{G}}_0)^T(\mathbf{G}_j-\bar{\mathbf{G}}_0)]} \tag{I.4}$$

and the log of this yields the log-likelihood ratio

$$log\lambda_j = -\frac{1}{2\sigma^2}[(\mathbf{G}_j - \bar{\mathbf{G}}_1)^T(\mathbf{G}_j - \bar{\mathbf{G}}_1) - (\mathbf{G}_j - \bar{\mathbf{G}}_0)^T(\mathbf{G}_j - \bar{\mathbf{G}}_0)] \tag{I.5}$$

Subtracting constants in equation H.5 and normalizing by constants to only retain terms containing the data $\mathbf{G}_j$ yields

$$\Lambda_j = \frac{log\lambda_j - \bar{\mathbf{G}}_1^T\mathbf{G}_1 + \bar{\mathbf{G}}_0^T\mathbf{G}_0}{1/\sigma^2} = \mathbf{G}_j^T(\bar{\mathbf{G}}_1 - \bar{\mathbf{G}}_0) \tag{I.6}$$

In the optical case, $\mathbf{G}_j = [G_j(1), G_j(2), ..., G_j(n)]$ is a vector of size $n = N_xN_y$ such that $G_j(t)$ where $t = 1, 2, ..., n$ denotes a vectorized form of the offset-adjusted luminance $G_j(x, y)$ in any domain at pixel (x, y) for measurement j. That is, $G_j(x, y) = \mathcal{L}_j(x, y) - \frac{1}{N_xN_y}\sum_{x=1}^{N_x}\sum_{y=1}^{N_y}\mathcal{L}_j(x, y)$ in the untransformed domain and $G_j(x, y) = T(\mathcal{L}_j(x, y)) - \frac{1}{N_xN_y}\sum_{x=1}^{N_x}\sum_{y=1}^{N_y}T(\mathcal{L}_j(x, y))$ in the transformed domain where T could be T_V, T_L, T_{FS} or T_{ME}. Here, detection analysis using hypothesis testing is carried out between a null hypothesis H_0 corresponding to the $N = 9000$ image measurements, that is, $\mathbf{G}_j^{H_0} = \mathbf{G}_j$ where $j = 1, 2, ..., N$ and an alternate hypothesis H_1 generated by

replacing a particular number of pixels t_n by a mud patch where $t_n = 0, 1, 2, ..., 30$ starting at a pixel location (x, y) for each measurement $\mathbf{G}_j$, creating a new set of $N = 9000$ altered images $\mathbf{G}_j^{H_1}$ where $j = 1, 2, ..., N$. Note, the average level for offset adjustment in any instantaneous image, i.e. $\frac{1}{N_x N_y} \sum_{x=1}^{N_x} \sum_{y=1}^{N_y} \mathcal{L}_j(x, y)$ in the untransformed domain and $\frac{1}{N_x N_y} \sum_{x=1}^{N_x} \sum_{y=1}^{N_y} T(\mathcal{L}_j(x, y))$ in the transformed domain, is computed over pixels in the original image $\mathbf{G}_j^{H_0}$ and is also used for offset adjustment in the altered image $\mathbf{G}_j^{H_1}$ ensuring that the only difference in images $\mathbf{G}_j^{H_0}$ and $\mathbf{G}_j^{H_1}$ are the replaced pixels. The alternative approach of using a distinct offset computed from the H_1 data leads to negligible differences in pattern recognition performance for the optical examples used here. The replaced pixels were obtained from a mud patch from the scene shown in Fig 1A but distinct from the 'patch of exposed ground' example in Fig 4. The replaced pixels were from a patch of darker mud giving the appearance of a dark spot on the image, as seen in Fig 4E.

For both H_0 and H_1, $N_{train} = 4500$ samples are used as training set and multiple template means, $\bar{\mathbf{G}}_{0_m} = \frac{1}{k} \sum_{j=m_0(1)}^{j=m_0(k)} \mathbf{G}_j^{H_0}$ for H_0 and $\bar{\mathbf{G}}_{1_m} = \frac{1}{k} \sum_{j=m_1(1)}^{j=m_1(k)} \mathbf{G}_j^{H_1}$ for H_1, are generated from a small set $m = m_0, m_1$ where m_0, m_1 are distinct sets each containing $k = 5$ consecutive samples from the training set. The remaining $N_{test} = 4500$ samples in sets H_0 and H_1 are used to obtain the probability distribution of the test statistic given that data corresponds to the null hypothesis $p(\Lambda)|H_0$ and the probability distribution of the test statistic given that data corresponds to the alternate hypothesis $p(\Lambda)|H_1$ respectively. Finally, the replaced patch oft_n pixels is moved across different starting locations (x^i, y^i) where $i = 1, 2, ..., 40$ on the image. Figure 4C shows mean and standard deviation of average true positive rate, determined as area $A_{m,i}^V(t_n)$ under the ROC curve, obtained from the empirical distributions $p(\Lambda)|H_0$ and $p(\Lambda)|H_1$ as a function of the number of replaced pixels t_n across the multiple sets $m = 1, 2, ..., 20$ used to obtain template means $\bar{\mathbf{G}}_{0_m}$ and $\bar{\mathbf{G}}_{1_m}$ for the different starting coordinates (x^i, y^i) of the patch on the image where where $i = 1, 2, ..., 40$ for the offset-adjusted variance-stabilizing transformed luminance data $\mathbf{G}_j$ which is the vectorized form of $G_j(x, y) = T_V(\mathcal{L}_j(x, y)) - \frac{1}{N_x N_y} \sum_{x=1}^{N_x} \sum_{y=1}^{N_y} T_V(\mathcal{L}_j(x, y))$. Figure 4D shows mean and standard deviation of deficit $d_{m,i}^T(t_n) = A_{m,i}^V(t_n) - A_{m,i}^T(t_n)$ from the

variance-stabilizing transform average true positive rate as a function of the number of replaced pixels t_n for the other transforms, where $A^T_{m,i}(t_n)$ is the average true positive rate of transform T such that T could be T_L, T_{FS}, T_{ME} or the untransformed luminance.

Bibliography

[1] Karin L. Akre, Hamilton E. Farris, Amanda M. Lea, Rachel A. Page, and Michael J. Ryan. Signal perception in frogs and bats and the evolution of mating signals. *Science*, 333(6043):751–752, 8 2011.

[2] Salah Alrabeei, Sam Subbey, Sofie Gundersen, and Harald Gjøsæter. Spatial and temporal patterns of capelin (Mallotus villosus) spawning sites in the Barents Sea. *Fisheries Research*, 244:106117, 2021.

[3] M S Bartlett. The Use of Transformations. *Biometrics*, 3(1):39–52, 1947.

[4] Andrew Berdahl, Colin J Torney, Christos C Ioannou, Jolyon J Faria, and Iain D Couzin. Emergent Sensing of Complex Environments by Mobile Animal Groups. *Science*, 339(6119):574–576, 2 2013.

[5] H Richard Blackwell. Contrast Thresholds of the Human Eye. *J. Opt. Soc. Am.*, 36(11):624–643, 11 1946.

[6] B Bogstad and H Gjøsæter. Predation by cod (Gadus morhua) on capelin (Mallotus villosus) in the Barents Sea: implications for capelin stock assessment. *Fisheries Research*, 53(2):197–209, 2001.

[7] George E P Box, Gwilym M Jenkins, Gregory C Reinsel, and Greta M Ljung. *Time series analysis: forecasting and control*. John Wiley & Sons, 2015.

[8] Brondizio E. S., Settele J., Díaz S., and Ngo H. T. IPBES (2019): Global assessment report on biodiversity and ecosystem services of the Intergovernmental Science-Policy Platform on Biodiversity and Ecosystem Services. Technical report, IPBES secretariat, Bonn, Germany, 2019.

[9] Michael D Collins. A split-step Padé solution for the parabolic equation method. *The Journal of the Acoustical Society of America*, 93(4):1736–1742, 4 1993.

[10] T N Cornsweet and H M Pinsker. Luminance discrimination of brief flashes under various conditions of adaptation. *The Journal of Physiology*, 176(2):294–310, 1 1965.

[11] K J W Craik. The effect of adaptation on differential brightness discrimination. *The Journal of Physiology*, 92(4):406–421, 1938.

[12] J H Curtiss. On Transformations Used in the Analysis of Variance. *The Annals of Mathematical Statistics*, 14(2):107–122, 6 1943.

[13] Hugh Davson. *Physiology of the Eye*. Academic Press, New York, 4 edition, 1980.

[14] Julius V Di Franco and William L Rubin. Radar detection. 1968.

[15] Yadolah Dodge and Daniel Commenges. *The Oxford dictionary of statistical terms*. Oxford University Press on Demand, 2006.

[16] Dainis Dravins, Lennart Lindegren, Eva Mezey, and Andrew T Young. Atmospheric Intensity Scintillation of Stars. I. Statistical Distributions and Temporal Properties. *Publications of the Astronomical Society of the Pacific*, 109(732):173–207, 1997.

[17] Daniel Duane, Byunggu Cho, Ankita D. Jain, Olav Rune Godø, and Nicholas C. Makris. The effect of attenuation from Fish Shoals on long-range, wide-area acoustic sensing in the Ocean. *Remote Sensing*, 11(21), 11 2019.

[18] Daniel Duane, Olav Rune Godø, and Nicholas C. Makris. Quantification of wide-area norwegian spring-spawning herring population density with ocean acoustic waveguide remote sensing (OAWRS). *Remote Sensing*, 13(22), 11 2021.

[19] E Eriksen, H Gjøsæter, D Prozorkevich, E Shamray, A Dolgov, M Skern-Mauritzen, J E Stiansen, Yu. Kovalev, and K Sunnanå. From single species surveys towards monitoring of the Barents Sea ecosystem. *Progress in Oceanography*, 166:4–14, 2018.

[20] Elena Eriksen, Harald Gjøsæter, Alexander Trofimov, Randi Ingvaldsen, Tatiana Prokhorova, Pavel Krivosheya, Padmini Dalpadado, Jon Rønning, Andrey Dolgov, Tone Falkenhaug, Dmitry Prozorkevich, Georg Skaret, Jostin Alvarez, Bjarte Bogstad, , Lis Jørgensen, Denis Zakharov, T Tankovskaya, Vladimir Pavlov, and A Mashnin. *Survey report from the joint Norwegian/Russian ecosystem survey in the Barents Sea and adjacent waters, August-October 2014*. 1 2015.

[21] Johanna Fall, Lorenzo Ciannelli, Georg Skaret, and Edda Johannesen. Seasonal dynamics of spatial distributions and overlap between Northeast Arctic cod (Gadus morhua) and capelin (Mallotus villosus) in the Barents Sea. *PLOS ONE*, 13(10):e0205921–, 10 2018.

[22] Johanna Fall, Edda Johannesen, Göran Englund, Geir Odd Johansen, and Øyvind Fiksen. Predator–prey overlap in three dimensions: cod benefit from capelin coming near the seafloor. *Ecography*, 44(5):802–815, 5 2021.

[23] Gustav Theodor Fechner. *Elemente der psychophysik*, volume 2. Breitkopf u. Härtel, 1860.

[24] Ronald Aylmer Fisher. Statistical methods for research workers. *Statistical methods for research workers.*, (5th Ed), 1934.

[25] Thomas L Frölicher, Erich M Fischer, and Nicolas Gruber. Marine heatwaves under global warming. *Nature*, 560(7718):360–364, 2018.

[26] Stanley A Gelfand. *Hearing: An introduction to psychological and physiological acoustics*. CRC Press, 2017.

[27] D Georgobiani, J R Kuhn, and J M Beckers. Using eclipse observations to test scintillation models. *Solar Physics*, 156(1):1–5, 1995.

[28] G Gescheider. *Psychophysics: The Fundamentals*. 1997.

[29] Alejandro H Gloriani, Beatriz M Matesanz, Pablo A Barrionuevo, Isabel Arranz, Luis Issolio, Santiago Mar, and Juan A Aparicio. Influence of background size, luminance and eccentricity on different adaptation mechanisms. *Vision Research*, 125:12–22, 2016.

[30] Olav Rune Godø, Nils Olav Handegard, Howard I Browman, Gavin J Macaulay, Stein Kaartvedt, Jarl Giske, Egil Ona, Geir Huse, and Espen Johnsen. Marine ecosystem acoustics (MEA): quantifying processes in the sea at the spatio-temporal scales on which they occur. *ICES Journal of Marine Science*, 71(8):2357–2369, 10 2014.

[31] Zheng Gong, Mark Andrews, Srinivasan Jagannathan, Ruben Patel, J Michael Jech, Nicholas C Makris, and Purnima Ratilal. Low-frequency target strength and abundance of shoaling Atlantic herring (Clupea harengus) in the Gulf of Maine during the Ocean Acoustic Waveguide Remote Sensing 2006 Experiment. *The Journal of the Acoustical Society of America*, 127(1):104–123, 1 2010.

[32] David Marvin Green, John A Swets, and others. *Signal detection theory and psychophysics*, volume 1. Wiley New York, 1966.

[33] Benjamin S Halpern, Shaun Walbridge, Kimberly A Selkoe, Carrie V Kappel, Fiorenza Micheli, Caterina D'Agrosa, John F Bruno, Kenneth S Casey, Colin Ebert, Helen E Fox, Rod Fujita, Dennis Heinemann, Hunter S Lenihan, Elizabeth M P Madin, Matthew T Perry, Elizabeth R Selig, Mark Spalding, Robert Steneck, and Reg Watson. A Global Map of Human Impact on Marine Ecosystems. *Science*, 319(5865):948–952, 2 2008.

[34] Nils Olav Handegard, Kevin M. Boswell, Christos C. Ioannou, Simon P. Leblanc, Dag B. Tjøstheim, and Iain D. Couzin. The Dynamics of Coordinated Group Hunting and Collective Information Transfer among Schooling Prey. *Current Biology*, 22(13):1213–1217, 2012.

[35] Anthony D Hawkins and Marta Picciulin. The importance of underwater sounds to gadoid fishes. *The Journal of the Acoustical Society of America*, 146(5):3536–3551, 11 2019.

[36] Donald C Hood and Marcia A Finkelstein. Sensitivity to light. In K Boff, L Kaufman, and J Thomas, editors, *Handbook of Perception and Human Performance (Vol. 1: Sensory Processes and Perception)*, volume 1, chapter 5. Wiley, New York, 1986.

[37] A. J.M. Houtsma, N. I. Durlach, and L. D. Braida. Intensity perception XI. Experimental results on the relation of intensity resolution to loudness matching. *Journal of the Acoustical Society of America*, 68(3):807–813, 1980.

[38] C C Ioannou, V Guttal, and I D Couzin. Predatory Fish Select for Coordinated Collective Motion in Virtual Prey. *Science*, 337(6099):1212–1215, 9 2012.

[39] Christos C Ioannou, Frederic Bartumeus, Jens Krause, and Graeme D Ruxton. Unified effects of aggregation reveal larger prey groups take longer to find. *Proceedings of the Royal Society B: Biological Sciences*, 278(1720):2985–2990, 10 2011.

[40] Srinivasan Jagannathan, Ioannis Bertsatos, Deanelle Symonds, Tianrun Chen, Hadi Tavakoli Nia, Ankita Deepak Jain, Mark Andrews, Zheng Gong, Redwood Nero, Lena Ngor, Mike Jech, Olav Rune Godø, Sunwoong Lee, Purnima Ratilal, and Nicholas Makris. Ocean acoustic waveguide remote sensing (OAWRS) of marine ecosystems. *Marine Ecology Progress Series*, 395:137–160, 2009.

[41] Ankita D. Jain, Anamaria Ignisca, Dong Hoon Yi, Purnima Ratilal, and Nicholas C. Makris. Feasibility of Ocean Acoustic Waveguide Remote Sensing (OAWRS) of atlantic cod with seafloor scattering limitations. *Remote Sensing*, 6(1):180–208, 2013.

[42] Steven M Kay. *Fundamentals of statistical signal processing: estimation theory*. Prentice-Hall, Inc., 1993.

[43] A. Koenig and E. Brodhun. Experimentelle Untersuchungen über die psychophysische Fundamentalformel in bezug auf den Gesichtssinn. *Sitzungsber. preuss. Akad. Wissensch*, pages 917–931, 1888.

[44] Andrey Kolmogorov. Sulla determinazione empirica di una lgge di distribuzione. *Inst. Ital. Attuari, Giorn.*, 4:83–91, 1933.

[45] J Anthony Koslow. The role of acoustics in ecosystem-based fishery management. *ICES Journal of Marine Science*, 66(6):966–973, 7 2009.

[46] David H Krantz. Integration of just-noticeable differences. *Journal of Mathematical Psychology*, 8(4):591–599, 1971.

[47] Lester E Krueger. Reconciling Fechner and Stevens: Toward a unified psychophysical law. *Behavioral and Brain Sciences*, 12(2):251–267, 1989.

[48] Ralf H J M Kurvers, Stefan Krause, Paul E Viblanc, James E Herbert-Read, Paul Zaslansky, Paolo Domenici, Stefano Marras, John F Steffensen, Morten B S Svendsen, Alexander D M Wilson, Pierre Couillaud, Kevin M Boswell, and Jens Krause. The Evolution of Lateralization in Group Hunting Sailfish. *Current Biology*, 27(4):521–526, 2017.

[49] Katie LaBarbera, Peggy B. Nelson, and Mark A. Bee. Mate choice and the 'opposite miss' to Weber's law: proportional processing governs signal preferences in a treefrog. *Animal Behaviour*, 168:199–209, 10 2020.

[50] Trevor D Lamb. Light adaptation in photoreceptors. In Leonard A Levin, Siv F E Nilsson, James Ver Hoeve, Samuel Wu, Paul L Kaufman, and Albert Alm, editors, *Adler's Physiology of the Eye: Expert Consult, 11Th Edition*, chapter 20. Saunders/Elsevier, 11 edition, 2011.

[51] Jan Lauwereyns. *Brain and the gaze: On the active boundaries of vision*. MIT Press, 2012.

[52] Leonard A Levin, Siv F E Nilsson, James Ver Hoeve, Samuel Wu, Paul L Kaufman, and Albert Alm. Adler's Physiology of the Eye: Expert Consult, 11Th Edition. Technical report.

[53] Jason S Link. Evidence of ecosystem overfishing in U.S. large marine ecosystems. *ICES Journal of Marine Science*, 78(9):3176–3201, 11 2021.

[54] Richard H Love. Resonant acoustic scattering by swimbladder-bearing fisha). *The Journal of the Acoustical Society of America*, 64(2):571–580, 8 1978.

[55] Nicholas C Makris. A foundation for logarithmic measures of fluctuating intensity in pattern recognition. *Optics Letters*, 20(19):2012–2014, 1995.

[56] Nicholas C. Makris. The effect of saturated transmission scintillation on ocean acoustic intensity measurements. *The Journal of the Acoustical Society of America*, 100(2):769–783, 8 1996.

[57] Nicholas C Makris, Olav Rune Godø, Dong Hoon Yi, Gavin J Macaulay, Ankita D Jain, Byunggu Cho, Zheng Gong, Josef Michael Jech, and Purnima Ratilal. Instantaneous areal population density of entire Atlantic cod and herring spawning groups and group size distribution relative to total spawning population. *Fish and Fisheries*, 20(2):201–213, 3 2019.

[58] Nicholas C Makris, Purnima Ratilal, Srinivasan Jagannathan, Zheng Gong, Mark Andrews, Ioannis Bertsatos, Olav Rune Godø, Redwood W Nero, and J Michael Jech. Critical Population Density Triggers Rapid Formation of Vast Oceanic Fish Shoals. *Science*, 323(5922):1734–1737, 3 2009.

[59] Nicholas C Makris, Purnima Ratilal, Deanelle T Symonds, Srinivasan Jagannathan, Sunwoong Lee, and Redwood W Nero. Fish Population and Behavior Revealed by Instantaneous Continental Shelf-Scale Imaging. *Science*, 311(5761):660–663, 2 2006.

[60] Mark N Maunder and Kevin R Piner. Contemporary fisheries stock assessment: many issues still remain. *ICES Journal of Marine Science*, 72(1):7–18, 1 2015.

[61] S Mehl, Asgeir Aglen, Bjarte Bogstad, Gjert Dingsør, Harald Gjøsæter, Jane Godiksen, E Johannessen, Knut Korsbrekke, Pavel Murashko, Alexey Russkikh, Arved Staby, T Wenneck, and Rupert Wienerroither. Fish investigations in the Barents Sea winter 2013-2014. *IMR/PINRO Joint Report Series*, 2014(2):73 pp, 1 2014.

[62] R L Mitchell. Permanence of the Log-Normal Distribution*. *Journal of the Optical Society of America*, 58(9):1267–1272, 1968.

[63] Brian C J Moore. *An introduction to the psychology of hearing*. Brill, 2012.

[64] James W Morley, Rebecca L Selden, Robert J Latour, Thomas L Frölicher, Richard J Seagraves, and Malin L Pinsky. Projecting shifts in thermal habitat for 686 species on the North American continental shelf. *PLOS ONE*, 13(5):e0196127–, 5 2018.

[65] David J Murray. A perspective for viewing the history of psychophysics. *Behavioral and Brain Sciences*, 16(1):115–137, 1993.

[66] Jerzy Neyman and Egon Sharpe Pearson. IX. On the problem of the most efficient tests of statistical hypotheses. *Philosophical Transactions of the Royal Society of London. Series A, Containing Papers of a Mathematical or Physical Character*, 231(694-706):289–337, 1933.

[67] Kenneth Norwich and Elad Sagi. Deriving the loudness exponent from categorical judgments. *Perception & Psychophysics*, 64:804–814, 1 2002.

[68] Erik Olsen, Sondre Aanes, Sigbjørn Mehl, Jens Christian Holst, Asgeir Aglen, and Harald Gjøsæter. Cod, haddock, saithe, herring, and capelin in the Barents Sea and adjacent waters: a review of the biological value of the area. *ICES Journal of Marine Science*, 67(1):87–101, 1 2010.

[69] Judith Wheeler Onley. Light Adaptation and the Brightness of Brief Foveal Stimuli*. *Journal of the Optical Society of America*, 51(6), 1960.

[70] Shourav Pednekar, Arun Krishnadas, Byunggu Cho, and Nicholas C Makris. Weber's Law of perception is a consequence of resolving the intensity of natural scintillating light and sound with the least possible error. *Proceedings of the Royal Society A: Mathematical, Physical and Engineering Sciences*, 479(2271):20220626, 3 2023.

[71] Andrew J Pershing, Michael A Alexander, Christina M Hernandez, Lisa A Kerr, Arnault Le Bris, Katherine E Mills, Janet A Nye, Nicholas R Record, Hillary A Scannell, James D Scott, Graham D Sherwood, and Andrew C Thomas. Slow adaptation in the face of rapid warming leads to collapse of the Gulf of Maine cod fishery. *Science*, 350(6262):809–812, 11 2015.

[72] E K Pikitch, C Santora, E A Babcock, A Bakun, R Bonfil, D O Conover, P Dayton, P Doukakis, D Fluharty, B Heneman, E D Houde, J Link, P A Livingston, M Mangel, M K McAllister, J Pope, and K J Sainsbury. Ecosystem-Based Fishery Management. *Science*, 305(5682):346–347, 7 2004.

[73] Tony J Pitcher. Functions of Shoaling Behaviour in Teleosts. In Tony J Pitcher, editor, *The Behaviour of Teleost Fishes*, pages 294–337. Springer US, Boston, MA, 1986.

[74] Calyampudi Radhakrishna Rao. *Linear statistical inference and its applications*. Wiley New York, 1973.

[75] Purnima Ratilal, Yisan Lai, and Nicholas C Makris. Validity of the sonar equation and Babinet's principle for scattering in a stratified medium. *The Journal of the Acoustical Society of America*, 112(5):1797–1816, 10 2002.

[76] R. R. Riesz. The relationship between loudness and the minimum perceptible increment of intensity. *The Journal of the Acoustical Society of America*, 4(3):211–216, 1 1933.

[77] Guillaume Rieucau, Arne Johannes Holmin, José Carlos Castillo, Iain D Couzin, and Nils Olav Handegard. School level structural and dynamic adjustments to risk promote information transfer and collective evasion in herring. *Animal Behaviour*, 117:69–78, 2016.

[78] G A Rose. Capelin (Mallotus villosus) distribution and climate: a sea "canary" for marine ecosystem change. *ICES Journal of Marine Science*, 62(7):1524–1530, 1 2005.

[79] George A Rose and Sherrylynn Rowe. Northern cod comeback. *Canadian Journal of Fisheries and Aquatic Sciences*, 72(12):1789–1798, 10 2015.

[80] E J Seykora. Solar scintillation and the monitoring of solar seeing. *Solar Physics*, 145(2):389–397, 1993.

[81] Robert Shapley and Christina Enroth-Cugell. Chapter 9 Visual adaptation and retinal gain controls. *Progress in Retinal Research*, 3:263–346, 1984.

[82] Nickolay Smirnov. Table for estimating the goodness of fit of empirical distributions. *The annals of mathematical statistics*, 19(2):279–281, 1948.

[83] Jacinto Steinhardt. Intensity discrimination in the human eye: I. The relation of ΔI/I to intensity. *Journal of General Physiology*, 20(2):185–209, 11 1936.

[84] Joseph C Stevens and Stanley S Stevens. Brightness function: Effects of adaptation. *JOSA*, 53(3):375–385, 1963.

[85] S. S. Stevens. The Measurement of Loudness. *Journal of the Acoustical Society of America*, 27(5):815–829, 1955.

[86] J W Strohbehn. Modern theories in the propagation of optical waves in a turbulent medium. In John W Strohbehn, editor, *Laser Beam Propagation in the Atmosphere*, pages 45–106. Springer Berlin Heidelberg, Berlin, Heidelberg, 1978.

[87] H. C van de Hulst. *Light scattering by small particles*. Courier Corporation, 1981.

[88] Tamás Vicsek, András Czirók, Eshel Ben-Jacob, Inon Cohen, and Ofer Shochet. Novel Type of Phase Transition in a System of Self-Driven Particles. *Physical Review Letters*, 75(6):1226–1229, 8 1995.

[89] Tamás Vicsek and Anna Zafeiris. Collective motion. *Physics Reports*, 517(3):71–140, 2012.

[90] Delin Wang, Heriberto Garcia, Wei Huang, Duong D Tran, Ankita D Jain, Dong Hoon Yi, Zheng Gong, J Michael Jech, Olav Rune Godø, Nicholas C Makris, and Purnima Ratilal. Vast assembly of vocal marine mammals from diverse species on fish spawning ground. *Nature*, 531(7594):366–370, 2016.

[91] Delin Wang and Purnima Ratilal. Angular resolution enhancement provided by nonuniformly-spaced linear hydrophone arrays in ocean acoustic waveguide remote sensing. *Remote Sensing*, 9(10), 10 2017.

[92] Harry W Wessely and McLaren P Mitchell. Solar-Scintillation Measurements*. *Journal of the Optical Society of America*, 61(2):242–247, 1971.

[93] A D Woodhead. Variations in the activity of the thyroid gland of the cod, Gadus callarias L., in relation to its migrations in the Barents Sea II. The 'dummy of run' of the immature fish. *Journal of the Marine Biological Association of the United Kingdom*, 38(2):417–422, 1959.

[94] Dong Hoon Yi, Zheng Gong, J. Michael Jech, Purnima Ratilal, and Nicholas C. Makris. Instantaneous 3D continental-shelf scale imaging of Oceanic fish by multi-spectral resonance sensing reveals group behavior during spawning migration. *Remote Sensing*, 10(1), 1 2018.